

Alma Mater Studiorum – Università di Bologna

DOTTORATO DI RICERCA IN
Ingegneria Biomedica, Elettrica e dei Sistemi

Ciclo 34

Settore concorsuale: 09/E2 “Ingegneria dell’Energia Elettrica”

Settore scientifico disciplinare: ING-IND/33 “Sistemi Elettrici per l’Energia”

NANOSTRUCTURED PIEZOELECTRIC MATERIALS FOR THE DESIGN
AND DEVELOPMENT OF SELF-SENSING COMPOSITE MATERIALS
AND ENERGY HARVESTING DEVICES

Presentato da: Giacomo Selleri

Coordinatore Dottorato

Prof. Michele Monaci

Supervisore

Prof. Davide Fabiani

Esame finale anno 2022

Abstract

In the fields of artificial intelligence, robotic and mechanical engineering, the design of materials that combine their mechanical properties with other functionalities is rapidly becoming a great area of interest in the last years. Besides their structural duties, multifunctional composite materials can perform additional tasks, paving the way for a new generation of *smart* materials. For instance, Structural Health Monitoring systems aim to combine the mechanical strength and the lightweight of composite materials with sensing functionalities for the in-situ control of their health status. In this context, the main challenge is conferring to the material those smart functionalities in a non-intrusive manner, in order to impact as low as possible on the original mechanical properties.

The work activities reported in this thesis lie within this scenario, investigating the self-sensing and the energy harvesting capability of composite materials based on piezoelectric nanostructured elements.

The self-sensing composite materials were designed and fabricated by interleaving between the plies of the laminate the piezoelectric elements. The problem of negatively impacting on the mechanical properties of the hosting structure was addressed by shaping the piezoelectric materials in appropriate ways. In the case of polymeric piezoelectric materials, the electrospinning technique allowed to produce highly-porous nanofibrous membranes which can be immersed in the hosting matrix without inducing delamination risk. The flexibility of the polymers was exploited also for the production of flexible tactile sensors. The sensing performances of the specimens were evaluated also in terms of lifetime with fatigue tests. In the case of ceramic piezoelectric materials, the production and the interleaving of nanometric piezoelectric powder limitedly affected the impact resistance of the laminate, which showed enhanced sensing properties.

In addition to this, a model was proposed to predict the piezoelectric response of the self-sensing composite materials as function of the amount of the piezo-phase within the laminate and to adapt

its sensing functionalities also for quasi-static loads. Indeed, one final application of the work was to integrate the piezoelectric nanofibers in the sole of a prosthetic foot in order to detect the walking cycle, which has a period in the order of 1 second.

In the end, the energy harvesting capabilities of the piezoelectric materials were investigated, with the aim to design wearable devices able to collect energy from the environment and from the body movements. The research activities focused both on the power transfer capability to an external load and the charging of an energy storage unit, like, e.g., a supercapacitor.

Table of Contents

Introduction	9
1. Context and objectives.....	11
1.1 Sensing strategies for composite materials.....	11
1.1.1 Composite materials	11
1.1.2 Self-sensing composite material	12
1.1.3 Sensors for composite materials	16
1.2 Energy harvesting technologies.....	20
1.3 Aim of the work.....	25
2. Piezoelectric technologies	26
2.1 Piezoelectricity	26
2.2 Piezoelectric materials.....	28
2.2.1 Quartz	28
2.2.2 Ceramic piezoelectric materials.....	28
2.2.3 Polymeric piezoelectric materials.....	30
2.3 Piezoelectric applications	32
2.3.1 Direct piezoelectric effect.....	32
2.3.2 Indirect piezoelectric effect	36
3. Electrospinning.....	38
3.1 History of electrospinning	38
3.2 Working principle.....	39
3.2.1 Electrospinning parameters	40
3.2.2 Kinds of collectors.....	42
3.3 Core-shell electrospinning.....	45
4. Self-sensing nanostructured piezoelectric materials.....	46
4.1 Self-sensing laminate based on piezo-polymeric nanofibers.....	48
4.1.1 Context	48
4.1.2 Electrospinning	49
4.1.3 Chemical characterization	49
4.1.4 Polarization process.....	50
4.1.5 Nanofibers integration in a soft matrix.....	55

4.1.6	Electrode manufacturing.....	57
4.1.7	Self-sensing composite material.....	60
4.1.8	Micrograph analyses.....	62
4.1.9	Piezoelectric model.....	64
4.1.10	Characterization technique	67
4.2	Position flexible piezoelectric sensor based on core-shell nanofibers.....	68
4.2.1	Context	68
4.2.2	Polymeric solutions	70
4.2.3	Viscosity analyses.....	72
4.2.4	Coaxial electrospinning	74
4.2.5	Micrograph analyses.....	75
4.2.6	Sensor manufacturing	79
4.2.7	Characterization technique	82
4.3	Self-sensing laminate based on piezo-ceramic nanopowder	83
4.3.1	Context	83
4.3.2	PZT ceramic powder	83
4.3.3	Laminates manufacturing	84
4.3.4	Polarization.....	85
4.3.5	Piezoelectric model of the laminate.....	87
4.3.6	PZT and GFRP phases characterization	88
4.3.7	Signal conditioning.....	89
4.3.8	Characterization techniques of the composite	90
5.	Design of piezoelectric energy harvesting.....	93
5.1	Context	93
5.2	Power transfer.....	95
5.2.1	Piezoelectric materials.....	95
5.2.2	Acquisition circuit	95
5.2.3	Characterization techniques.....	96
5.3	Energy storage	97
5.3.1	Capacitor charging.....	97
5.3.2	Piezoelectric-supercapacitor coupling.....	98
5.4	PZT nanofibers	101
5.4.1	PZT nanofibers production.....	101
5.4.2	PZT nanofibers polarization	102
5.4.3	Characterization technique	103
6.	Results and discussion.....	104
6.1	Piezoelectric response of the self-sensing materials.....	104
6.1.1	Self-sensing material based on piezo-polymeric nanofibers	104
6.1.2	Position flexible piezoelectric sensor based on core-shell nanofibers.....	114
6.1.3	Self-sensing laminate based on ceramic nanopowder	115

6.2	Piezoelectric-based device for energy harvesting.....	121
6.2.1	Maximum power transfer	121
6.2.2	Energy storage	124
7.	Conclusive remarks	127
	References	134

Introduction

Over the last years, the diffusion of smart materials is rapidly increasing with the aim to couple the mechanical properties of the structural material with one or more functionalities, such as optical, magnetic, thermal, electrical, etc. The term *smart* refers to the capability of such material to respond in a precogitated manner to external stimuli, providing a real-time communication with the user.

The functionalization typically contributes to a physical or chemical process that improves the original status of the material. The reaction to the external stimuli can translate into the detection of external mechanical impacts (self-sensing), the automatic readjustment after a damage of its structure (self-healing), the power harvesting and the energy storage from environmental movements (self-powering). Therefore, these new materials aim to perform multiple functionalities in the context of energy efficiency and system intelligence, guaranteeing active responses and self-monitoring abilities.

This PhD work fits into this context with the aim to conceive and manufacture smart composite materials by using nanofibrous membranes to be interleaved inside a hosting matrix, which can be soft (e.g. silicon-based matrix) or stiff (e.g. epoxy-based matrix), according to the final application. The piezoelectric nature of the nanofibers confers to the composite material an energy harvesting potential and a self-sensing capability. Energy generation refers to the conversion of mechanical energy into electrical energy to be stored in a capacitor or directly be used to power a load. On the other hand, the self-sensing property of the composite material is not only designed for structural damage detection (like traditional Structural Health Monitoring systems), but it is also adapted to suit the smart composite material to work as a pressure sensor capable to detect the mechanical load applied on its surface.

The highly porous structure of a nanofibrous membrane favors its impregnation in the epoxy matrix, thus creating a network of piezoelectric receptors and conferring a *smart* behavior to the composite material. One of the most simple process to fabricate piezoelectric nanofibers is the electrospinning, whose study and optimization is one of the central aspects of this work. The electrospinning is an innovative and versatile technique for the production of the polymer in a nanostructured-fiber shape that enhances the specific performance of the piezo-material.

Therefore, with respect to conventional piezo-films, the use of nanofibrous membranes is beneficial in terms of structure compactness and piezoelectric efficiency, which is increased by the high surface to volume ratio.

The research activities are part of the European Project MyLeg, which aims to design a smart and intuitive osseointegrated transfemoral prosthesis embodying advanced dynamic behaviors. Beyond the activities carried out by the other partners of the project, this work focuses on the implementation of the nanofibrous membrane in the sole of the prosthesis. The piezo-membranes in the sole (Figure 0-1) are designed both to enhance the energy efficiency by harvesting the energy of the walking cycle and to guarantee a precise contact detection and ground morphology estimation.

Therefore, the experimental campaign of this work focused on two main fields. In Chapter 4, the design of three kinds of self-sensing composite materials based on polymeric and ceramic nanostructured piezoelectric elements is described; whereas in section 5, the study on piezo-based energy harvesting devices is reported. The results about the sensing performances of the composite materials and the energy harvesting capability of the designed devices are reported in Chapter 6.

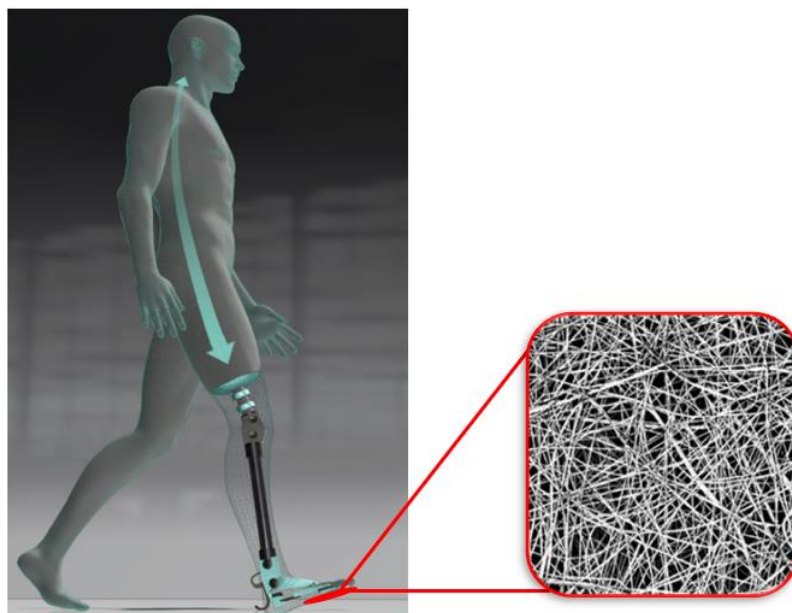


Figure 0-1 MyLeg prosthesis with piezoelectric nanofibers integrated into the sole

1. Context and objectives

1.1 Sensing strategies for composite materials

The strategies to create a self-sensing composite material essentially can be represented by two main techniques. According to the material properties and its structure, commercial sensors can be integrated into the composite material or bonded on its surface with limited impact on its mechanical strength. On the other hand, if the use of external sensors is not desirable or suitable, the intrinsic nature of the composite material can be exploited to confer it self-sensing capabilities by using different working principles. In this chapter, the most common sensing strategies for composite materials are described.

1.1.1 Composite materials

A composite material is commonly defined as the combination of two or more different materials at a macroscopic level. The interaction between the two materials (or phases) allows achieving new properties that cannot be attained acting alone [1], [2]. Composite materials consist of a reinforcing phase (i.e. fibers, flakes or particles) and a matrix phase (i.e. polymers, ceramic or metals) [3].

The main advantages of composite materials are their high specific strength and stiffness, their lightness, good vibration damping ability, high resistance to corrosion and temperature and their very strong tailor ability which makes them suitable to be manufactured for a wide range of applications. For instance, in aeronautics they are used to decrease structural loads and in naval infrastructures their high resistance to corrosion broadened their use. A specific class of composite material that is widely used for aerospace applications is fiber-reinforced plastic (FRP). The FRPs are composite materials based on a polymeric matrix reinforced with fibers made of glass or carbon. The matrix is usually a thermoset resin or epoxy. Therefore, the mechanical properties of the laminate mainly depend on the materials of the two phases, but also on the thickness of each ply and the fibers orientation. The manufacturing process of the laminates has been deeply investigated and various stacking optimization techniques have been explored [4], [5], [6].

Despite their multiple application fields, composite materials present some disadvantages. Their anisotropic properties stem from the multiphase structure of those materials, creating some drawbacks, in particular, in case of structural damages. So far, a clear description for the damage evolution and the flaw initiation represents a challenging work. The lack of reinforcement in the out-of-plane direction is a critical aspect, as in case of high energy impacts the matrix crack could induce delamination [7], debonding between the plies and a fiber breakage could also occur on the opposite side of the impact. If those damages occur beneath the laminate surfaces, their timely detection could be difficult and catastrophic failure of the entire structure could occur.

For these reasons, different techniques have been conceived in order to perform a live monitoring of the health status of the structure and prevent its failure. Non-destructive testing (NDT) methods such as ultrasonic, X-ray and thermography can be adopted but require voluminous equipment. Among these, Structural Health Monitoring (SHM) is an emerging technique that combines the use of sensors with an algorithm for a real-time monitoring of the structure health [8].

1.1.2 Self-sensing composite material

Based on different working principles, the sensing techniques that have been recently studied aim to realize non-invasive SHM methods and to create self-sensing structures that are able to continuously monitor the laminate conditions [9].

Resistive sensing mechanism

The carbon fiber-based composite materials exhibit a change in their electrical conductivity as the effect of a strain, damage or temperature variation [9]. The electrical resistance can therefore be measured and used as an indicator for those kinds of structural variations. These measurements can be performed in different ways, such as volume resistance, surface resistance and internal resistance. The volume resistance refers to a measurement where the electrodes are properly arranged in order to make the current flow through the whole volume of the composite. The surface resistance refers to a specific region of the composite and provides information such as the tensile/compressive surface region of a composite beam under flexure and interfacial resistance refers to the resistance of an interface of the composite. The status of the interfacial zone between two plies of the composite, which is the weakest point of the structure and the most common crack propagation region, can be described by monitoring the electrical resistance value. In this case, the current direction is usually perpendicular to the interface area and in case of delamination, the interfacial resistance is expected to increase.

Traditional methods for the aforementioned resistance measurements can be the two-probe method and the four-probe method. Moreover, an interfacial resistance measurement method is

described in Figure 1-1, where A, B, C and D are the electrical contacts of two laminates one on top of the other with an overlap area. The current flows from A to D and the voltage is measured between C and D. The resistance is easily calculated as the ratio between the voltage and the current [9].

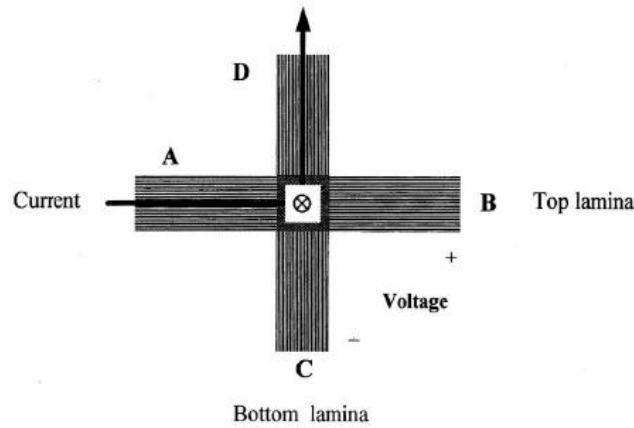


Figure 1-1 Interfacial resistance measuring method. Adapted from ref. [9].

In this way, two laminates alone provide an array of a sensor and the interface resistance can be used as a thermistor, a thermocouple junction, a stress sensor, a damage sensor and a moisture sensor. In the case of compression, a decrease of the resistivity was measured as a result of an increase in the number of contacts between the carbon fibers of the adjacent laminates. Different behaviors were found for a thermoset and thermoplastic matrix. In the case of a thermoplastic-matrix (e.g. polyamide), the piezoresistive effect was essentially reversible and more repeatable than for a thermoset-matrix (e.g. epoxy matrix). Indeed, due to the higher ductility of the polyamide matrix if compared with the epoxy matrix, the damage resistance is superior and the contact resistivity value exhibited great reversibility under repeated compression tests in the through-thickness direction [10]. The sensing efficiency was improved by means of nano-additive interleaving in the matrix [11]. Joo et al. demonstrated a high sensitivity damage mapping method by spreading carbon nanotubes (CNs) between the laminate prepregs, thus increasing the through-thickness electrical conductivity [12]. Even for low CNs concentrations (1% wt) electrically conductive networks were formed, acting as distributed sensors in the composite part. However, experiments showed that excessively high conductivity is not beneficial for the piezoresistive effect [13].

The disadvantages of the resistive effect-based self-sensing composite materials are mainly related to the electrodes contact resistance. Optimal contacts are required to be applied to the structure. Too high contact resistances could overshadow the composite resistance, which is the quantity of interest. Moreover, besides the resistance variation of the composite as effect of

external conditions, moisture and temperature could also impact the contact resistance of the electrodes, thus distorting the actual measurement [9].

Capacitive sensing mechanism

Unlike self-sensing composite materials based on the resistive-effect, literature on capacitive-based composite materials is limited. The self-sensing mechanism relies on the effect of damage, stress or strain on the capacitance of the structural composite. The sensing principle can be described by the typical structural capacitor configuration of Figure 1-2. Two conductive parallel plies of carbon fiber reinforced polymer (CFRP) work as electrodes and are separated by a dielectric between them. When the system is subjected to a small strain, the magnitude of the strain can be easily correlated to a variation of the capacitance value. External copper tapes can be connected to the carbon fiber as electrodes for the data acquisition system.

Carlson et al. investigated the impact of damage on the electrical properties of a structural capacitor made of carbon fiber/epoxy prepregs as structural electrodes with thermoplastic PET as the dielectric separator [14]. Shen and Zhou measured the electric capacitance as a function of the applied mechanical load by introducing three different separators as a dielectric between the CFRP plies. The mechanical load-induced capacitance deterioration was mainly due to interlaminar damage and delamination. However, it was observed that the load-bearing capacities of the designed structural capacitors are 5-30% lower than their CFRP counterparts, depending on the dielectric type [15]. In the case of using an epoxy matrix as dielectric separator, nanoparticles were added to enhance the sensing mechanism of the structure [16]. The test results show that doping the titania filler within the epoxy matrix can improve the sensor sensitivity, and that the sensor signal increases linearly with increasing strain.

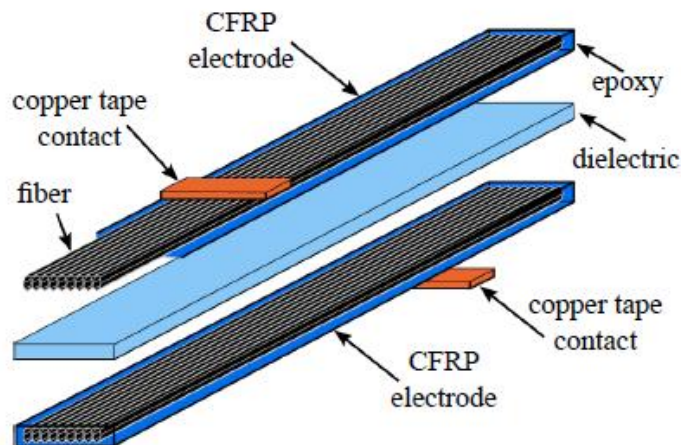


Figure 1-2 Schematic representation of the capacitive sensing working principle, according to ref. [16].

Antenna based sensing mechanism

Carbon fiber's conductivity allows a carbon fiber polymeric matrix composite to be shaped into an antenna. Damage to the composite affects the behavior of the antenna, allowing for wireless self-sensing of composite damage. Utilizing unidirectional CFRP laminates, the feasibility of wireless SHM using the self-sensing antenna approach is examined analytically and experimentally. When utilized as a half-wavelength dipole antenna, the CFRP radiates radio energy well, and damages to the CFRP may be detected wirelessly by monitoring an increase in the CFRP antenna's resonance frequency [17]. As observable in Figure 1-3, the power spectrum peak of the intact specimen is at 330 MHz, while the damaged one presents the peak at 570 MHz.

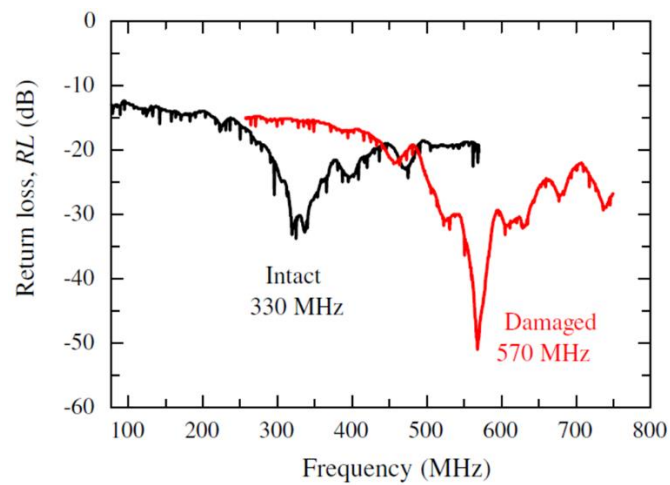


Figure 1-3 Frequency response of the return loss RL of intact and damaged CFRP rectangular specimens as antennas, adapted from [17].

Thermoelectricity based sensing mechanism

The thermoelectricity sensing mechanism is based on making two different oriented carbon fibers of two distinct plies of the CFRP laminate working as thermocouples, as represented in Figure 1-4. The acceptor and donor intercalation makes the two fibers (p-type and n-type) creating a thermocouple at the interlaminar interface. Bromine and sodium were intercalated to create the thermocouple and the array disposition of two crossed laminae was exploited to achieve a temperature distribution [18].

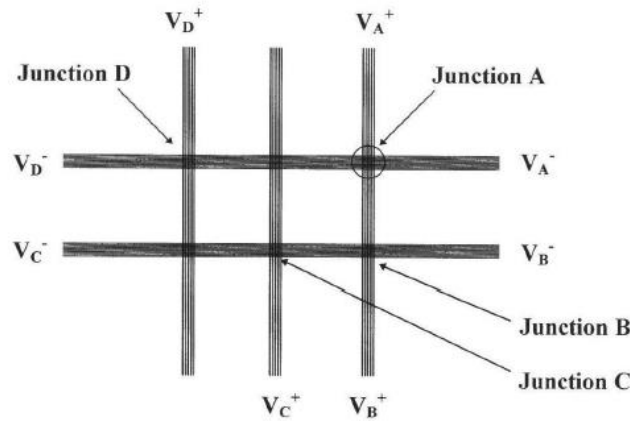


Figure 1-4 A six-junction sample for temperature distribution sensing, adapted from [18].

1.1.3 Sensors for composite materials

Resistance strain gage

The resistance strain gage is a strain sensing element which consists of a resistance grid of thin wire or foil, a connector and an encapsulation layer, as shown in Figure 1-5a. The strain-resistance effect causes the grid to sense the structure's strain as a resistance value, which may then be translated to a voltage signal using a Wheatstone bridge circuit, as shown in Figure 1-5b. The resistance strain gage can be bonded on the surface of the composite material and can resist to high pressures and temperature conditions.

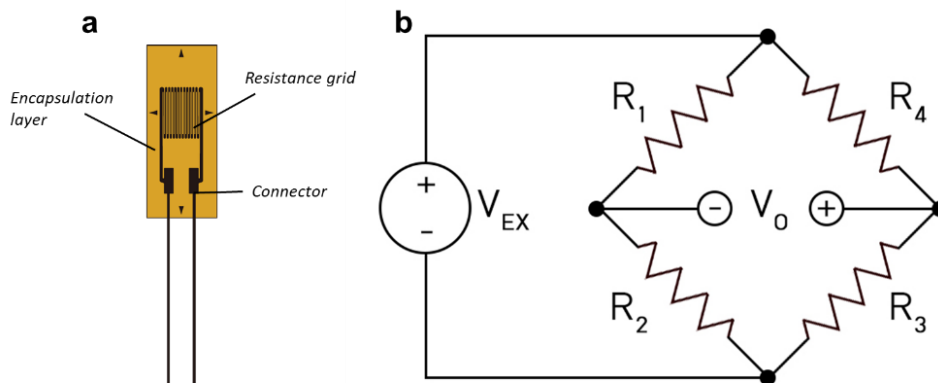


Figure 1-5 (a) Strain gage typical design; (b) Wheatstone bridge circuit.

Fiber optic sensors

Optical fiber sensors are widely accepted candidates for SHM in composite materials, thanks to their lightweight, high reliability and long-life cycles. The most common fiber-based sensors are

based on the so-called Fiber Bragg Gratings (FBGs) (average gage length: 5–10 mm) which can be printed serially into the core of an optical fiber. These sensors detect strains and deformations at local places by measuring the property variation of the transmitted or reflected spectra of optical waves. When a broadband light beam propagates through a FBG, a specific wavelength peak is back-reflected, which matches the micrometric period of the grating [19]. The axial strain stretches, or compresses, the period of the grating thus causing a wavelength shift of the reflected peak. This way, the strain may be determined by measuring the wavelength difference of the peak before and after applying the strain itself, as shown in Figure 1-6 [1]. FBG sensors can be easily multiplexed and can be deployed in a single fiber for quasi-distributed measurements.

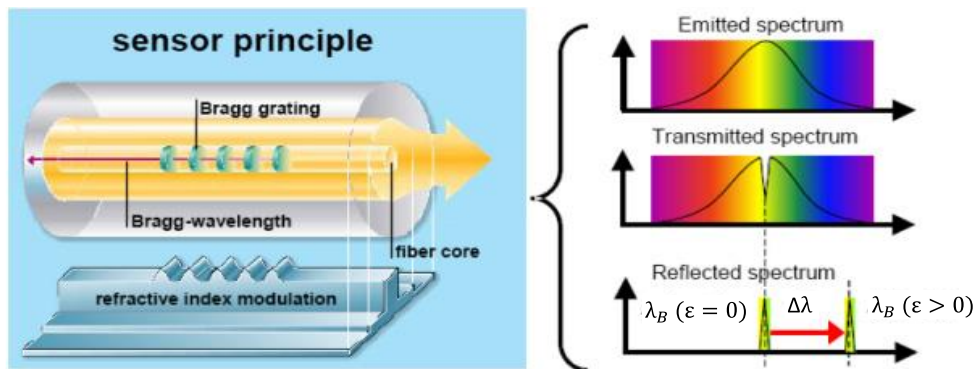


Figure 1-6 Fiber Bragg grating sensors [1].

Optical fibers can be embedded in the composite materials parallelly to the laminate reinforcing fibers direction. To lower the impact on the structure strength, the coating and the cladding of the fibers have to present appropriate mechanical properties. An optical fiber made of a 52 μm diameter of polyimide coating and a 40 μm diameter cladding was easily embedded into the CFRP plies of 125 μm thickness. Before integration, the FBG sensor was thermally treated at high temperature, showing a sufficient preservation of its mechanical strength and reflectivity. The optical characteristics of the FBG sensor integrated into the composite materials were analyzed as a function of the temperature and tensile strength, showing promising performances for SHM systems [20].

Another important aspect is that the FBG sensors are very sensitive to non-uniform strain distribution along the entire length of the grating, which makes them recommendable to localize the damages. Indeed, microscopic damages induce a non-uniform strain distribution in the CFRP composite. Okabe et al. embedded a FBG sensor in a 0° oriented CFRP ply, bordering a 90° oriented ply. The reflection spectrum results showed a peak in correspondence of the most damaged region of the 90° oriented ply [21]. Cracks localization was successfully performed also for quasi-isotropic CFRP laminate by embedding small diameter optical fibers (cladding diameter equal to 40 μm) between the plies [19].

Besides cracks detections, the FBG sensor showed promising responses also for the monitoring of delamination, which is a crucial problem in the composite laminates manufacturing. Free-edge delamination in CFRP [45/_45/0/90]_s laminate was detected by embedding small diameter optical fibers in a transverse direction with respect to the ply orientation plane, without introducing any significant defects. At the initial stage, with no delamination, a single peak in the reflection spectrum was observed. As delamination occurred, the peak divided into two different peaks, presenting a wavelength increasing with the delamination amplitude [22].

The effect of the integration of fiber optic sensors in composite materials was investigated in detail in terms of mechanical strength and elastic modulus. Song et al. found a decrease of the tensile strength of the self-sensing composite laminate equal to 4.7% compared with the pristine specimen. A little effect on the elastic modulus when FBG was embedded in different layers was also observed [23]. Moreover, the optical fiber effect on the laminate mechanical response when subjected to low-velocity impact was quantified and a lower stiffness due to the optical fiber integration was measured. The FBG sensor could represent a possible source for crack nucleation, favoring the crack propagation during the fatigue tests [24].

Piezoelectric sensors

Piezoelectric sensors are frequently used for SHM systems and vibrations measuring thanks to their lightness, low cost and reduced dimensions [25]. By means of the piezoelectric direct effect, they can generate charges as a stress is applied on the materials. Among the piezoelectric materials, lead zirconate titanate (PZT) wafers and polyvinylidene fluoride (PVdF) films are widely accepted for sensing applications. PZT usually presents higher piezoelectric coefficients than PVdF, but its fragile nature makes it not suitable for many applications. On the other hand, flexible PVdF films can be adapted for different geometries and manufactured in different shapes [26]. Impact localization on a composite material was also performed by means of PZT disks properly disposed on the surface. Signals are recorded by all sensors when the stress guided waves generated by an impact pass a particular mV threshold at one PZT. The wave time difference of arrival among the multiple sensors is then estimated using specific signal processing that incorporates filtering and dispersion compensation methods [27], [28]. Piezoelectric sensors can be either mounted on the surface of the composite and embedded within the laminate for a superior longevity and higher damage sensitivity. In both cases (surface-mounted or embedded sensors) the effect on the sensitivity and on the mechanical performance of the laminate was investigated [29].

Despite their various advantages, in the case of integration of the piezoelectric materials between the laminate plies of a composite laminate, some problems could occur. In particular, the breakage of PZT could lead to crack nucleation inside the plies and propagation of the damage [30].

To summarize, in Table 1-1 are listed the discussed sensing strategies for composite materials, taking into account the advantages and drawbacks of each technique.

Table 1-1 Sensing strategies for composite materials.

Sensing strategies		Sensing method	Ref	Advantages	Drawbacks
Self-sensing composite materials	Resistive	Interfacial resistance measurement	[10]	<ul style="list-style-type: none"> • Different types of damage detections; • Low impact on the mechanical properties of the composite. 	<ul style="list-style-type: none"> • Different types of damage detections; • Electrical contacts; • Power supply needed; • Environmental condition influence.
		Mechanical stress sensing of epoxy resin filled with CNs	[11]		
		Carbon fiber polypropylene (CFPP)/carbon nanotube (CNT) nano-composite damage sensing	[12]		
		Strain measurement of carbon fiber	[13]		
Capacitive	Impact damage of CFRP electrodes and PET separator	Mechanical load sensing on CFRP composite with different separators	[14]	<ul style="list-style-type: none"> • Different types of damage detections. 	<ul style="list-style-type: none"> • Impact of the dielectric separator on the composite structure; • External power supply.
		CFRP layer with a titania-filled epoxy resin separator	[15]		
			[16]		
Antenna	Damage detection by using CFRP as antenna	[17]	<ul style="list-style-type: none"> • Wireless monitoring. 	<ul style="list-style-type: none"> • Power supply needed. 	
Thermoelectricity	CFRP plies working as thermocouple	[18]	<ul style="list-style-type: none"> • Low intrusiveness. 	<ul style="list-style-type: none"> • Power supply needed. 	
Sensors for composite materials	Strain gage	Strain sensing element	[1]	<ul style="list-style-type: none"> • Small thickness; • Easy bonding on structures. 	<ul style="list-style-type: none"> • Limited frequency response.
	Optic fiber	Small-diameter FBG for transverse crack localization	[19]	<ul style="list-style-type: none"> • Light weight; • High sensitivity; • Long life-cycles. 	<ul style="list-style-type: none"> • Impact on the mechanical properties of the composite; • Possible source of crack nucleation.
		Damage detection by using FBG sensor in FRP laminate	[20]		
Transverse crack detection embedding FBG in CFRP	[21]				
Piezoelectric sensors	PVDF film for load sensing in CFRP		[26]	<ul style="list-style-type: none"> • Self-powering capability; • High sensitivity. 	<ul style="list-style-type: none"> • Crack nucleation in composite material; • Delamination induction between the laminate plies.
		PZT transducers for impact detection in composite panels	[27]		
		PZT sensor embedded in composite laminate	[28]		
			[30]		

1.2 Energy harvesting technologies

Energy harvesting is the increasingly common practice of trying to "collect" energy, from natural or environmental origin phenomena, which would otherwise be lost. The ultimate goal is to make certain devices self-supplied, avoiding of recharging from outside or replacing the power supply, e.g. batteries. This aspect is even more important in all those applications that involve equipment used in remote, isolated or difficult to reach places so the replacement of batteries could be very complicated, as in the extreme case of medical devices placed inside the human body. The energy harvesting technologies are designed for low-power electronic devices (<1 W) such as mobile phones, global positioning systems (GPS) and laptop computers and they can be coupled with a storage system, like capacitors, or connected to the final application for a direct supply. The energy conversion process starts from the individuation of the environmental energy source, which can be captured in different forms such as light, heat, vibration or pressures. The energy harvesting device is designed to convert such a source into an electrical output, whose amplitude depends on the nature of the input source and on the system efficiency. In the end, the useful energy provided by the device is transferred to the final applications. Usually, the transducing mechanism of the energy harvesting devices is not very efficient, indeed the energy conversion efficiency is often in the range of a few percent, depending on the working principle.

The energy developed from the body movements is attracting enormous interest in the last period and many are the solutions designed to convert into electrical energy the mechanical energy available in different parts of the body [31]. The large amounts of energy emitted by the human body in the form of heat and motion pave the way for the development of technologies that can harvest this energy and use it to power electronic devices. The most difficult aspect of designing such a technology is creating a system that can capture as much energy as possible while interfering as little as possible with the body's normal functioning. Furthermore, those energy harvesters should ideally not raise a person's metabolic cost, or the amount of energy necessary to carry out their daily duties.

According to their working principles, a wide variety of nanogenerators have been conceived, as described in the following.

Triboelectric nanogenerators (TENG)

The triboelectric effect is an electrical phenomenon that consists in the transfer of electric charges, and therefore in the generation of a voltage, between different materials (of which at least one insulator) when they are rubbed together. A first prototype of TENG was first developed in 2012 by Fan et al. for mechanical-to-electrical energy conversion based on coupled effects of triboelectrification and electrostatic induction. Two different polymeric sheets (Kapton and

polyethylene terephthalate) were stacked together and in case of mechanical deformation, the friction between the layers generated opposite polarity charges at the two sides of the system, as shown in Figure 1-7. The flexible TENG exhibited power densities up to 10.4 mW/cm^3 , with an output voltage of 3.3 V [32].

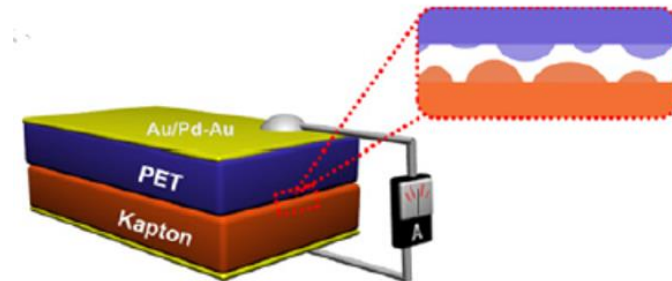


Figure 1-7 Triboelectric nanogenerator as designed by Fan et al. [32].

Further improvements in energy efficiency were achieved and area power densities up to 50 mW/m^2 and 15 W/cm^3 were reached by using metal gratings electrodes on polytetrafluoroethylene (PTFE) films [33].

The advantages of triboelectric nanogenerators lie in their simple design, their flexibility and lightweight, that make them suitable for wearable electronics and easily scalable for advanced structures designs. The highly bending part of the body, like the knee or elbow, are promising sites for their placements with low-frequency movements. Indeed, in a recent study was demonstrated that TENG shows the best harvesting performance in case of low-frequency mechanical deformations ($0.1 - 3 \text{ Hz}$) [34].

However, TENGs present pulse alternate energy output because of the unstable mechanical energy source, which makes them preferably to be coupled with a storing system. Typically, materials with strong triboelectric effects are less conductive or insulators, so the generated charges can be trapped or can stay at the surface for a long period of time. Zhou et al. demonstrated an in situ method for quantitative characterization of the triboelectrification and subsequent charge diffusion on the dielectric surface, providing a fundamental understanding of the triboelectric and de-electrification process, which is important for designing high performance triboelectric nanogenerators [35].

Electromagnetic energy harvester

The electromagnetic scavengers working mechanism is based on the electromagnetic induction principle. A voltage is generated across a conductive material when exposed to a variable magnetic field. A magnet is placed in relative movement to a coil and the Faraday's law of electromagnetic induction is the fundamental principle of the energy harvesting mechanism (Figure 1-8). A cantilever structure was designed to explore the opportunity to collect energy from vibrations. The designed structure, comprising a NdFeB magnet and a copper coil, was swung at low frequency (less than 100 Hz) and generated 2.34 mV [36].

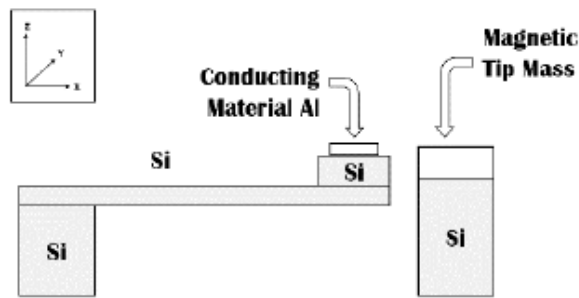


Figure 1-8 Basic Design of Energy Harvester based on Faraday's Law of Electromagnetic Induction [36].

Electrostatic energy harvester

The working principle of the electrostatic devices is based on the capacity variations of a parallel plate capacitor. The capacitor is charged by an external power source. When a variation of its configuration occurs – such as plate separation or surface overlapping – the voltage of the capacitor is varied, and charges can be extracted to provide energy to an external load (Figure 1-9). Various capacitor configurations and plate separation modes were explored. Meninger et al. optimized the moving method of the capacitor plates and that the estimated output power was equal to 8 μ W [37].

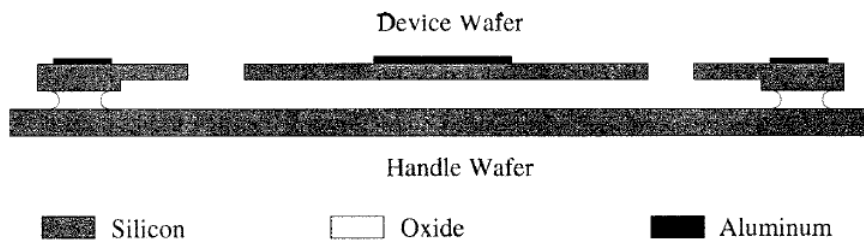


Figure 1-9 Electrostatic scavenger side view, adapted from [37].

The main disadvantages related to this energy harvesting technique regard the need of an external energy source to initially charge the capacitor.

Piezoelectric energy harvester

Piezoelectric materials, according with their piezoelectric coefficients, can be used not only for sensing applications but also for energy harvesting devices. If compared with the other energy scavengers working principles, piezoelectricity is a very convenient mechanism for capturing ambient mechanical energy since the piezoelectric effect is based on the intrinsic polarization of the materials. Consequently, the piezo-based energy harvesters do not require external power source to operate. Various structures have been designed, such as beams, cantilever and stuck, depending on the application. Among all the piezoelectric materials, their mechanical structure and the desired final use are the guide parameters for an appropriate choice. For instance, even if ceramic materials such as PZT disks present excellent piezoelectric performances, the brittle and fragile morphology makes them not suitable for flexible applications, such as wearable and stretchable devices [38]. Usually, PZT disk can be used in a stack configuration. On the other hand, a great number of wearable nanogenerators were developed in the last period, based on barium titanate (BaTiO_3), PVdF and its copolymers and zinc oxide (ZnO). Depending on their processability, the energy harvesting performances were investigated by manufacturing those materials in different shapes, such as PVdF films and nanofibers, ZnO nanowires and nanorods [39]. The coefficient that quantifies the charge generated on the surfaces of a piezoelectric material as a force is applied perpendicularly on those surfaces is the d_{33} , whose value is reported for each piezo-material in Figure 1-10.

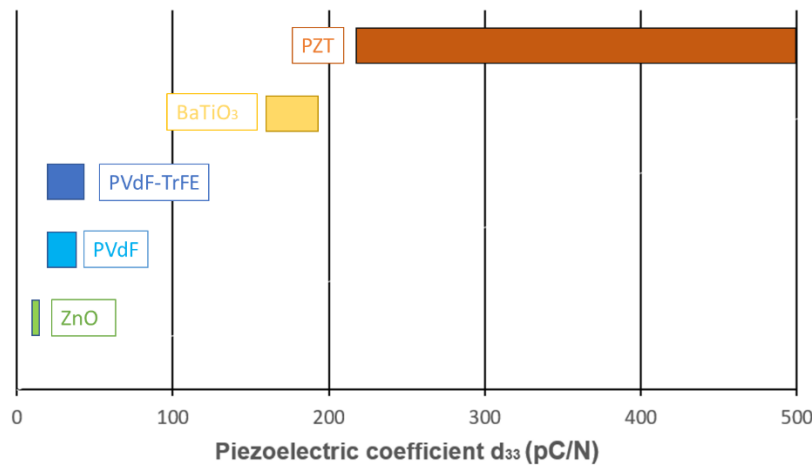


Figure 1-10 Piezoelectric d_{33} coefficient for each piezoelectric material

Some examples of the discussed energy harvesting techniques are reported in Table 1-2, considering the energy harvesting mechanism, the output power or energy, the advantages and disadvantages of each technique.

Table 1-2 Energy harvesting strategies based on different working mechanism.

Energy harvesting strategies	Energy harvesting method	Output	Ref	Advantages	Drawbacks
Trieboelectric	Friction between Kapton and PET sheets during bending	10.4 mW/cm ³	[32]	<ul style="list-style-type: none"> • Simple design; • Flexibility; • Lightweight; • Suitable for wearable applications. 	<ul style="list-style-type: none"> • Unstable and alternate energy output.
	Sliding motion between metal gratings and PTFE film	50 mW/m ²	[33]		
	Low-frequency motion between Cu electrodes and FEP films	8 μW/g	[34]		
Electromagnetic	Low frequency swing between a NdFeB magnet and a copper coil	1.1 μW	[36]	<ul style="list-style-type: none"> • Suitable for harvesting from vibrations. 	<ul style="list-style-type: none"> • External source for operating.
Electrostatic	Charge generation by overlapping of capacitor plates	8 μW	[37]	<ul style="list-style-type: none"> • Energy harvesting capability from vibrations. 	<ul style="list-style-type: none"> • External source for operating.
Piezoelectric	Palm impact on a PVdF-ZnO thin film	15 mJ/g	[38]	<ul style="list-style-type: none"> • No external source to operate; • Piezopolymers suitable for wearable applications; • High performances of piezo-ceramic. 	<ul style="list-style-type: none"> • Fragile structure of ceramic disks.
	Bulk PZT thick films	32 mW/cm ³	[39]		
	PZT disk in a cymbal structure under oscillating compressive force	52 mW	[39]		

1.3 Aim of the work

Among the self-sensing and energy harvesting techniques proposed in literature, the aim of this PhD work is to design multifunctional composite materials by embedding piezoelectric nanofibrous membrane in a hosting polymeric matrix.

If compared with traditional piezoelectric film or disk, the use of nanofibers presents two main advantages. First, the high surface/volume ratio of the nanofibers enhance the specific piezoelectric properties of the membranes and values comparable with the commercial bulky specimens can be reached with a remarkable material saving. Moreover, the embedding of highly porous nanofibrous layers between the plies of a composite laminate does not introduce defects on its structure - on the contrary of bulky disks or films – but even increases its mechanical strength thanks to the intimate contact between the nanofibers and the hosting matrix.

Therefore, the experimental campaign firstly focused on the optimization of the electrospinning technique and the realization of high-quality nanofibers. The investigations have been performed both on piezoelectric polymeric materials (PVdF-TrFE) and ceramic ones (PZT), in collaboration with the Department of Chemistry of the University of Bologna. Moreover, strong efforts were made with the purpose to maximize the piezoelectric response of the nanofibers by means of the polarization process, in order to achieve performance comparable with commercial piezoelectric bulky samples. Furthermore, the research activities focused on the integration of the piezoelectric nanofibers in the hosting matrix to realize multifunctional composite materials.

The electromechanical properties of both the PVdF-TrFE (in form of nanofibers) and PZT (in form of commercial disk, nanofibers and nanometric powder) were investigated in order to identify the best solutions for the design of self-sensing materials and energy harvesting devices.

To summarize, the following bullet point list reports the main research issues which this PhD work addresses:

- Investigation on the production of nanofibrous membranes and optimization of the electrospinning process;
- Study and optimization of the piezoelectric performance of nanostructured piezoelectric materials (PVdF-TrFE nanofibers and PZT powder) for sensing applications;
- Investigation on how the use of nanostructured piezoelectric materials affects the mechanical structure of the composite materials where they are integrated in;
- Study and development of energy harvesting systems based on piezoelectric materials.

2. Piezoelectric technologies

2.1 Piezoelectricity

Dielectric materials can be classified in 32 total crystal classes, which can be centrosymmetric and non-centrosymmetric according to the disposition of the center of symmetry of the crystal lattice. When the dielectric material is subjected to an external electric field, a mechanical deformation will occur on the material as a consequence of the displacement of the cations and ions of the lattice. In particular, cations will orient in the direction of the electric field and the anions will orient in the opposite direction. In the case of centrosymmetric dielectrics, the movements of anions and cations are such that the deformation of the crystal is ideally nil. On the other hand, in the case of materials without a center of symmetry of the crystal lattice, the movements of anions and cations result in a considerable deformation of the crystal. These materials are classified as piezoelectric materials [40]. Depending on the polarity of the electric field, the deformation of the material is compressive or extensive. This effect is called as *indirect piezoelectric effect* (Figure 2-1b). Indeed, as mechanical stress is applied on the surface of a piezoelectric material, the positive and negative charges will distribute on the two opposite surfaces of the material, generating an electric field across the crystal. Such a mechanism is defined as a *direct piezoelectric effect*, as shown in Figure 2-1b [40].

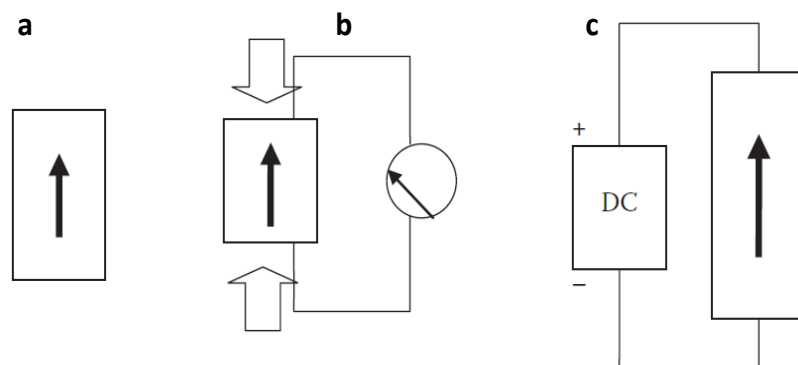


Figure 2-1 (a) Piezoelectric original shape; (b) direct piezoelectric effect; (c) indirect piezoelectric effect

The behavior of the piezoelectric materials can be described through piezoelectric coefficients, that define the magnitude of the piezoelectric response, both in case of direct and indirect piezoelectric effects. Among these, it is possible to define:

- Piezoelectric coefficient d :

$$d = \left(\frac{\partial D}{\partial X}\right) \quad (2.1)$$

defines the change in the polarization D as a mechanical stress X is applied on the material.

- Piezoelectric coefficient g :

$$g = -\left(\frac{\partial E}{\partial X}\right) \quad (2.2)$$

defines the change in the electric field E as a mechanical stress X is applied on the material.

- Piezoelectric coefficient e :

$$e = \left(\frac{\partial D}{\partial x}\right) \quad (2.3)$$

defines the change in the polarization D as a mechanical strain x is applied on the material.

- Piezoelectric coefficient h :

$$h = -\left(\frac{\partial E}{\partial x}\right) \quad (2.4)$$

defines the change in the electric field E as a mechanical strain x is applied on the material.

The polarization D and the electric field E are 3-components vectors, whereas the mechanical stress X and the strain x are 3x3-matrices. Thus, usually the piezoelectric coefficients are expressed with subscripts, in order to define the direction considered. For instance, the coefficient d is a 3x6-matrix and the d_{33} represents the amount of charge generated on the two surfaces divided by the force applied on the same surfaces. On the other hand, the coefficient d_{31} represents the amount of charge generated on the two surfaces divided by the force applied on the other two surfaces.

According to the nature of the piezoelectric element considered, the abovementioned coefficients

vary for every piezoelectric material. In particular, in this study, broad investigations have been conducted on the piezoelectric voltage coefficient d and the piezoelectric strain coefficient g .

2.2 Piezoelectric materials

Various kinds of piezoelectric material exist and can be classified according to their nature. The most widely used natural piezoelectric material is quartz, frequently used as a resonator (e.g., for digital watches) thanks to its crystalline structure. Moreover, ceramic piezoelectric materials such as lead zirconate titanate (PZT) and barium titanate (BaTiO_3) are widely used both as sensors and actuators. Among the polymeric materials, good piezoelectric properties are exhibited by the polyvinylidene fluoride (PVDF) and its copolymers, like polyvinylidene fluoride-trifluoroethylene (PVDF-TrFE).

In this section, an overview of the properties of these piezoelectric materials is reported, together with their typical applications.

2.2.1 Quartz

The quartz is considered a natural nonferromagnetic piezoelectric material, whose single crystalline form is silicon dioxide (SiO_2). The main advantages of the quartz, with respect to the other piezoelectric material, are its robust mechanical stability, its stiffness and its reliability over a long period. Moreover, environmental conditions and ambient temperature do not affect its behavior. The quartz is commonly used for various applications, such as pressure sensors, microphones or digital resonators. For instance, the cylinder pressures of the internal combustion engine or the pressure changes of the pneumatic can be measured by stacking a series of quartz layers that are compressed. Thus, a proportional output voltage is generated by the quartz crystals. Moreover, quartz thin plates are frequently used for microphones, where the geometry and the thickness of the layer are chosen in order to generate an audible sound frequency range output.

2.2.2 Ceramic piezoelectric materials

In this paragraph, a brief description of the most common ceramic piezoelectric materials (lead zirconate titanate and barium titanate) is reported.

Lead zirconate titanate

Among the ceramic piezoelectric materials, lead zirconate titanate (PZT) is the most frequently used for actuators and transducers applications thanks to its high piezoelectric properties. Its crystalline structure is called perovskite and presents the lead atoms in the corner and the oxygens in the middle of the faces, whereas the zirconium or titanate atoms are placed in the center of the structure, as shown in Figure 2-2.

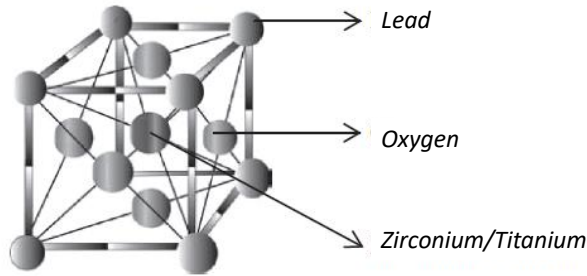


Figure 2-2 Schematic representation of the PZT crystalline structure

Above the Curie temperature of PZT, (typically 350°C, but slight changes can occur according to the specific composition), the structure of the crystal is cubic and the material is paraelectric. In the case of titanium-rich compositions, below the Curie temperature, the material becomes ferroelectric and the structure becomes tetragonal. On the other hand, in the case of zirconium rich composition, below the Curie temperature the structure of PZT changes from cubic to rhombohedral. The piezoelectric response of the PZT is then strictly correlated to its composition. As demonstrated by Jaffe et al., the piezoelectric coefficient d_{33} and the dielectric constant of PZT can be expressed as function of its composition (Figure 2-3) [41].

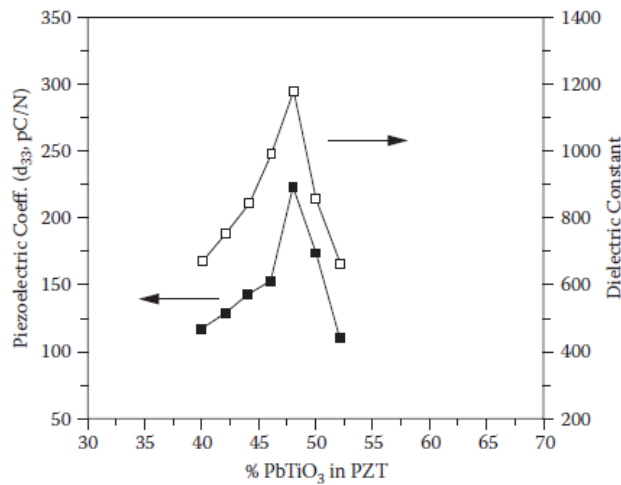


Figure 2-3 d_{33} piezoelectric coefficient and dielectric constant of PZT as function of its composition.

Piezoelectric d_{33} values up to 300 pC/N can be achieved in case of 48% of PbTiO_3 and 52% of PbZrO_3 .

Despite its high piezoelectric performances, PZT ceramic disk presents very brittle and fragile morphology that in the case of particular application could lead to mechanical problems for the structure where it is employed.

According to their manufacturing process, it is possible to produce different shapes of PZT devices, accordingly to their application need.

Barium titanate

Barium titanate (BaTiO_3) is ceramic piezoelectric material with a perovskite crystalline structure. Its piezoelectric performances are not comparable with the PZT ones, so it is not usually used as an actuator or transducer [40]. However, its capability to resist at high temperatures makes it suitable for applications such as temperature measuring and control devices for heating systems. Typical d_{33} values are in the order of 150-180 pC/N.

2.2.3 Polymeric piezoelectric materials

If compared with ceramic piezoelectric materials, the piezoelectric polymers generally present lower piezoelectric performances, but their flexibility and their possibility to be produced in thin film shape make them preferable for a variety of applications. The most common piezo-polymer is the polyvinylidene fluoride (PVDF), but also its copolymers such as polyvinylidene fluoride-trifluoroethylene (PVDF-TrFE) are widely used.

Polyvinylidene fluoride

PVdF is a semi-crystalline polymer whose molecular formula is $[\text{C}_2\text{H}_2\text{F}_2]$ and can be present in four different phases according to its chain disposition (α , β and γ), as shown in Figure 2-4. The β and γ phases are polar, whereas α is the non-polar phase. Indeed, in the case of piezoelectric applications, the β phase of PVdF is the most recommended, as its dipole moment is higher than the other phases ones. Specific manufacturing methods have been implemented in order to increase as much a possible the β phase content, for instance by mechanically stretching the sample to convert most of the α phase into β phase and by applying a strong electric field. Indeed, PVdF is a ferroelectric material and its crystals polarity can be oriented by applying an external electric field. Typically, the d_{33} value of PVdF is in the range of 20-30 pC/N.

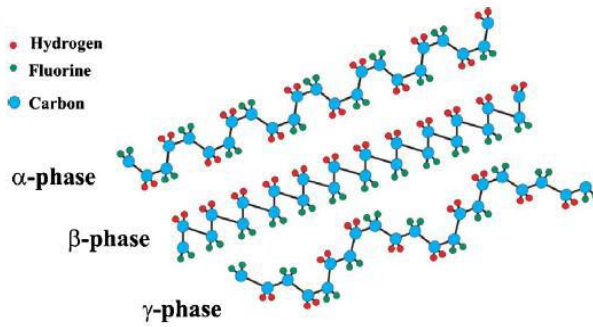


Figure 2-4 PVdF phases.

Polyvinylidene fluoride-trifluoro ethylene

PVdF-TrFE is a copolymer of PVdF that exhibits a better piezoelectric response than pure PVdF thanks to the addition of the group trifluoro-ethylene (Figure 2-5) to its chain. The addition of TrFE in concentrations between 60% and 80% favors the formation of the crystalline β phase, independently of the manufacturing method.

Moreover, differently from PVdF where the Curie temperature is higher than the melting temperature, the Curie temperature of the PVdF-TrFE is considerably below the melting point, depending on the amount of TrFE. In this way, an effective polarization process can be carried out by applying an external electric field on the material at the Curie temperature, in order to favor the dipoles movement and enhance the piezoelectric behavior of the material. Typically, the d_{33} value of PVdF-TrFE is in the range of 20-45 pC/N.

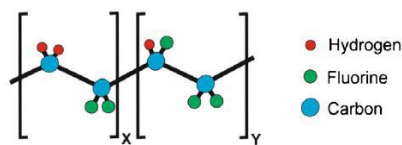


Figure 2-5 PVdF-TrFE molecular chain.

2.3 Piezoelectric applications

Piezoelectric materials are used for many applications based on their capability to convert mechanical energy into electric energy (direct piezoelectric effect) and to convert electrical energy into mechanical energy (indirect piezoelectric effect). In this section, an overview of the possible applications of the piezoelectric material is reported.

2.3.1 Direct piezoelectric effect

Pressure sensors

The working principle of pressure piezoelectric sensors is based on the direct piezoelectric effect. As a pressure is applied to the piezoelectric membrane, an output voltage can be measured as result of the material deformation. Pressure sensors can be used for the detection of dynamic pressure fluctuations, pulsations and turbulences in high static pressure environments [40]. They are ideal for monitoring dynamic pressure events that occur during the operation of compressors, pumps, pipelines and gas turbines. Quartz piezoelectric pressure sensors are widely used in many applications thanks to their stiffness and high sensitivity. Quartz pressure sensors are usually designed by means of a diaphragm leaning on a quartz column for the measurement of low acoustic pressure changes. Even though pressure piezoelectric sensors are primarily recommended for dynamic load measurements, some quartz piezoelectric materials can be used also for low-frequencies applications and quasi-static loads, by properly tuning the acquisition circuit.

MEMS pressure sensors can be designed by using PZT thin films. Their manufacturing starts from a silicon wafer (thickness about 500 μm) and a silicon oxide substrate deposited on it. Then, a PZT thin film (up to 5 μm thickness) is added to the structure by using platinum electrodes, as schematically reported in Figure 2-6.

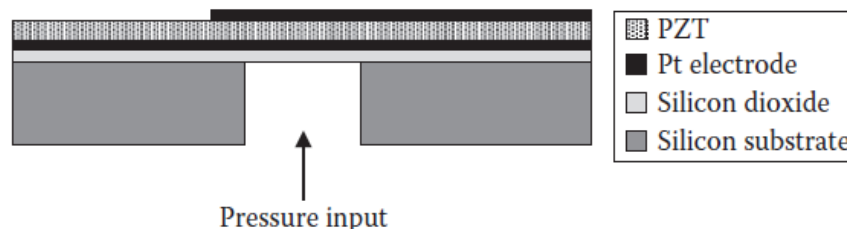


Figure 2-6 PZT thin film based MEMS.

Moreover, in the last years strong efforts have been made in order to integrate PZT disk in composite structures, to create a material that is able to detect pressure variations or compressive loads on its surface. For instance, Saeedifar et al. validated a network made of eight PZT wafers attached on a CFRP composite plate surface for a precise damage localization [42].

Despite their high performances in terms of sensitivity and stability over the time, the ceramic PZT disk fragile and brittle morphology makes such a sensors not suitable for flexible applications. For this reason, in the last period many efforts have been spent on the research of piezoelectric polymer-based pressure sensors. Due to their structural flexibility, biocompatibility, chemical stability, and piezoelectricity, PVdF and PVdF-TrFE based have shown great potential for e-skins capable to detect low-pressure variations [43]. Moreover, thanks to their easy manufacturing process, PVDF materials can be produced in different shapes and by means of the electrospinning process it is possible to produce nanofibrous layers that can be embedded in a flexible hosting matrix.

Accelerometer

Accelerometers are used for the measurement of vibrations in many applications, such as vibrations testing, machine health monitoring and fault diagnosis, structural analysis and measurements on the vibrations transferred to the human body by vehicles and hand-held power tools. The piezoelectric accelerometer is widely accepted as the best available transducer for the absolute measurement of vibrations, thanks to its proper working over a very wide frequency range, its excellent linearity over a wide dynamic load range and self-powering capability. As schematically represented in Figure 2-7, the accelerometer layout consists of a noted seismic mass that is clamped over a piezoelectric disk [44]. The open circuit voltage measured across the thickness of the disk is correlated to the acceleration of the oscillating mass, the area of the piezoelectric disk and the piezoelectric coefficient of the disk. The operating frequency range is the frequency range where the sensitivity remains constant and depends on the mechanical and electrical characteristics of the system. Indeed, low-frequency limits are defined by the RC time constant of the circuit and represent the region of the drop of the sensitivity. On the other hand, an increase of the sensitivity values can be found in correspondence of the high-frequency limits, which are defined by the resonance frequency of the accelerometer. Indeed, when the forcing frequency becomes comparable with the natural resonance frequency of the accelerometer the displacement between the seismic mass and the base plate increases, thus leading to higher output voltages. The operating frequency range can be adjusted according to the needs by varying the seismic mass. For instance, shock accelerometers usually require high-frequency ranges that can be obtained by decreasing the seismic mass. However, the choice of a lower seismic mass reduces the absolute value of the sensitivity for all the frequency ranges. Compromises between the

operating frequency range and the sensitivity amplitude are then to be founded according to the application of the accelerometer.

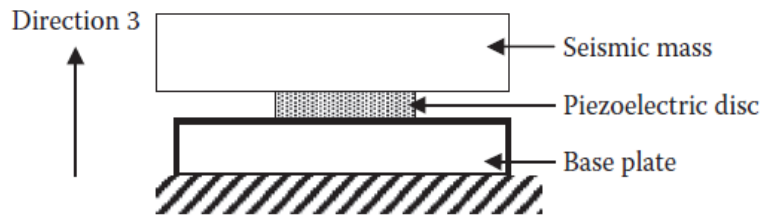


Figure 2-7 Schematic representation of an accelerometer.

Energy harvesters

As previously mentioned in section 1.1.1, the direct effect of piezoelectric materials can be used as working principle for many energy harvesting devices. Movements generated by walking or vibrations caused by high-traffic streets and machines are the most typical mechanical sources of possible energy harvesting devices. In the last year, various ideas have been proposed and published on this new concept of sustainable energy source. However, despite its variety of possible applications, the conversion efficiency of a piezoelectric device is still considerably low and such devices are to be considered suitable only for feeding low-power applications. Among the piezoelectric materials, the ceramic PZT is the most promising one for energy harvesting purposes, as its piezoelectric coefficient d_{33} is considerably higher than the other materials. Indeed, numerous kinds of devices based on PZT disk were fabricated in different designs, like cymbals geometries ([45],[46]) or cantilevers. The cantilever has a natural frequency of resonance which depends on its geometrical design and its proof mass mounted on it (Figure 2-8). Consequently, high conversion efficiency can be achieved in specific operating conditions. With this purpose, Jiang *et al* (2005) also investigated methods of increasing the cantilever efficiency [47]. Model and experimental results showed that by reducing the thickness of the elastic layer of the bimorph and increasing the proof mass fixed on the end of the cantilever, the resonance frequency is decreased and high energy conversion efficiencies were reached also at low frequencies [48].

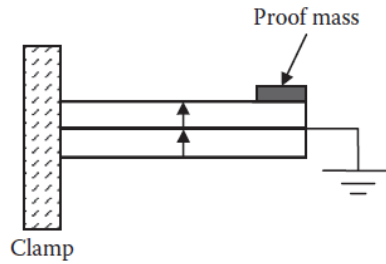


Figure 2-8 Piezoelectric cantilever for energy harvesting.

Motter et al. demonstrated the feasibility of vibrational energy harvesting based on a piezoelectric cantilever beam with the aim to light a LED to possibly show the charge status of a storage system, like a battery or a capacitor [49].

Another typical configuration for piezoelectric energy harvesting is the cymbal. Typical cymbals applications can be found in case of high mechanical loads, such as prosthesis sole or the integration with the shoe sole. The cymbal design consists of two metallic plates (i.e. aluminum) encapsulating a ceramic piezoelectric disk, as shown in Figure 2-9. As a compressive force is applied on the upper plate and it is transferred to PZT disk also in a radial direction. In this way, two piezoelectric contributions are involved: d_{33} and d_{31} , resulting in higher efficiency. With respect to cantilevers, cymbals can generate output powers considerably higher, as their structure is able to sustain high mechanical load. For instance, Li, Tian and Deng designed a cymbal structure (29 mm diameter and 1 mm thickness) able to generate 52 mW under a 70 N compressive force oscillating at 100 Hz [47].

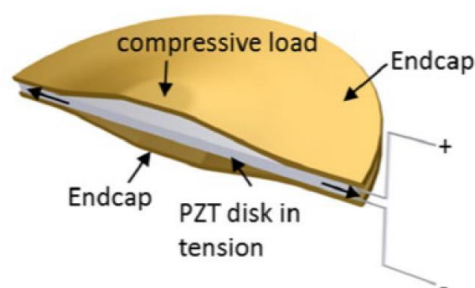


Figure 2-9 Cymbal configuration for energy harvesting.

However, cymbals and cantilever rigid and brittle morphology dramatically narrows their application fields, especially if based on PZT ceramic disk. For this reason, strong efforts have been made to develop piezoelectric generators based on polymeric materials, which are flexible and suitable for application such as integration in a sole of a shoe or wearable nanogenerators. Pi et al. [50] fabricated a flexible nanogenerator based on spin-coated PVdF-TrFE film exhibiting a

current density of $0.56 \mu\text{A}/\text{cm}^2$ and 7 V of open circuit voltage. As previously mentioned, the β phase amount in the crystalline structure strongly affects the piezoelectric performance of PVDF. Different techniques have been explored in order to maximize the β phase formation and increase the dipole alignment, consequently increasing the piezoelectric response. Among these, electrospinning represents a promising solution as the strong electric field and the mechanical stretching of the nanofibers increase the β phase amount in the crystalline structure of the polymer. Moreover, conductive nanofillers such as carbon black or graphene have been used to aid the charge transfer and non-conductive nanofillers such as barium titanate (BT) or zinc oxide (ZnO) have been added in order to enhance nucleation and the dipoles alignment [39], [51]. Choi et al. synthesized a flexible piezoelectric nanocomposite with a 50 vol% content of BT nanowires embedded in the PVDF matrix that achieved a d_{33} value of 61 pC/N [52].

2.3.2 Indirect piezoelectric effect

Piezoelectric actuators

Piezoelectric actuators convert the electrical input in a change of the dimension and a mechanical displacement of the materials, leading to the development of novel kinds of technologies for many applications. They are typically manufactured as piezoelectric cantilever actuators or linear actuators according to their purpose. The strain of the piezoelectric material for high voltages is around 0.1% and 0.2%. The strain can be increased, for a given voltage, by disposing different piezoelectric element in a stack.

A piezoelectric stack actuator consists of several thin piezoelectric rings stacked one above the other, where each element is polarized in the opposite direction of the adjacent ones and the alternate faces are electrically connected as shown in Figure 2-10. The voltage is then applied to each face of the elements and each displacement is thus added up. The total thickness of this configuration is in the order of the millimeters, generating a displacement of micrometers. Piezoelectric stack actuators have applications as valves, switches, relays and can be used in composite structures or robotic applications.

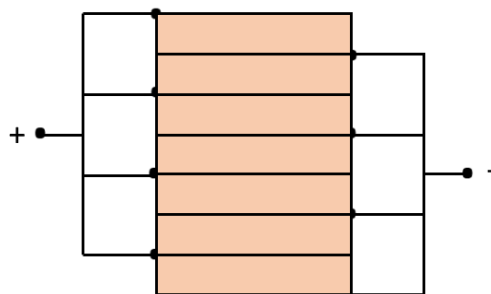


Figure 2-10 Schematic piezoelectric stack actuator.

Piezoelectric uniform actuators are designed by stacking a piezoelectric film over an elastic substrate of non-piezoelectric material. One end of the cantilever is clamped and when the voltage is applied the bending of the cantilever is used for actuation. The electric voltage induces a strain on the piezoelectric material and the non-piezoelectric layer resists the strain, thus leading to the bending of the cantilever. PZT and PVdF based piezoelectric materials are used for this kind of application.

Cymbal configurations have been explored for piezoelectric actuators design by encapsulating two piezoelectric ceramic disks between two cymbal-shaped metal end caps [53]. The two disks are polarized in the opposite directions and the voltage is applied in the common surfaces with the two outer surfaces grounded. In the cymbal configuration both the d_{33} and d_{31} coefficients are involved. Indeed, when the voltage is applied across the disk, the d_{33} coefficient induces a displacement in the axial direction that causes a lateral contraction of the disk in the radial direction (d_{31} coefficient) that also contributes to the actuation mechanism. A proper choice of the metal caps determines the sensitivity of the actuator, which still results higher than the cantilever and stacked actuator ones.

3. Electrospinning

3.1 History of electrospinning

Electrospinning is a technique for the production of solid nanofibers starting from a liquid solution. The first electrospinning procedure was established and described in a list of patents from 1934 to 1944 by Anton Formhals, who designed an electrospinning apparatus for the production of artificial threads starting from a liquid solution where the solid part is dissolved in appropriate solvents [53]. The solution is passed into an electrical field formed between two electrodes in a thin stream or drops in order to separate them in a plurality of threads for the production of silk-like spun fibers.

Considerable improvements to the electrospinning process were introduced by Geoffrey Taylor in the 1960s, whose contributions regarded the mathematical modeling of the shape of the cone formed by the fluid droplet under the effect of an electric field [53]. Such a characteristic shape of the drop during the electrospinning process is known as the “Taylor cone”. In the late 1990s Reneker and Rutledge characterized in detail the electrospinning process of organic polymers by evaluating the morphology of the nanofibers for different setup conditions of the process [54].

Electrospinning is an established technique that since the early 20th century has been studied first on a laboratory scale and later also for industrial production. It is a quite simple process for the manufacturing of nanofibrous layers of different materials, but its modeling and understanding requires knowledge in mechanical, chemistry and electrostatic fields. The obtained nanofibrous membrane can be used for various applications, according to the materials they are made of, the morphology of the nanofibers and the interaction with the environment where they are placed in. The very high surface-volume ratio of the nanofibers is a key component that enhances the material properties [55] and opens the possibility to use them in fields like tissue engineering, biosensing, theragnostic, and functional textiles [56], [57]. For instance, in biomedical nanofibrous membranes have been used for tissue regenerations (nerves, muscles and skin [58], [59], [60]), for cancer diagnosis [61], wound healing [62] and filtration membranes [63].

3.2 Working principle

Generally, the electrospinning apparatus consists of a spinneret, like a syringe and a needle, a syringe pump, a high voltage generator and a ground collector where the nanofibers are deposited, as schematically represented in Figure 3-1. The polymeric solution or the melt is loaded by the syringe pump at a constant rate to the needle tip and extruded in a hanging drop shape.

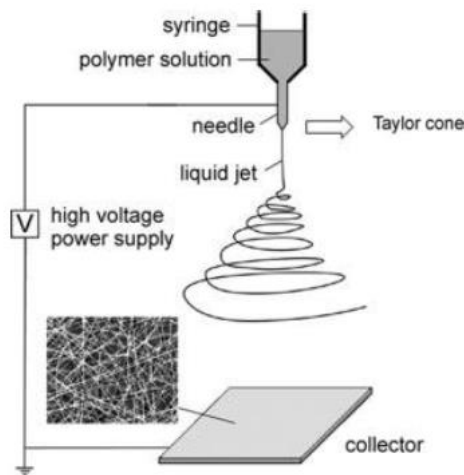


Figure 3-1 Electrospinning apparatus.

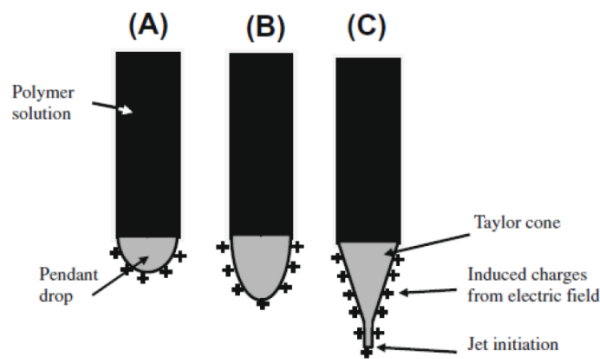


Figure 3-2 Taylor cone formation.

When the applied voltage (in the kV range) reaches the proper value, the drop is stretched and its spherical original shape is deformed in the typical Taylor cone shape (Figure 3-2). The electrostatic force induced by the electric field overcomes the surface tension of the drop and a thin jet of fluid polymer separates from the drop and flows toward the ground collector. The region between the high voltage needle and the ground collector where the fluid jet passes through is known as *whipping instability zone*. In this region, the fluid jet runs in a spiral path and bending deformation occurs as result of the interaction between the electrostatic charge of the fluid and the external electric field. During this instability zone, the solvents in the fluid jet evaporate and

solid nanofibers with a diameter in the order of a few hundreds of nanometers are then deposited on the ground collector. Therefore, the distance between the high voltage needle and the collector has to be finely tuned to guarantee the complete evaporation of the solvents. The nanofibers deposited on the collector will appear as a nanofibrous membrane whose thickness depends on the electrospinning duration time and their randomly oriented deposition is the result of the instability of the jet movement in the whipping zone.

3.2.1 Electrospinning parameters

The electrospinning process depends on a various number of parameters, such as the environmental conditions where the process is carried out (temperature, humidity etc.), the process parameters (like the applied voltage, the flow rate of the syringe etc.) and the composition of the solution (viscosity, boiling point of the solvents, etc.) [64]. In this section the way those parameters affect the process stability and the morphology of the nanofibers is described [55].

Process parameters

- *Applied voltage*: the applied voltage stretches the liquid drop coming out to the needle as the columbic force of the solution interacts with the electric field. The amplitude of the electric field strongly affects the morphology of the nanofibers, as generally a high voltage value corresponds to lower diameters of the nanofibers [54] [65]. Low values of electric fields could result in high diameters of the nanofibers collected and, as consequence, could lead to not proper evaporation of the solvent in the whipping zone [66]. Moreover, the increase of the electric field value affects the crystallinity degree and the molecular dipoles orientation in the polymeric chain. For instance, in the case of piezoelectric polymeric nanofibers, an electrospinning process carried out at high electric field values is claimed to produce nanofibrous membranes with enhanced piezoelectric properties [67];
- *Needle-collector distance*: the main aspect to be considered when calibrating the distance between the high voltage needle and the ground collector is the evaporation rate of the solvents during the flight of the jet. A restricted whipping zone does not allow the solvents to completely evaporate and increases the risk of unstable electrospinning (like a bending Taylor cone or electrical discharges between the needle and the ground collector). However, it is confirmed that within a specific range, increasing the distance helps to improve the uniformity of the electrospun fibers and decreases the average diameter, slightly affecting the fibers morphology [68].

- *Flow rate:* the flow rate set on the syringe pump determines the amount of solution placed in the electric field and the droplet dimensions. The higher the flow rate, the higher the diameter of the fibers, as the amount of electrospun solution increases. The flow rate is also a key parameter to obtain a stable Taylor cone for the whole process.
- *Needle diameter:* the needle diameter reduction usually results in lower fibers diameters as the drop of polymeric solution exposed to the electric field will create a small Taylor cone.

Ambient parameters

- *Temperature and humidity:* the ambient parameters of the ambient where the process is carried out, such as temperature and humidity, strongly affect the morphology of the nanofibers. High humidity environments reduce the evaporation rate of the solvent, whereas high temperature and dry environment could create problems in the jet flow through the needle, like clogging or early evaporation of the solvents.

Solution parameters

- *Viscosity of the solution:* the viscosity of the solution is one of the most critical aspects of the electrospinning process, affecting both the stability of the process and the morphology of the fibers. For low viscosity values, electrospray can occur as the polymer would deposit on the ground collector as beads and not in nanofibrous shape. In this case, the surface tension of the Taylor cone is affected by the excessive concentration of solvent molecules that does not allow a continuous polymeric jet. Therefore, smooth and regular fiber morphologies can be obtained by increasing the viscosity value of the solution, guaranteeing continuities along with the jet flow and a good solvent evaporation. Nanofibers will then be deposited in smooth morphology and higher diameter, making the beads disappear. On the other hand, very high values of viscosity could cause the problem of pumping the solution through the needle and the formation of extremely elongated Taylor cone shapes that prevent a stable electrospinning process. Indeed, if the viscosity of the solution is too high, the surface tension of the drop makes it difficult to be stretched by the electric field and the jet cannot be generated in a whipping zone.
- *Polymer molecular weight:* the molecular weight of a polymer indicates the length of the polymeric chain and it strongly affects the viscosity of the solution. The

electrospinning of low molecular weight polymers can result in electrospray, as the short molecular chains do not generate entanglements.

- *Solvent feasibility*: the solvents used to dissolve the polymer are to be properly chosen both in terms of solubility with the polymer and in terms of electrospinnability. Indeed, according to their conductivities and relative dielectric constant, each solvent reacts differently when exposed to an external electric field.
- *Solvents evaporation rate*: the evaporation of the solvents during the path towards the ground collector is a crucial aspect for a good morphology fibers formation. If the solvent deposits on the ground collector without totally evaporating, a wet membrane will be formed. The needle-collector distance regulation is not always the solution of this problem, as it impacts strongly on the stability of the Taylor cone. Therefore, a combination of low-boiling point and high-boiling point solvents is a consolidated strategy to achieve good fibers morphology.
- *Solution conductivity*: the polymeric solution during the electrospinning process has to accumulate charges under the effect of the electric field in order to overcome the surface tension of the drop and to start the jet formation. The stretching of the Taylor cone is subsequently associated to the conductivity of the solution. In case of very low conductivity values, it is possible to add to the solution a small amount of salt in order to increase its capability to carry charges.

3.2.2 Kinds of collectors

The nanofibrous membranes obtained via electrospinning process are generally characterized by a randomly oriented disposition of the nanofibers. Moreover, the low deposition rate of the nanofibers in the edges of the ground collector frequently leads to the production of not uniform thickness membrane. However, various techniques have been explored to govern the orientation of the nanofibers and to uniform the thickness of the mats by changing the ground collector structure, as described in this section.

Plane collector

The plane ground collector is usually made of a metallic plate connected to the ground, where the nanofibers are deposited and randomly oriented, as shown in Figure 3-3. It is typically considered

as a standard collector and the nanofiber distribution is not uniform on its area as the center part of the plane, in front of the needle, is the one with the higher nanofiber deposition.

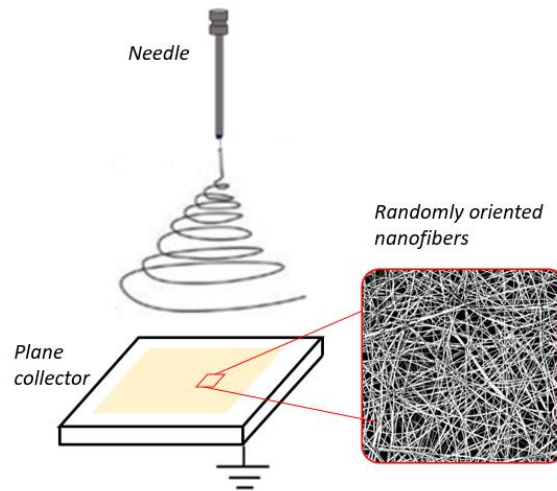


Figure 3-3 Plane ground collector.

Rotating drum

The use of a rotating drum as a ground collector presents several advantages if compared to the plane collector. The low rotating speed of the drum promotes a uniform distribution of the nanofibers in the direction perpendicular to the drum length. Moreover, by connecting two or more needles to a structure with a translation movement, the distribution of the nanofibers is optimized also in the direction parallel to the drum length and the thickness of the layer is uniform all over the deposition area, as represented in Figure 3-4. The dimension of the rotating drum can be varied to obtain larger nanofibrous membranes for massive production.

If the speed of the drum is substantially increased (i.e. 2500 rpm), the nanofibers deposit on the drum collector in an aligned direction. As the polymeric jet reaches the drum surfaces, it is mechanically stretched by the high speed of the drum in the direction of rotation. The alignment degree of the nanofibers can be enhanced by increasing the rotating speed of the drum.

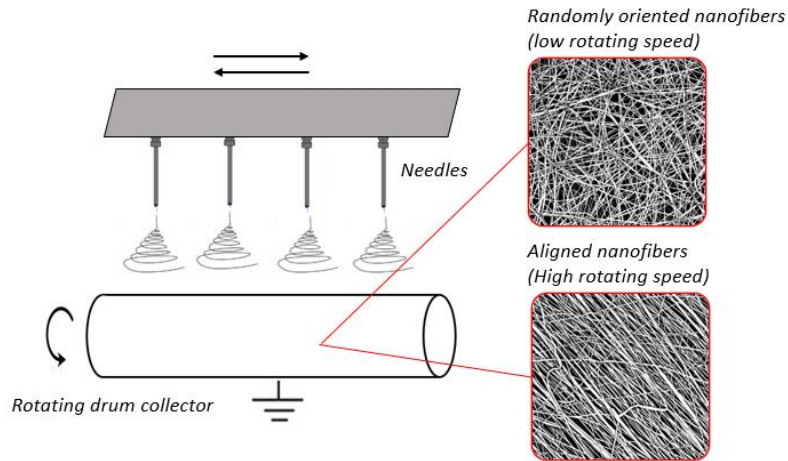


Figure 3-4 Rotating drum collector.

Parallel ground electrodes

Another technique typically used for the production of aligned nanofibers is the use of two parallel ground electrodes (such as wires or parallel plates). Once the solvents evaporate, the nanofibers are collected in the area between the two electrodes and deposit perpendicularly to the direction of the electrodes, as shown in Figure 3-5. In this case, the alignment mechanism of the nanofibers does not mechanically impact the nanofiber morphology, but it is the result of the electrical field distribution. On the other hand, large deposition areas of aligned nanofibrous mats are not feasible, as the two parallel electrodes cannot be placed too far from each other.

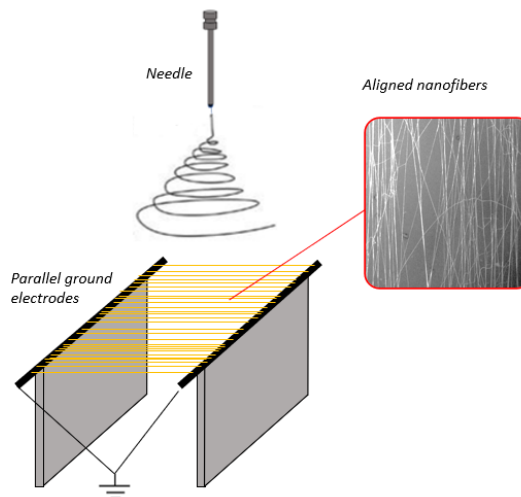


Figure 3-5 Parallel ground electrodes for aligned nanofibers.

3.3 Core-shell electrospinning

Beyond the traditional electrospinning process, alternative techniques have been explored for several years for a multifluid electrospinning that opens the possibility to create complex structures [56]. So far, coaxial electrospinning is the most widely studied.

The coaxial electrospinning apparatus consists of two syringes for two different polymeric solutions, whose flow rates are controlled by two different pumps. The coaxial needle presents two inputs for the polymeric solutions as shown in Figure 3-6. Consequently, the Taylor cone shape presents an inner needle and an outer needle concentrically disposed for the loading of the core solution and shell solution, respectively.

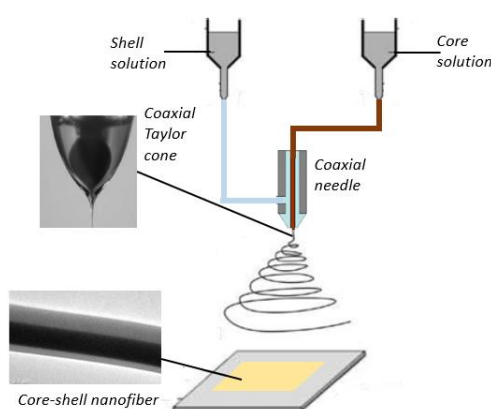


Figure 3-6 Coaxial electrospinning apparatus.

Coaxial electrospinning provides the opportunity to develop nanostructures with tunable functional performances, such as core-shell nanofibers [69] or hollow fibers [70], [71]. Diverse functionalities are exploited for various applications fields, such as tissue engineering, bioregenerations and bio-sensors [56]. Core-shell nanofibers can be used to improve filtration efficiency in seawater desalination by using a hydrophilic shell and a core to improve the fibers strength [72]; Li et al. conceived the coaxial electrospinning as a novel method to produce heterojunction, which is a better way to transfer charge, between core and sheath [73]. Hollow or porous structures can be obtained if a post-treatment like washing or calcination is applied [74]. During those preparation processes, the inner and outer liquids are usually either immiscible or completely miscible. For example, mineral oil was used as an immiscible inner liquid to prepare a hollow cross-section morphology [75]. While for the miscible system, it is difficult to regulate the cross-section morphology of NFs [76]. In the pressure sensors field, investigations have been performed to produce flexible sensors based on core-shell nanofibers with a conductive core and a piezoelectric shell [77]. This configuration is designed and developed also in this work.

4. Self-sensing nanostructured piezoelectric materials

The experimental campaign on the development of piezoelectric self-sensing composite materials has been carried out by using both piezo-polymeric (PVdF-TrFE) and piezo-ceramic (PZT) materials, with the aim to study advantages and drawbacks of each configuration. The piezoelectric co-polymer has been chosen for its flexibility, which can be exploited for flexible sensors or wearable applications. On the other hand, the ceramic PZT, which has a fragile and brittle nature but presents high piezoelectric performances, can be used for the development of highly-sensitive composite material.

The work has focused on the design of three different self-sensing materials typologies, based on piezoelectric PVdF-TrFE nanofibers, core-shell piezoelectric nanofibers (PVdF-TrFE as shell and conductive PEDOT:PSS as core) and ceramic PZT powders. In this section the manufacturing process and the characterization techniques are described.

The piezoelectric self-sensing composite laminate described in section 4.1 is based on PVdF-TrFE nanofibers obtained with the traditional electrospinning technique, as described in section 3.2. First, a flexible piezoelectric nanofibrous sensor has been manufactured by investigating its piezoelectric coefficient, polarization process and mechanical structure. Furthermore, the flexible sensor was integrated between the plies of a composite material made of CFRP and Glass Fiber Reinforced Plastic (GFRP). A lumped electric model is proposed for a complete characterization of the polarization of the nanofibers and the piezoelectric response of the laminate. A strong focus was put on the choice of the material used to fabricate the piezoelectric sensor. Indeed, with the aim to integrate the sensor with the prosthetic sole of MyLeg project, brittle elements are to be avoided, as delamination between the laminate plies could occur. For this reason, a flexible configuration of the sensor was explored by using an embedding medium that is also compatible with the resin of the composite material of the prosthesis. With the same purpose of maintaining

the mechanical integrity of the structure, traditional electrodes, typically brass sheets or aluminum foils, are replaced with non-invasive electrodes like, e.g., metallic fine mesh and carbon-black based electrodes.

At the same time, studies were conducted for the development of a peculiar kind of flexible piezoelectric sensor (see section 4.2), based on core-shell nanofibers to obtain flexible position microsensors. The coaxial electrospinning apparatus working principle is described in section 3.3, where a conductive polymer (PEDOT:PSS) is used as the core solution and the piezo-polymer PVdF-TrFE for the shell solution. By properly aligning the produced nanofibers in a geometrical matrix disposition and by integrating them in a flexible hosting material, such a piezoelectric sensor is able to locate the exact position of a mechanical impact on its surface. As previously mentioned, also in this case strong efforts have been made to guarantee the flexibility of the structure and the realization of non-invasive electrodes.

The third kind of self-sensing composite material investigated in this work was made by dispersing PZT powder in the epoxy matrix of the laminate. In particular, the PZT powder was inserted between the GFRP prepreg plies of the laminate together with thin brass sheets electrodes to collect the piezoelectric signal. The effects of PZT morphology (disk and powder) and PZT/GFRP volume ratio were explored in terms of impact resistance of the hosting laminate and sensors performance. Two interconnected models (polarization and piezoelectric models) were adopted to correlate the volumetric fractions of the two phases (PZT and GFRP) with the piezoelectric signal of the composite laminates.

4.1 Self-sensing laminate based on piezo-polymeric nanofibers

4.1.1 Context

The sensing efficiency of the piezo-polymers is becoming highly attractive in fields of civil engineering, SHM systems or robotic systems, thanks to the self-powering characteristic of their transducing mechanism. The advantageous features of polymers such as PVdF (and its copolymers) include its variety of size and shape (e.g., films, nanofibers, etc.) its flexibility and the possibility to be embedded in very remote locations [78], [79]. In situ and real-time SHM was successfully performed by embedding in tensile specimens a PVDF disk. The non-intrusiveness of the embedded transducer and its stretchability extended the limits of its working domain, if compared with ceramic devices [80]. Moreover, interesting studies have been dedicated to the development of PVdF-based piezoelectric pressure sensor for the development of electronic skin and flexible wearable devices [43], [81].

The possibility to produce nanofibers via electrospinning starting from a polymeric solution with PVdF was also widely explored in pressure sensors fields [82]. For example, Maity et al. introduced e-skin-based metal-free to fabricate a piezoelectric sensor; where highly aligned PVdF nanofibers (NFs) arrays were used as the piezoelectric active mat, and conductive polyaniline coated PVdF (PANI-PVdF) NFs as a flexible electrode [83], [84]. Highly sensitive PVdF nanofibrous mats embedded in polydimethylsiloxane (PDMS) (up to 254 mV/N) were manufactured by using flexible polymeric conductive electrodes [85].

In composite structures, the use of electrospun piezoelectric mats avoids mechanical problems related to the interface strength between the polymeric film and the hosting material. Indeed, the intimate contact between the nanofibers and the hosting matrix prevents the delamination risk and increases the impact strength of the composite material [86], [87].

In this section, the design of a self-sensing composite material based on PVdF-TrFE nanofibers is proposed. A nanofibrous flexible piezoelectric sensor was produced and subsequently integrated with a hosting laminate. The manufacturing steps of the pressure nanofibrous sensor are illustrated in the following sections, taking into account the electrospinning process of the nanofibrous piezoelectric membrane of PVdF-TrFE, the polarization techniques of the nanofibers, the integration of the nanofibers in different hosting materials and the realization of non-invasive electrodes. In the end, the proposed piezoelectric model and the electromechanical characterization techniques used for the sensor testing are reported.

4.1.2 Electrospinning

PVdF-TrFE Solvener (80/20 mol%, $M_w=600$ kDa), kindly provided by Solvay Specialty Polymers (Bollate, Italy), is used as piezoelectric material. The polymeric solution is prepared by dissolving 7% wt of PVdF-TrFE (available as polymeric powder) in dimethyl-formamide (DMF) (23%wt) and acetone (AC) (70% wt). Such a composition is the result of a deep investigation on the stability of the electrospinning process and the analysis of the produced nanofibers. After a stirring of 24 hours at room temperature, the polymeric solution is ready to be used for the electrospinning process [67].

The electrospinning apparatus used to manufacture the nanofibers is a Spinbow Lab Unit (Spinbow S.r.l., Italy). Its working principle is shown in Figure 3-1 and previously described in section 3.2. The distance between the needle and the ground collector is set at 15 cm. The electric voltage applied to the needle with the DC generator is set at 10 kV. The electrospinning process is carried out for 3 hours and the obtained nanofibrous mat presents 100 μm thickness.

4.1.3 Chemical characterization

X-ray diffraction (XRD) measurements were carried out by means of X'PERT pro Instrument, with detector 1-D PIXcell using Cu radiation 1.54 \AA . PVdF-TrFE copolymer shows a complex structure and is characterized by the presence of different crystalline phases, related to the different chain conformations that allow different packing of the dipoles within the unit cell. PVDF-TrFE has been synthesized to possess an intrinsic β -phase that shows an all TTTT conformation wherein the polar C-F and C-H bonds possess a dipole moment perpendicular to the carbon backbone, which makes it the most electrically active phase [88]. In order to investigate the influence of the electrospinning process on the crystalline phase, the nanofibrous mat and powder of PVDF-TrFE were analyzed by XRD and the diffractograms of the two samples are shown in Figure 4-1. A prominent peak at $2\theta = 19.8^\circ$ is observed, representing the (200) Bragg reflections, which is typically assigned to the β crystal phase of PVDF-TrFE, and indicates that the ferroelectric phase is the dominant phase in the copolymer [89]. A shoulder centered around 18° was evident for the powder sample, attributed to a higher amount of amorphous material in the powder with respect to the nanofibrous mat, as confirmed by the degree of crystallinity (48% for the powder and 58% for the electrospun fibers). This result indicates that the paraelectric phase of the copolymer is reduced going from powder to electrospun fibers, as indicated by the arrow in Figure 4-1.

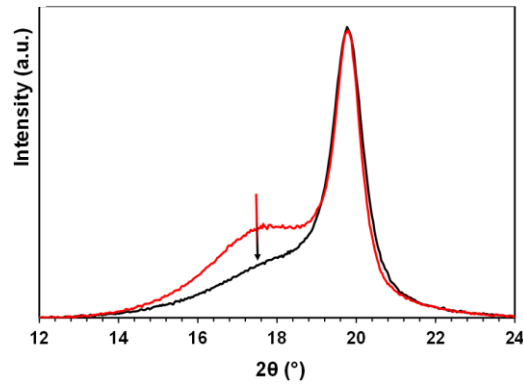


Figure 4-1 XRD diffractograms of the electrospun membrane (black line) and powder before electrospinning (red line).

4.1.4 Polarization process

The high electric field of the electrospinning process promotes the formation of polar β -phase in PVdF-TrFE, the one responsible for the piezoelectric behavior. Despite this, a poling process is still required to fully align the ferroelectric domains of the nanofibers by applying an external electric field, thus enhancing the macroscale piezoelectric behavior of the membrane. It has been demonstrated that the structural changes of the polar β -phase depend on its responsiveness to the electric field and the orientation of the polymer chains [90], [91].

Polarization working principle

To induce permanent polarization the piezoelectric material is typically heated at a temperature close to its Curie temperature [92], [93]. The Curie temperature of PVDF-TrFE (80/20%mol) used in this work is 130°C. To this aim, the nanofibrous sample was placed in the oven and, as temperature reached 130°C, the electric field was applied. After a defined period, the temperature was decreased to ambient temperature and then the DC voltage generator was switched off. This poling procedure is commonly applied to piezoelectric materials, such as stiff disks of PZT and PVDF-TrFE films. In such a kind of bulk monocomponent system the electric field would be homogeneously applied on the entire material [94]. Differently, nanofibrous mats are more complex materials, characterized by high porosity and interconnected pores. Such kind of structures can be thought as bicomponent systems where the fibers are embedded in a second phase, being it air if we consider the plain electrospun mat, or silicon rubber, silicon oil, epoxy matrix, etc., if the mat is embedded in a different material. Hence, once the electric field is applied, it will distribute unevenly between the two phases, according to their electric properties [95]. More precisely, the structure can be modeled as a multilayered system where the nanofibers and the embedding medium are represented as n -times the series of their resistivity (R_{nf} , R_{em}) and capacitance (C_{nf} , C_{em}) [96]. The resistance R_i is the opposite of the conductance G_i ($R_i = 1/G_i$),

where G_i is proportional to the conductivity σ_i and the capacitance C_i is proportional to the permittivity ε_i . The schematic representation of the poling setup of Figure 4-2a can be modeled as a multilayers system whose equivalent electric circuit is shown in Figure 4-2b.

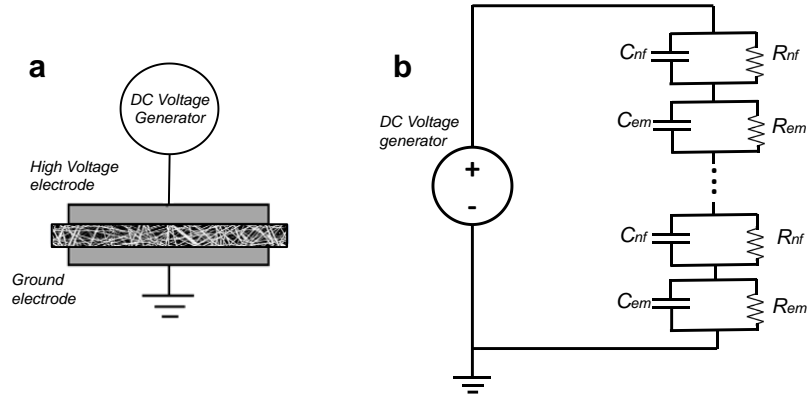


Figure 4-2(a) Schematic representation of the poling setup; (b) Equivalent circuit of the polarization process.

As the DC voltage generator is switched on, a first transient domain distributes the electric field on the different materials accordingly to their permittivity (ε). On the other hand, in the steady-state domain reached after a period of time τ [97], the electric field distribution is governed by the conductivity values (σ) of the materials (i.e. higher on the material with lower conductivity). According to the discussion on the electric field distribution on two dielectric materials reported in [98], by schematizing the poling process as a two-layer system, the time constant τ can be calculated as described by equation (4.1):

$$\tau = \tau_{nf} * \tau_{em} * \frac{\frac{1}{\varepsilon_{nf}} + \frac{h}{\varepsilon_{em}}}{\frac{1}{\sigma_{nf}} + \frac{h}{\sigma_{em}}} \quad (4.1)$$

where $h = h_{em}/h_{nf}$ and $\tau_i = \varepsilon_i/\sigma_i$. h_{em} and h_{nf} represent the thickness of the embedding medium and the nanofibers, respectively. By neglecting after a period of 10τ the capacitors C_{nf} and C_{em} , the electric field applied to the nanofibers (E_{nf}) can be simply calculated by equation (4.2), where E is the electric field applied with the voltage generator at the whole system and h_{tot} is the total thickness (100 μm).

$$E_{nf} = \frac{\frac{E h_{tot}}{\sigma_{nf}}}{\frac{h_{nf}}{\sigma_{nf}} + \frac{h_{em}}{\sigma_{em}}} \quad (4.2)$$

Polarization tests

An experimental campaign was carried out by polarizing the nanofibrous layers in different embedding mediums with the aim to identify the conditions that maximize the piezoelectric response of the membrane.

Air, silicon oil, ester oil (FR3 natural ester, Cargill) and seeds oil were chosen as environments for the experimental tests. In the case of polarization in air, the nanofibers were simply placed between the high voltage electrode and the ground voltage electrode, as shown in Figure 4-3.

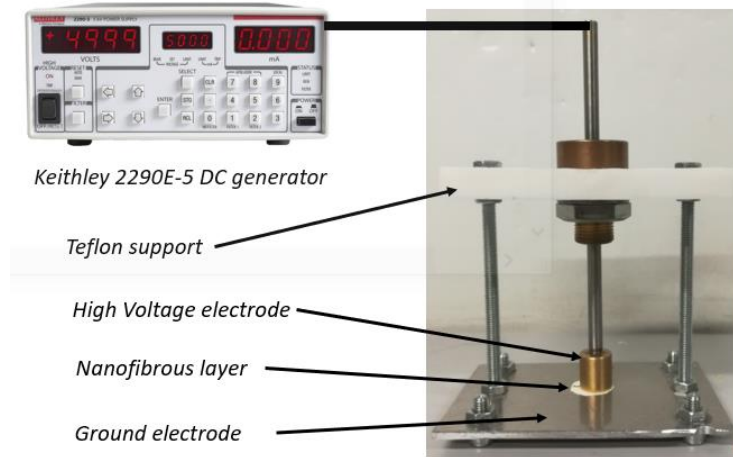


Figure 4-3 Polarization cell configuration connected to the DC voltage generator.

In the case of polarization in oil, the whole setup of Figure 4-3 was immersed in an oil bath and by means of a vacuum pump the air cavities were removed. The poling process was carried out at 130 °C by applying an electric field $E = 30 \text{ kV/mm}$ with a DC voltage generator (Keithley 2290E-5). In the case of seeds oil, the applied electric field, E , was set at 10 kV/mm, as further increases resulted in electrical breakdown. For the same reason, in the case of air the applied electric field was set at 10 kV/mm. The permittivity and the electric conductivity of PVdF-TrFE were calculated on a 200 μm thickness film at 130°C (Table 4-1). The electrical parameters of the oils are reported in Table 4-2, together with the calculated τ value and the expected electric field applied on the PVdF-TrFE nanofibers.

Table 4-1 Permittivity and conductivity of a PVdF-TrFE film calculated at 130°C.

	ϵ_r	$\sigma \text{ (S/m)}$
PVDF-TrFE (80/20%mol)	11	$6.2 * 10^{-10}$

Table 4-2 Electrical parameters, E_{nf} and τ values for each embedding medium tested.

	ϵ_r	σ (S/m)	E (kV/mm)	τ (s)	E_{nf} (kV/mm)
Seeds oil	3.3	7.7×10^{-10}	10	0.2	11.8
Silicon oil	2.5	8.2×10^{-12}	30	0.2	4.9
Ester oil	4	9.8×10^{-10}	30	0.1	35

In the case of PVDF-TrFE poling, by evaluating a τ value in the order of 10^{-1} s for all the oils, the time of the process was set at 5 minutes. As previously mentioned, the temperature was increased up to 130°C and the electric field was applied. After 5 minutes, the temperature was decreased to ambient temperature and in the end the voltage generator was switched off.

Once the polarization was completed, the nanofibrous layers were soaked in a cyclohexane bath for one hour in order to fully remove the oil and restore the initial porosity grade of the mats.

The piezoelectric response of the membrane was measured by means of a piezometer (d_{33} PiezoMeter System, Piezotest, Singapore, www.piezotest.com). Before the polarization the d_{33} measured values of the membranes was zero, whereas their value measured after the poling process is reported in Figure 4-4.

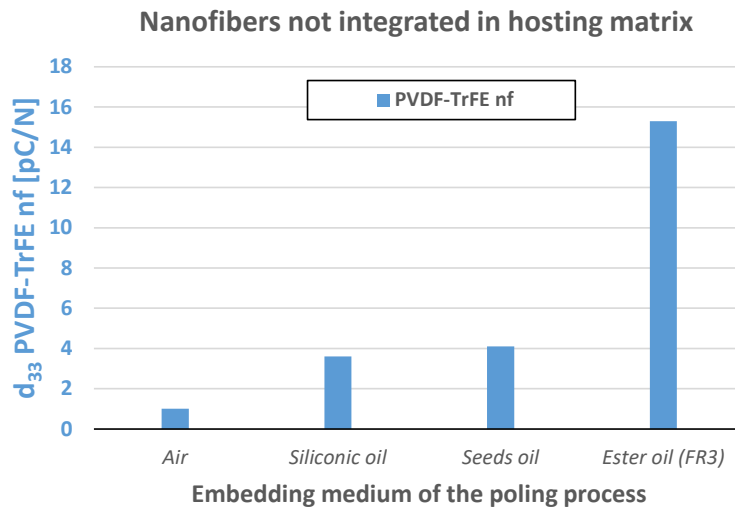


Figure 4-4 d_{33} values measured on nanofibrous mats for each different poling medium.

The highest d_{33} values are reached for the polarization carried out in a ester oil bath (FR3). Indeed, consistently with the values calculated in Table 4-2, the electric field applied on the nanofibers with this configuration is the highest one. Moreover, 15 pC/N can be considered a good value for PVDF-TrFE nanofibers, comparable with the commercial PVDF-TrFE films (20-25 pC/N).

The main advantage of this polarization technique is represented by the possibility to produce polarized nanofibrous mats that still have the same morphology they had before the process. Indeed, as the cyclohexane restores the initial porosity grade of the layer, the mechanical performances of the mats are not affected and the nanofibers can still be embedded in the desired hosting composite material. Traditional polarization techniques are expected to be carried out once the nanofibers are already immersed in the hosting matrix, whose electrical properties could strongly affect the success of the polarization process and consequently the piezoelectric behavior of the laminate.

For the sake of completeness, a polarization process was also carried out by integrating the nanofibers in a hosting material, without any treatments before the integration. The choice of this material and the integration process of the nanofibers with this blend are described in detail in the following section. The used material is a blend of epoxy resin (Itapox 108, kindly provided by Ddchem S.l.r., Verona, Italy) and blocked isocyanate polyurethane prepolymer (Synthane 2095, Synthesia Technology, Barcelona, Spain). This material presents a good flexibility and a good mechanical resistance.

As before, the poling temperature was set at 130 °C and the applied electric field was 30 kV/mm. In this case, obviously, the blend of epoxy resin and polyurethane represents the embedding medium of the polarization process. Its electrical conductivity was measured to be $2.6 \cdot 10^{-13}$ S/m at 130 °C.

In order to compare the effectiveness of the blend of epoxy resin and polyurethane used as embedding medium, also the previously polarized nanofibrous layers were integrated in this hosting material and the d_{33} of each layer was then evaluated. Indeed, once integrated in the blend the nanofibers cannot be removed (differently from the oils) and the stiffness of such a material sensibly reduces the impact load transferred on the nanofibers and thus the generated charges.

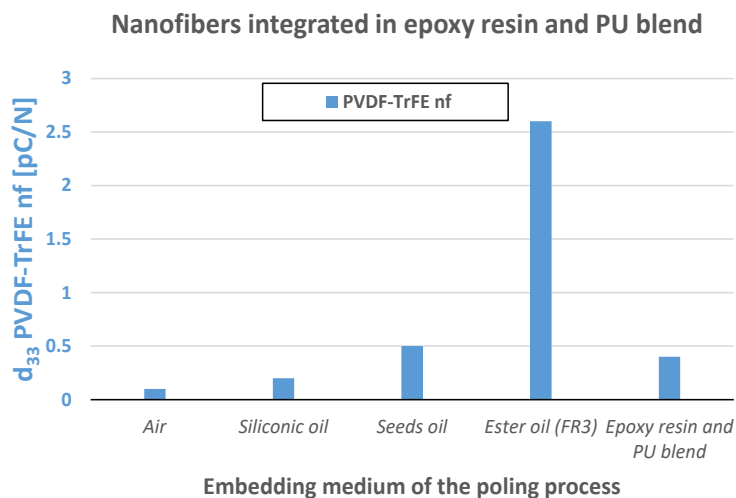


Figure 4-5 d_{33} values measured on the nanofibrous mats polarized in different embedding mediums and integrated in a flexible hosting matrix made of epoxy resin and polyurethane (PU).

As predicted, the overall d_{33} values are sensibly reduced if compared with the values of the not-integrated nanofibers [96], see Figure 4-5. The highest value of d_{33} was achieved by immersing the nanofibers in ester oil, which has a relatively high electrical conductivity σ , while embedding mediums with lower σ resulted in low electric field distribution on the nanofibers during the polarization process, as shown in the bar graph of Figure 4-5. If the polarization process takes place after the integration of the nanofibers with the blend of epoxy resin and polyurethane, the obtained d_{33} value of the system (piezo-nanofibers impregnated in the hosting polymeric matrix) is equal to 0.4 pC/N. This d_{33} value is sensibly lower than 2.6 pC/N, which is the d_{33} value of the specimen produced by first polarizing the nanofibers in ester oil and then integrating them in the same polymeric hosting material.

4.1.5 Nanofibers integration in a soft matrix

Once the nanofibers have been electrospun and deposited on the ground collector, they are to be integrated within a hosting material. Indeed, the nanofibrous membranes are not easily handable because of their high porosity and accumulated electrostatic charges. Therefore, investigations have been conducted on the integration process of the nanofibers with two different soft polymeric matrices: PDMS and a blend of epoxy resin and polyurethane (PU).

It is worth pointing out that in the final prototype of the MyLeg prosthetic sole the use of PDMS results not suitable. Indeed, the high elasticity of PDMS makes the sensor not enough stiff to resist the mechanical loads typical of the gait cycle, which is sequence of events or movements during locomotion that describes how the foot contacts the ground. Moreover, the interleaving of a PDMS layer between the laminate plies of the composite material results in delamination, as it is not compatible with the epoxy resin of the laminate and the adhesion at the interface of the two layers does not occur. However, remarkable piezoelectric studies have been carried out also on PDMS/nanofibers composite layers for other possible applications.

Integration in PDMS

PDMS belongs to a group of polymeric compounds that are commonly referred to as silicones. It is one of the most widely used silicon-based organic polymers thanks to its high-temperature resistance, biocompatibility, transparency, high flexibility and high insulating properties. In this work, PDMS Sylgard 184 was adopted as a two-component system with a polymeric base and a curing agent which cross-links with the polymeric matrix (see Table 4-3).

Table 4-3 PDMS and curing agent proportions.

	(%wt)
PDMS base	90
Curing agent	10

The curing agent and the PDMS base are mechanically mixed for 5 minutes and the air bubbles are removed by means of a vacuum pump. Indeed, air bubbles in the layer are highly undesirable as their presence could trigger electric discharge during the following polarization process. The nanofibrous membrane is placed on a PTFE support and surrounded by a 100 μm thickness pouring mask [99]. As the low-viscosity and free-air PDMS is poured on the nanofibrous substrate, the porosities are filled and the nanofibers are integrated. The slurry process is then carried out to remove the excess material on the two surfaces of the layer by means of a blade, as shown schematically in Figure 4-6. The curing process is then carried out for 1 hour at 80°C.

Integration in epoxy resin + PU blend

A hosting material stiffer than PDMS is adopted as a more suitable solution in order to guarantee a higher protection to the nanofibers in case of high mechanical loads. A blend of epoxy resin (Itapox 108, kindly provided by Ddchem S.l.r., Verona, Italy) and blocked isocyanate polyurethane prepolymer (Synthane 2095, Synthesia Technology, Barcelona, Spain) was chosen as embedding medium, and the curing agent (Itamine CA119, Ddchem S.l.r., Verona, Italy) was added after the stirring of the two components. The mixture compositions are reported in Table 4-4. The addition of the polyurethane to the epoxy resin has the aim to increase the elasticity of the matrix, still guaranteeing a good adhesion to the laminate resin.

Table 4-4 PU and epoxy resin blend composition.

	(%wt)
Epoxy resin	55
PU	24
Curing agent	21

The integration process is the same described for the PDMS integration and is schematically represented in Figure 4-6. The curing process is carried out for 2 hours at 50°C.

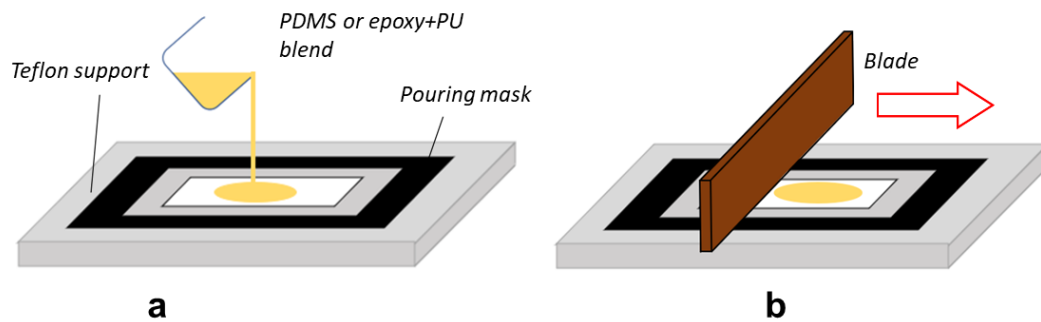


Figure 4-6 Slurry process: (a) PDMS or epoxy+PU blend pouring; (b) a homogeneous 100 μm thickness of the layer is achieved by means of a blade to remove the excess material.

4.1.6 Electrode manufacturing

In order to develop the entire structure of the sensor, the electrodes are required to be placed on the two opposite surfaces of the layer to collect the piezoelectric signal.

Electrodes such as aluminum foils or a gold sputtered layers are widely used for this purpose, but in the case of flexible devices the foils could rip or crumple and the thin metallization could present some discontinuities. Indeed, they have a limited maximum strain before breakage that would limit the flexibility of the sensor. Moreover, the interleaving of brass sheets electrodes within the laminate plies modifies the homogeneity of the structure and in case of high impacts the transferred load could start a delamination at the interface between the brass sheets and the plies of the composite material.

To overcome these problems, in this study, the electrodes were realized by dispersing conductive carbon black (CB) nanoparticles in the same material used for the nanofiber's integration. If carbon black is mixed into a polymer matrix, its high specific surface area can form a conductive network which greatly increases the conductivity of the resin, even by mixing a low amount of nanoparticles [100]. According to the polymer where the carbon black nanoparticles are dispersed, the percolation threshold can vary, but usually it is in the range between 5-15 wt% [101].

The experimental campaign was carried out for two different polymeric matrices described in the previous section (PDMS and epoxy resin with polyurethane, Figure 4-7a). The carbon black amount range was varied from 1% wt to 20% wt and the obtained layers were evaluated in terms of electrical resistance and curing process (Figure 4-7b). The dispersion process of the carbon black nanoparticles (Printex XE2B, BET surface area= 1000 m^2/g , average particles size= 30 nm) consisted of a magnetic stirring of the liquid formulation before the curing process. The addition of 300% wt of isopropanol facilitated a homogeneous dispersion of the CB nanoparticles in the matrix, as shown in Figure 4-7c. After a period of time equal to 100 hours, the curing agent was added and the liquid solution was placed on a Teflon support with a pouring mask (Figure 4-7d).

A heating process of 30 minutes at 40°C was needed in order to facilitate the isopropanol to evaporate and not to create air bubbles inside the layer during the curing process (Figure 4-7e). In the end, as represented in Figure 4-7f, a uniform free-isopropanol thin layer was obtained by means of a blade and the curing process was carried out (1 hour at 80°C for PDMS and 2 hours at 50°C for the epoxy resin end polyurethane blend).

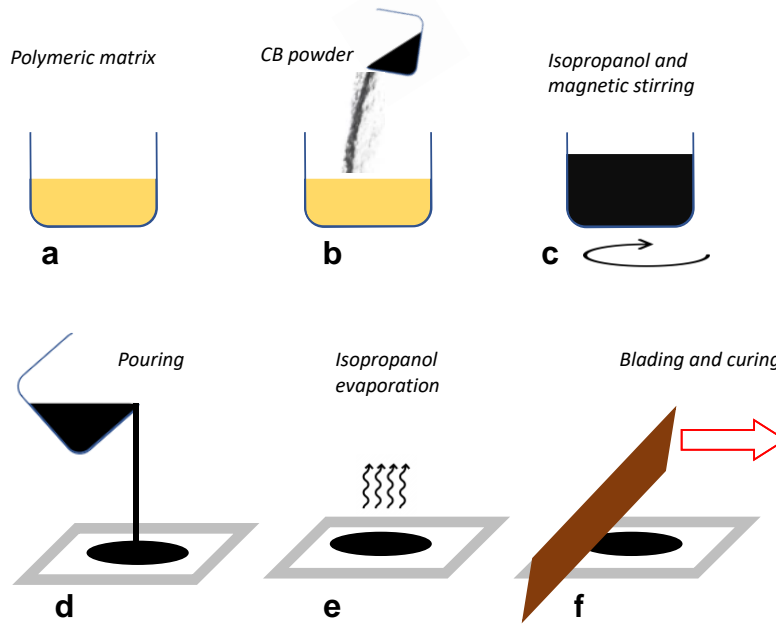


Figure 4-7 Carbon black based electrodes manufacturing process: (a) original polymeric matrix; (b) CB powder addition; (c) magnetic stirring with isopropanol; (d) mixture pouring; (e) isopropanol evaporation and partial curing; (f) curing process of the final thin layer.

The resistance was measured by placing the semi-conductive layer between two brass cylindrical electrodes (diameter of 1.5 cm) and connecting them to a multimeter set in a resistance measurement. Moreover, for each specimen the curing process was monitored in order to identify the maximum amount of carbon black nanopowder that was possible to add to the polymeric matrix without affecting its polymerization, as reported in Table 4-5.

Table 4-5 Electrical resistance of polymeric matrix mixed with carbon black nanoparticles.

CB content (%wt)	Resistance		Curing process
	PDMS	Epoxy+PU	
1%	>1 GΩ	>1 GΩ	Successful
2%	>1 GΩ	>1 GΩ	Successful
3%	>1 GΩ	>1 GΩ	Successful
4%	>1 GΩ	>1 GΩ	Successful
5%	500 MΩ	400 MΩ	Successful
7%	80 MΩ	65 MΩ	Successful
10%	5 kΩ	4 kΩ	Successful
15%	1 kΩ	1 kΩ	Partial curing
20%	/	/	Not cured

Similar trends were registered for both the polymeric matrix (PDMS and epoxy+PU). Resistance values above 1 GΩ were measured up to a carbon black amount of 4% wt, whereas 10% wt is the limit that still guarantees a successful curing process. In the 15% wt CB sample, partial curing occurred and cracks on the layer surface were visible, whereas in the case of 20% wt the materials did not cure at all.

Therefore, in order to deposit the electrodes on the surface of the piezoelectric layer described in section 4.1.5, a carbon black amount of 10% wt was chosen. The electrodes were fabricated with the aforementioned procedure and deposited on the piezoelectric substrate, as schematically shown in Figure 4-8a and Figure 4-8b. The same process was repeated for the opposite surface electrode. Furthermore, signal cables (430-FST, Micro-Measurements, Raleigh, NC 27611, USA, www.micro-measurements.com) coated with a Teflon jacket were placed within the electrode layers during the curing process. The total thickness of the sensor of Figure 4-8c results to be around 300 μm. Furthermore, the signal-to-noise ratio could get worse because of external phenomena, such as triboelectricity effects. With the purpose to reduce external electric noise, shield electrodes were added to the structure of the sensor with the same manufacturing process used for the signal electrodes (Figure 4-8d). A thin layer of polymeric matrix was also added between the signal electrodes and the shield electrodes in order to electrically insulate them from each other. The final piezoelectric sensor is shown in Figure 4-8e.

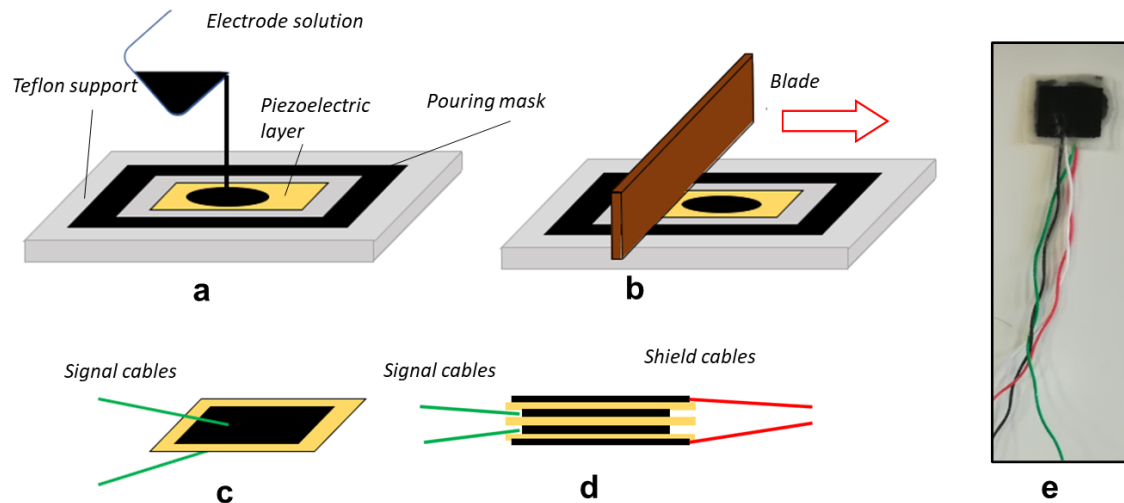


Figure 4-8 Signal electrodes and shields electrodes manufacturing (a): Electrodes solution pouring; (b) Slurry process; (c) Steps (a) and (b) are repeated on the opposite surface and the signal cables are cured within the electrodes; (d) Shield electrodes are added.

4.1.7 Self-sensing composite material

The development of a self-sensing composite material was performed by interleaving the piezoelectric sensor between the laminate plies of the laminate. In particular, two shape-different geometries were manufactured. Firstly, one sensor was integrated with a rectangular plane composite laminate with the purpose to perform standard compression tests for a broad electromechanical characterization. Then, the same stacking sequence was repeated as a proof of concept on the sole of MyLeg prosthetic foot by placing two sensors in the tip and one sensor in the heel.

The choice of the polymeric matrix used for the piezoelectric sensor manufacturing was done with the aim to be compatible with the resin of the composite laminate used in the prosthesis sole stacking.

As previously mentioned, the PDMS-based piezoelectric sensor was not adopted in the stacking sequence of the self-sensing laminate as the low adhesion of the PDMS silicon matrix with the laminate resin would result in delamination of the composite. Therefore, in this paragraph the flexible piezoelectric sensors used for the manufacturing of the laminates (both the rectangular plane and the prosthesis sole) are the ones based on the mixture of epoxy resin and polyurethane.

The piezoelectric sensor was integrated with a CFRP precured laminate, with a quasi-isotropic stacking sequence $[0/\pm 45/90]_s$ and 100 x 50 x 3 mm dimensions. A layer of GFRP prepreg (E-glass 8H balanced Satin 300 g/m² - epoxy matrix, VV300S - DT121H-34 DeltaPreg, 80 x 90 x ~0.22 mm) was stacked on the CFRP precured laminate, with a 0° orientation. Then the piezoelectric sensor was placed on it and finally covered with another GFRP prepreg ply 0° oriented, as depicted in Figure 4-9a. The presence of the GFRP layer below the piezoelectric sensor electrically insulates it from the CFRP conductive base; while the GFRP layer covering

the sensor protects it from triboelectric effects and electromechanical noises that would negatively affect the piezoelectric signal. Before stacking, the surface of the CFRP base was treated and grinded with sandpaper (P220) in order to improve the adhesion with the resin of the GFRP layer. The curing process was then carried out in a vacuum bag for 12 hours at 80 °C. The final self-sensing laminate is observable in Figure 4-9b.

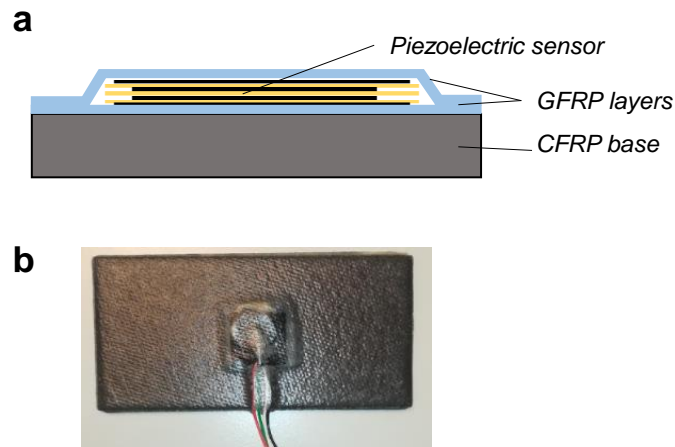


Figure 4-9 (a) Stacking sequence of the self-sensing rectangular composite material; (b) Self-sensing laminate image.

The same stacking sequence was repeated on the sole of the prosthetic foot by interleaving three sensors (Figure 4-10) and the curing process was done in an autoclave for 12 hours at 80°C.

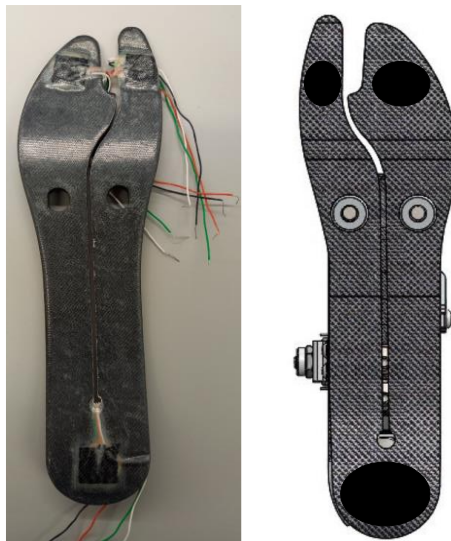


Figure 4-10 Prosthetic foot sole with piezoelectric sensors integrated.

4.1.8 Micrograph analyses

A Phenom Pro X Scanning Electron Microscope (SEM) applying an accelerating voltage of 15 kV on the samples sputter-coated with gold, was used to evaluate the fiber quality, the fiber diameter distribution after the electrospinning process by means of a Fibermetric software (Phenom) and the quality of the integration of the nanofibers in the hosting matrix.

The obtained electrospun PVDF-TrFE nanofibrous mat showed randomly oriented, bead-free fibers with average diameter of 420 ± 120 nm (Figure 4-11). The measured thickness of the mat was 100 ± 10 μm its areal weight was 20 g/m^2 .

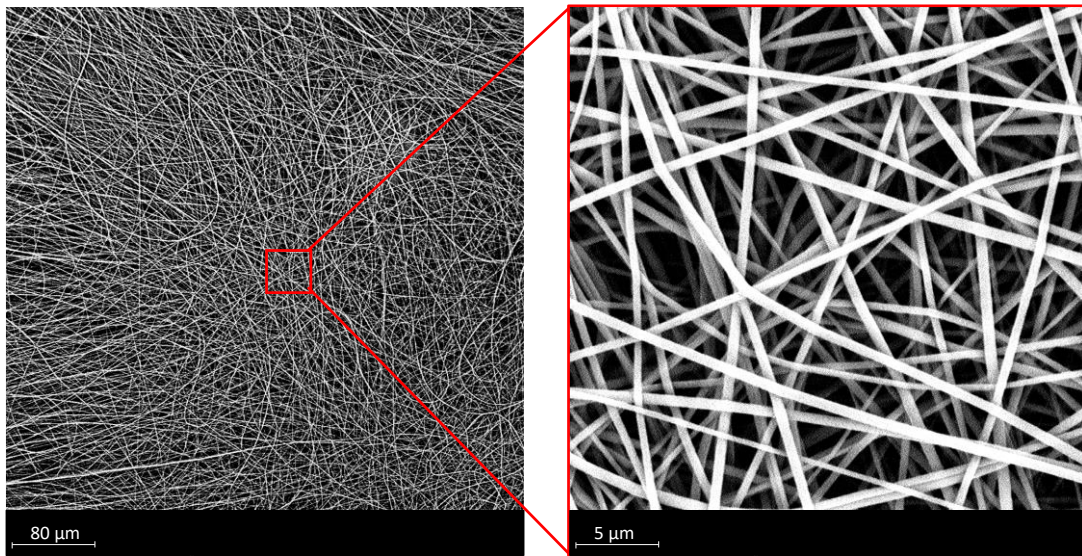


Figure 4-11 SEM image of PVdF-TrFE electrospun nanofibers.

The composite polymeric/nanofibrous layer (epoxy resin + polyurethane matrix/ PVdF-TrFE nanofibers) was observed by means of SEM images of the specimen cross-section, by placing it in vertical position in the specimen stub after a gold-metallization of its cross section. Considering that cutting the piezoelectric layer in ambient temperature would lead to plastic break, a sharp and clearly-observable cross section was obtained by fragile breaking the piezoelectric layer in nitrogen bath. Optimal penetration of the hosting blend inside the nanofibrous layer can be observed in Figure 4-12, thus confirming the excellent compatibility of the polymeric blend and PVdF-TrFE nanofibers, which will avoid delamination when periodic mechanical stresses are applied.

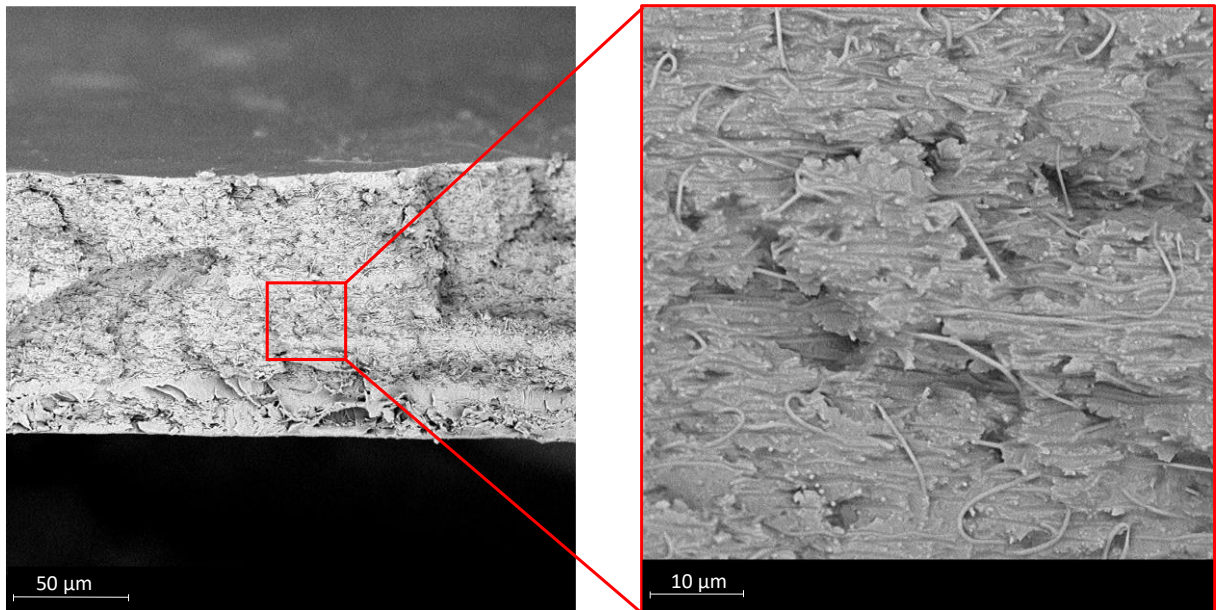


Figure 4-12 SEM cross section view of the nanofibrous layer integrated with the blend of epoxy resin and polyurethane.

With the same procedure, a fragile break of the sensor was performed in order to observe its cross section after the signal electrodes deposition. In Figure 4-13 the central layer is the piezoelectric one, whereas the 100 μm thick layers on the opposite surfaces are the carbon black-based electrodes of the sensor.

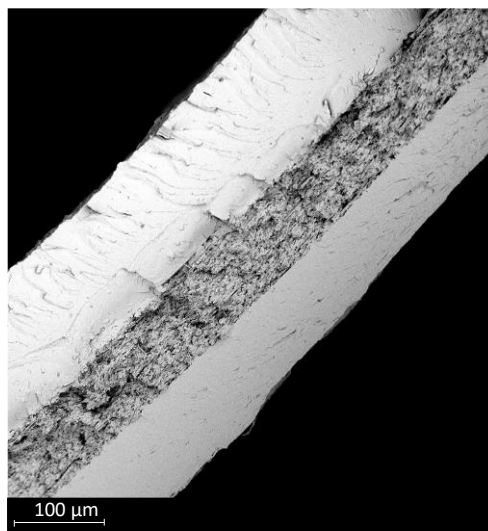


Figure 4-13 Piezoelectric sensor with carbon black based electrodes.

The integration of the piezoelectric sensor with the composite material was observed by means of optical micrograph and SEM analyses of the cross section of the laminate. In Figure 4-14a, the stacking sequence can be observed, with the [CFRP1/GFRP1/sensor/GFRP1] sequence. After polishing, the surface was soaked in an acetone bath for 1 hour in order to dissolve the PVdF-

TrFE nanofibers. In this way, the removed nanofibers can be clearly seen as holes in the SEM cross section magnification of Figure 4-14b. No delamination are observed, confirming the good integration of the sensor between the CFRP laminate plies.

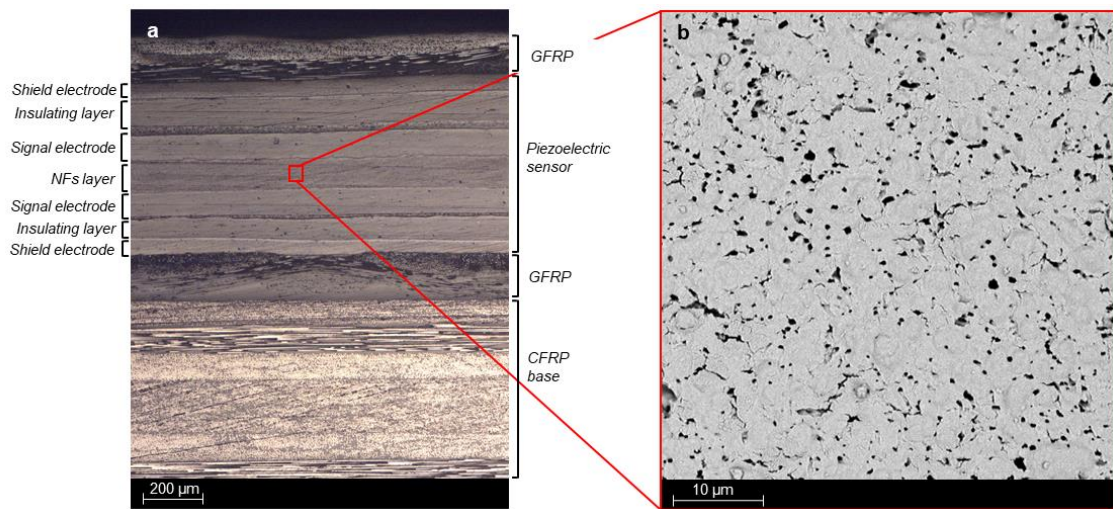


Figure 4-14(a) Micrograph image of the cross section of the composite material; (b) SEM image of the cross section of the nanofibrous layer after etching in acetone bath.

4.1.9 Piezoelectric model

The basic theory behind the piezoelectric phenomenon is based on the electric dipoles. When the material is stressed, the crystal deforms and loses its symmetry and a net dipole moment is created. This dipole moment creates an electric field across the crystal [102]. Piezoelectric sensors are not suitable for static loads measurements because the electrical charge produced decays with time due to the internal impedance of the sensor and the input impedance of the signal conditioning circuits. On the other hand, they are proper for dynamic applications.

The piezoelectric element can be modeled as a charge source or a voltage source, as represented in Figure 4-15, where the generated charge depends on the piezoelectric coefficient and the capacitance of the piezoelectric elements is determined by the area, the width, and the dielectric constant of the material.

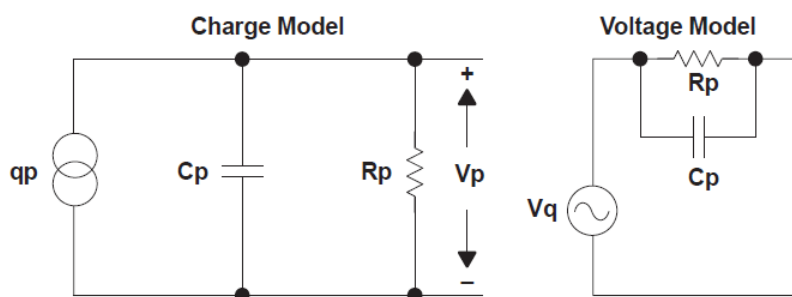


Figure 4-15 Charge model and voltage model of a piezoelectric element.

Considering the manufactured piezoelectric self-sensing laminate, the equivalent electric circuit of the charge model of the laminate connected to a voltage amplifier can be represented in Figure 4-16, where q_p is the charge generator, C_p is the capacitance of the piezoelectric element, R_p is its resistance and C_c is the capacitance associated to the cables of the circuit. The two resistance R_{el} stand for the semi-conductive carbon black electrodes of the sensor and the shunt resistance R_{load} provides a dc bias path for the amplifier input stage [86]. The addition of the capacitor C_{load} in parallel with the resistance R_{load} before the amplifier input is used for the tuning of the RC constant of the circuit.

If an ideal capacitor is charged, a voltage will be stored thanks to its infinite leakage resistance that guarantees a perfect insulation. However, since the internal resistance of the piezoelectric element is not infinite (R_p), the stored charges leak away and the voltage drops exponentially at a rate determined by the time constant τ of the RC circuit, where R is the equivalent resistance of the circuit ($R = 2 * R_{el} + (R_{load} // R_p)$) and C is the equivalent capacitance ($C = C_p + C_c$). The capacitance of the piezoelectric layer C_p is measured to be 55 pF, the capacitance of the cables of the circuit C_c is 5 pF and the resistance of each semi-conductive carbon-based electrodes R_{el} is 4 k Ω .

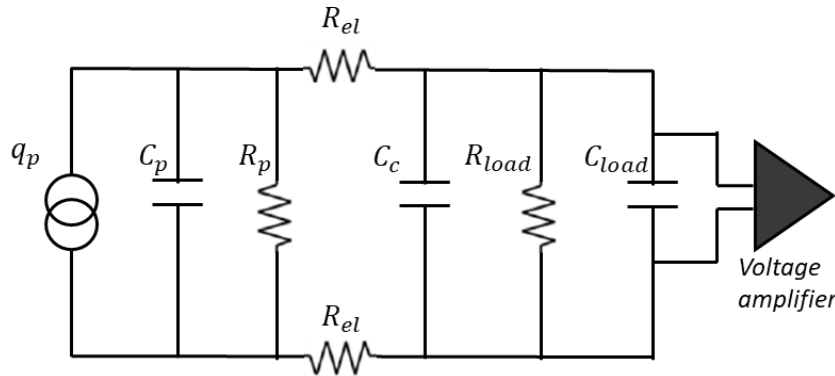


Figure 4-16 Equivalent piezoelectric circuit.

By applying Kirchoff's laws, the output voltage measured across R_{load} can be written as:

$$V(t) = \frac{R}{j\omega RC + 1} d_{33} \frac{dF}{dt} \quad (4.3)$$

where F is the applied force on the piezoelectric element. It can be noted that the output voltage is zero for static loads.

In the case of a sinusoidal load $F(t) = F * \sin(\omega t)$, where $\omega = 2\pi/T$ and T is the period, the equation (4.3) can be solved in the Laplace domain and anti-transformed back in the time domain, as shown in equation (4.4) [44].

$$V(t) = \frac{F\omega R d_{33}}{\omega^2 R^2 C^2 + 1} \left(-e^{-t/RC} + \cos(\omega t) + \omega RC \sin(\omega t) \right) \quad (4.4)$$

Moreover, by modeling the piezoelectric equivalent circuit as the series of a voltage generator with the equivalent capacitance C and resistance R , the resulting behavior of the circuit is equivalent to a high-pass filter. When a voltage signal is sent to the input stage of the electronic filter, the amplitude of the output signal depends on the frequency of the input one. In particular, the filter passes the signals with a frequency higher than a certain *cut-off frequency* f_c and attenuates the low-frequency signals. The cut-off frequency value depends on the circuit parameters (R and C) and it is defined as follow:

$$f_c = \frac{1}{2\pi RC} \quad (4.5)$$

Therefore, if a voltage signal is sent to a high-pass filter, the output voltage can present different shapes depending on the value of the RC constant of the circuit. For instance, considering a square wave input pulse with a fixed period T , the shape of the output pulse will change as function of the RC value of the circuit, as shown in Figure 4-17. When the RC is much larger than the pulse width ($10 T$), the output waveform present a trend similar to the input square waveform. While in case of low RC values ($0.1 T$), the output waveform assumes the shape of narrow and sharp spikes.

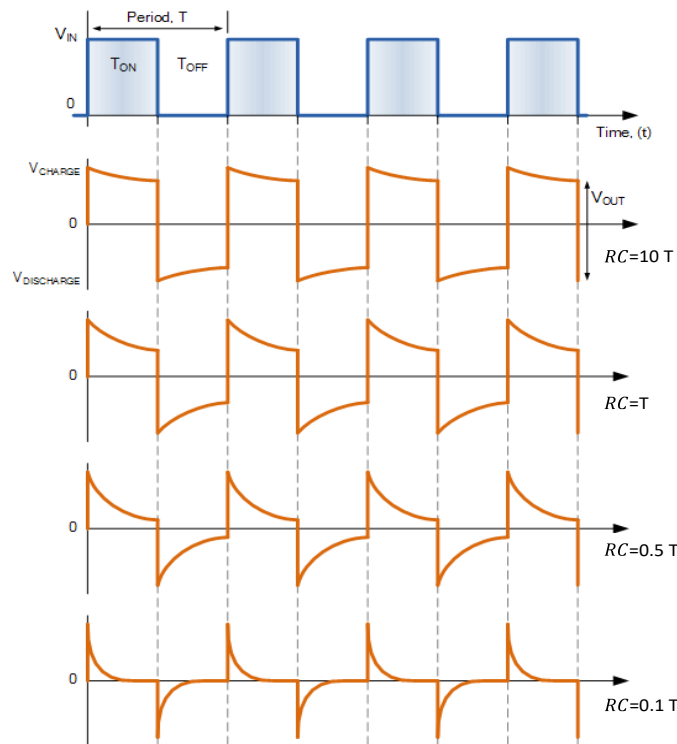


Figure 4-17 Output waveform of the high-pass filter as function of the RC constant.

Similarly with the high-pass filter description, the acquisition circuit parameters of a piezoelectric element can be tuned so that the piezoelectric output signal accurately follows the applied force curve. Indeed, with the aim to produce a piezoelectric self-sensing material that is capable to detect also quasi-static loads (e.g. Gait cycle), a proper tuning of the RC value can be achieved by varying the R_{load} and C_{load} values of the equivalent circuit of Figure 4-16.

4.1.10 Characterization technique

The piezoelectric response of the self-sensing laminate was evaluated in a frequency range between 0.25 Hz and 20 Hz, by means of tensile machine ElectroPuls E1000 (Instron™, Norwood (MA), USA, www.instron.us) equipped with a 2 kN load cell. The self-sensing laminate was compressed between a flat plate and a 1 cm diameter cylindric indenter, as shown in Figure 4-18. The piezoelectric signal was conditioned by an amplifier AD795JRZ mounted on a Single S08 Precision Amplifier Evaluation Board with a high impedance input and the shields electrodes were connected to the ground. The amplifier was set in a buffer mode, so no signal amplifications were performed. The piezoelectric and the load cell signals were synchronously acquired by the tensile machine. The piezoelectric response of the laminate was evaluated for different shunt resistances (R_{load}) and capacitances (C_{load}) connected in parallel to the amplifier input.

The electromechanical tests were carried out for the self-sensing laminate and for the piezoelectric sensor before the integration between the laminate plies, with the aim to investigate variations on the piezoelectric response.

The results of the electromechanical characterization of the produced specimens are reported in section 6.1.1, together with the discussions about the possibility to use such a sensor for quasi-static loads and the optimal acquisition circuit configuration for low-frequency applications.

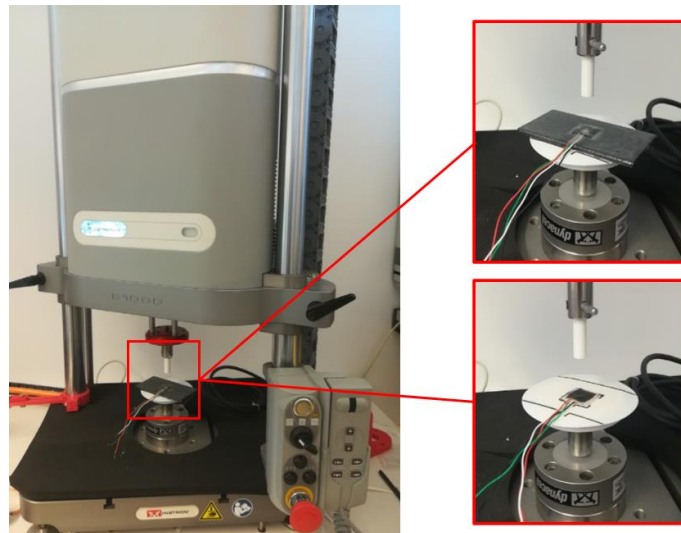


Figure 4-18 Test setup.

4.2 Position flexible piezoelectric sensor based on core-shell nanofibers

4.2.1 Context

Tactile sensors based on electrospun PVdF-TrFE nanofibers have recently attracted widespread attention because of their high sensitivity [103]. The piezoelectric properties and the sensibility of the pressure sensors are greatly enhanced when the PVDF fibers become more oriented [104]. Different alignment methods for the nanofibers were designed. For instance, Edmondson et al. introduced the concepts of the parallel-electrode electrospinning with centrifugal dispersion to produce nanofibers with a high degree of alignment and uniformity [105] and demonstrated the importance of the fibers alignment grade in the voltage generation capability. The effect of different rotating speeds of the disk collector during the electrospinning was studied in terms of alignment grade of the nanofibers and β phase orientation in the polymer chains [106]. Indeed, signals obtained from sensors with 80% of aligned fibers showed amplitudes about 4 times larger than those having only 30% [107]. Higher sensitivity of nanofibrous layers were achieved by inserting nanofillers, such as Ag nanowires, multi-walled carbon nanotubes, etc., because they enhance the content of β phase in the crystalline structure [108]. Moreover, one remarkable improvement of sensitivity was obtained by electrospinning aligned PVDF-TrFE core-shell nanofibers [77]. With respect to PVdF-TrFE nanofibers, four times higher sensitivity values (up to 4000 $\mu\text{V}/\text{mmHg}$) were found by producing an aligned array of nanofibers based on a conductive core (PVP-PEDOT:PSS) and a piezoelectric shell (PVdF-TrFE). Such a sensitive membranes were used for the production of pressure sensors for endovascular applications.

In this section, a peculiar kind of sensor based on piezoelectric nanofibers is described. The working principle of the sensor is the direct piezoelectric effect and its mechanical structure is not based on traditional stiff nanofibers, but on core-shell nanofibers produced via coaxial electrospinning. Indeed, with the coaxial electrospinning technique it is possible to obtain core-shell nanofibers, where the core used in this work is a conductive polymer (PEDOT:PSS) and the shell is the piezoelectric polymer (PVdF-TrFE). The shell is then covered with a metal coating for the realization of the external electrode, thus realizing a coaxial nano-piezoelectric device. As a mechanical stress is applied on the shell of the nanofiber, according to the direct piezoelectric effect, the generated charges distribute on the two opposite surfaces of the shell of the fiber (inner part and outer part). The opposite polarity charges are thus collected by the conductive core and the metallized layer outside the shell, as shown in Figure 4-19.

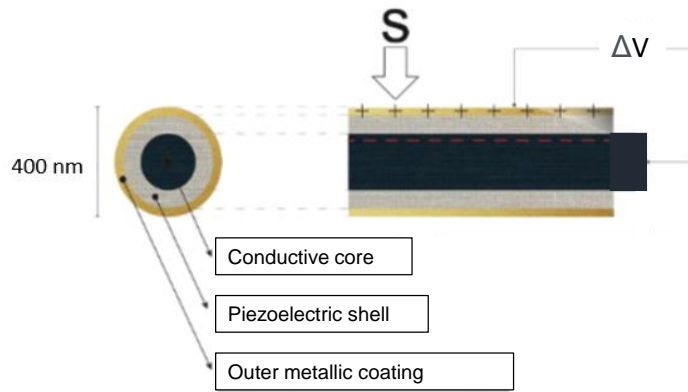


Figure 4-19 Core-shell nanofiber with external metallization.

In this way, every single nanofiber works as a piezoelectric nano-sensor and as a mechanical impact is applied, a piezoelectric voltage is generated as result of the charge flowing in the core electrode and the shell electrode. The output voltage is measured by electrically connecting the core and the shell to macro-scale electrodes that are disposed in the opposite ends of the fibers, thus leaving a free-electrodes surface area. By displacing those coaxial nanofibers in an appropriate arrangement and integrating them in a polymeric matrix, it is possible to realize a multifunctional material that is able to detect the exact position of a mechanical stress applied on its surface, as schematically represented in Figure 4-20. The nanofibers are aligned in a matrix disposition and the macro-scale electrodes are stacked on the edges of the nanofibrous area. The exact position of a mechanical impact on the surface of the sensor is detected by comparing the output voltages of the systems and going back to the position of the correspondent electrodes. Finer resolution of the impact localization can be achieved by increasing the number of the electrodes stacked in the edges of the sensor.

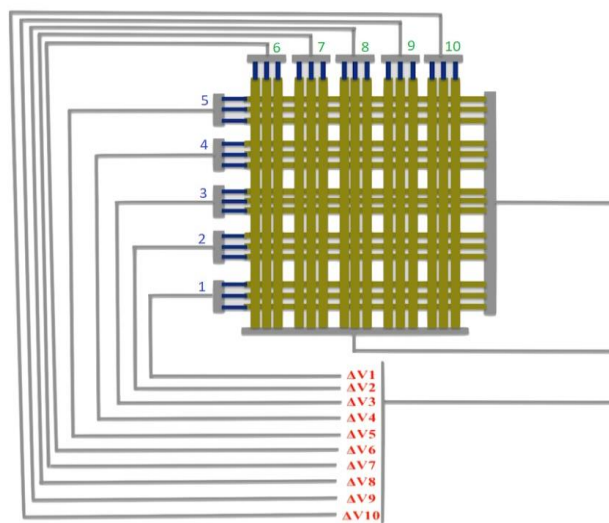


Figure 4-20 Schematic representation of the position piezoelectric sensor.

Strong focus was put on the optimization of the coaxial electrospinning process. Starting from PVdF-TrFE and PEDOT:PSS, different polymeric solutions were investigated in terms of solvents concentrations and viscosity. The aim is to precisely tailor the morphology of the nanofibers by controlling the viscosity values of the solutions and to identify the parameters for the production of smooth and beads-free coaxial nanofibers in a stable electrospinning process. It is important to underline that a stable electrospinning process is intended to be a process where the coaxial drop coming out from the needle (coaxial Taylor cone) is stable over the time under the electric field action and the nanofibers are regularly deposited on the ground collector. But at the same time, a stable process does not mean that the produced nanofibers are high quality nanofibers and their coaxial shape is not always assured.

Once solutions and electrospinning parameters are optimized, the nanofibers are aligned in a matrix disposition and integrated with a polymeric hosting matrix in order to protect them. Carbon black based electrodes are then integrated in the sensor structure in order to guarantee flexibility and material homogeneity.

4.2.2 Polymeric solutions

The interaction between the core and the shell polymeric solutions is a further critical parameter for a high-quality nanofiber production. When the droplet is charged at sufficient high electric field, a coaxial liquid jet is emitted, flowing towards the ground collector. The evaporation rate of the volatile solvents of the liquid solutions depends on different factors (i.e. boiling point, solutions concentrations, distance from the ground collector, etc.) and determines the coaxial morphology of the solid fibers [109]. Successful process depends on the design of the two polymeric solutions such in a way that the electrospinning process and the solidification of the fibers happen in the desired manner.

In this work, different pairs of the core and shell solutions have been studied by varying their solvents concentrations and thus their viscosity, as described next.

For the shell solution, PVdF-TrFE Solvane (75/25%mol, Mw=410 kDa), kindly provided by Solvay Specialty Polymers (Bollate, Italy), was dissolved in methyl ethyl ketone (MEK) and dimethylformamide (DMF) (Sigma Aldrich).

The conductive polymer poly(3,4-ethylenedioxythiophene) doped with poly(styrene sulfonate) anions (PEDOT:PSS) was used as core of the nanofibers and was dissolved in DMF in a range of different concentrations. Polyvinylpyrrolidone (PVP) was used as a carrier polymer and solution viscosity modifier, creating a solution based on PEDOT:PSS and PVP. First, a PEDOT:PSS dissolved in water in a concentration of 3-4%, as provided by Sigma Aldrich, with a viscosity equal to 10-30 mPa*s, was tested. Then, a PEDOT:PSS (PEDOT:PSS, 5% in water, Sigma

Aldrich) with higher conductivity, a viscosity of 30,000-90,000 mPa*s and in a gel physical state was electrospun also without PVP.

A wide number of polymeric solutions was investigated and different combination of core/shell were electrospun. Polymer concentration was varied both for the shell and core solutions, as reported in the follow.

- **Shell solutions (S1-S6) based on PVdF-TrFE (75/25 mol%)**

The polymeric shell solutions were prepared by dissolving the polymer in the solvents. MEK and DMF were used as solvents in 72:28% wt proportion. Each solution was left on a magnetic stirrer at 40°C for 20 minutes and at room temperature for 30 minutes before the electrospinning. Six solutions were prepared by varying the concentration of PVdF-TrFE from 18% wt to 28% wt, as reported in Table 4-6.

Table 4-6 Shell polymeric solutions based on PVdF-TrFE.

(%wt)	PVdF-TrFE	DMF	MEK
S1	18%	23.0%	59.0%
S2	20%	22.5%	57.5%
S3	22%	21.8%	56.2%
S4	24%	21.3%	54.7%
S5	26%	20.7%	53.3%
S6	28%	20.1%	51.9%

- **Core polymeric solutions (C1-C3) based on PEDOT:PSS (3-4% in water)**

The solutions were prepared in three different steps. First, the carrier polymer PVP was dissolved in DMF for 40 minutes at 60°C. The carrier polymer is necessary to obtain an electro-spinnable solution. Second, the solution was stirred for 24 hours at room temperature. In the end, PEDOT:PSS was added and the final solution was stirred for half an hour at room temperature before electrospinning. The three solutions compositions are reported in Table 4-7.

Table 4-7 Core polymeric solutions based on PEDOT:PSS (3-4% in water).

(%wt)	PEDOT:PSS	DMF	PVP
C1	20.2%	76.9%	2.9%
C2	20.2%	75.4%	4.4%
C3	20.2%	73.7%	6.1%

- **Core polymeric solutions (C4-C8) based on PEDOT:PSS (5% in water)**

The gel physic state of this PEDOT:PSS stems from its higher concentration in water and presents the possibility to be electrospun even without a carrier polymer. The core polymeric solution was prepared both with PVP as carrier polymer and without it, as shown in Table 4-8. The PEDOT:PSS concentration was varied between 36%wt and 60 %wt.

Table 4-8 Core polymeric solutions based on PEDOT:PSS (5% in water).

(%wt)	PEDOT:PSS	DMF	PVP
C4	60%	40%	/
C5	50%	50%	/
C6	45%	55%	/
C7	40%	60%	/
C8	44%	50%	6%
C9	42%	53%	5%
C10	36%	60%	4%

4.2.3 Viscosity analyses

The viscosity of the polymeric solutions has a strong effect on the process and consequently on fiber morphology. The viscosity is correlated to the number of entanglements formed by polymer chains in the solution. As previously mentioned, in the case of traditional electrospinning, low viscosity solutions may result in electrospray and beads formation on the fibers, whereas high viscosity solutions can cause problems during the flow through the needle. In the case of coaxial electrospinning, the fluids interaction between the shell and the core determines the morphology of the nanofibers and depends on the viscosity values of each polymeric solution. Low viscosity values of the shell solution can result in a not-complete covering of the core of the fiber, compromising its coaxial shape. Differently, too viscous shell solutions could prevent the constant flow of the core inside the Taylor cone, thus interrupting the continuity of coaxial morphology once the fibers are solidified.

Each viscosity value of the solutions described in section 4.2.2 was determined by means of Anton Paar MRC rheometer. The polymeric solution is placed on a horizontal plate and a rotating cone is placed over it. The angle between the surface of the cone and the horizontal plate is around 1 degree. The cone works at growing rotating speeds and it makes the liquid move. For each rotating speed the correspondent viscosity is measured. In particular, the viscosity value that has been selected for this study is the one corresponding to the speed the polymeric solutions have when they flow out of the needle during the electrospinning process. The speed of the solutions is calculated from the needle diameter and the flow rate of the pump. The shell solutions

viscosities are reported in Figure 4-21 and the core solutions ones are reported separately for the PEDOT:PSS dissolved in water at 3-4% wt and for PEDOT:PSS dissolved in water at 5% in Figure 4-22 and Figure 4-23, respectively.

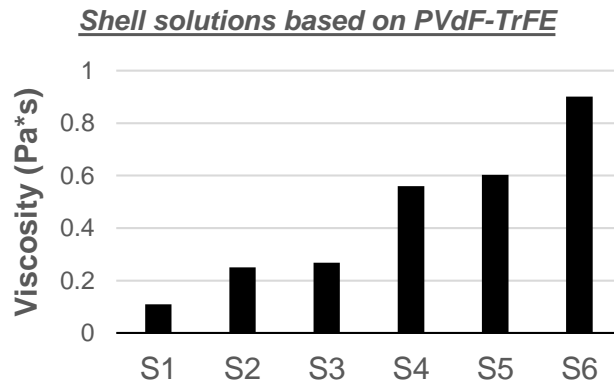


Figure 4-21 Viscosity values of the shell solutions (S1-S6) based on PVdF-TrFE.

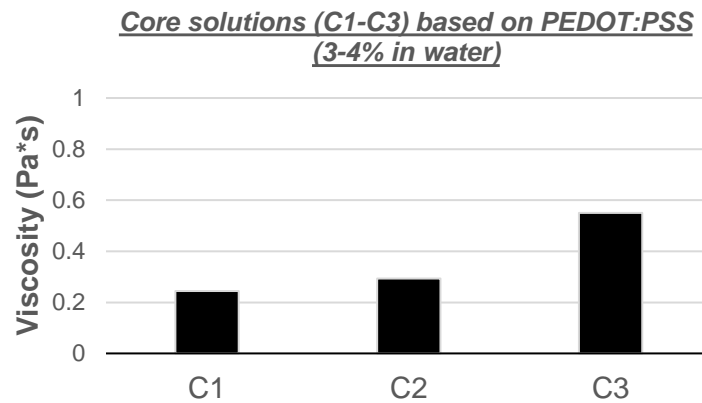


Figure 4-22 Viscosity values of the core solutions based on PEDOT:PSS (3-4% in water).

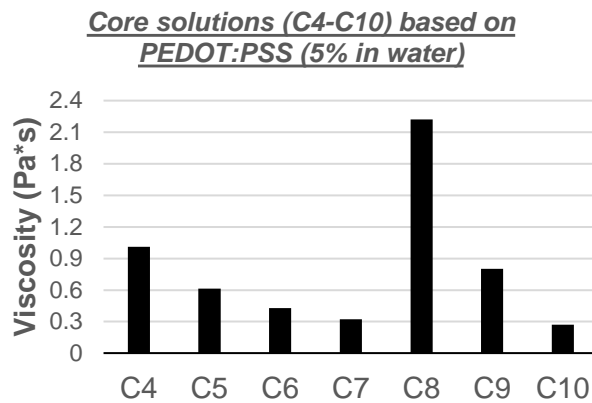


Figure 4-23 Viscosity values of the core solutions (C4-C10) based on PEDOT:PSS (5% in water).

As predictable, the higher the concentration of PVdF-TrFE, the higher the viscosity of the shell solution, which varied from 0.1 Pa*s to 0.9 Pa*s. The presence of the carrier polymer PVP in the core polymeric solutions strongly affects the viscosity values even for low variations (i.e. from 0.27 Pa*s of solution C10 to 2.2 Pa*s of solution C8). However, even if the use of PVP is a simple way to regulate the viscosity of the solutions and favors the electrospinning of PEDOT:PSS, its presence is not beneficial in terms of electrical conductivity of the core of the nanofibers, with repercussions on the piezoelectric response. Consequently, the core polymeric solutions that were prepared without using PVP – whose viscosities are regulated only by varying the PEDOT:PSS concentration – are of great interest both in terms of piezoelectric performances and feasibility of the electrospinning process (C4-C7 solutions). Indeed, even if in the case of traditional electrospinning of PEDOT:PSS the PVP is strongly recommended to induce the formation of nanofibers, in the case of coaxial electrospinning the interaction mechanism between the two coaxial liquids could still ensure the continuity of PEDOT:PSS-based core along the fiber length. Each pair of core/shell polymeric solutions was electrospun as described in section 4.2.4. Subsequently, the micrograph analyses of the obtained nanofibers (illustrated in section 4.2.5) provide an ex post evaluation to identify which are the optimal viscosity values that guarantee a coaxial morphology of the nanofibers.

4.2.4 Coaxial electrospinning

The electrospinning process took place for 15 minutes in order to produce 50 μm thickness nanofibrous mats for each core/shell solutions combination. The randomly oriented nanofibers were collected on a ground plane collector and each sample was analyzed in terms of stability of the electrospinning process and coaxial morphology of the nanofibers. The setup parameters such as needle-collector distance, room temperature and chamber moisture were fixed for all the electrospinning tests. The distance between the needle and the grounded collector was 14 cm, the temperature of the room was 25 °C and the chamber moisture was set at 40%. The high voltage value for each electrospinning process was properly set to achieve a stable configuration of the Taylor cone and avoid liquid leakage from the needle. Considering all the core/shell pairs solutions tested, the voltage range was set from 9 kV up to 16 kV. In general, higher electric field values are required for more viscous solutions as the surface tension of the droplet has a dominant role. The flow rate for the shell solution was equal to 1.1 ml/h, for the core solution was equal to 0.35 ml/h. The coaxial needle of Figure 4-24 has an inner diameter of 0.8 mm and the outer one is equal to 1.2 mm.



Figure 4-24 Coaxial needle.

It should be pointed out that the randomly oriented nanofibrous mats collected on a plane ground collector with the abovementioned protocol were used for a morphological and quality analysis of the nanofibers as function of the viscosity of the polymeric solutions. Once figured out the optimal core/shell combination, the electrospinning process apparatus was set up for the production of aligned nanofibers to be used for the sensor manufacturing, as represented in Figure 4-25. The two ground wires electrodes were parallelly disposed at 7 cm distance from each other to make the nanofibers align perpendicularly to their direction.

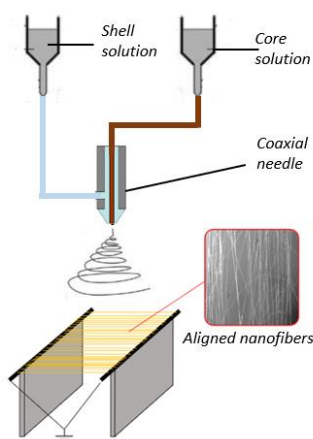


Figure 4-25 Coaxial electrospinning apparatus for aligned nanofibers.

4.2.5 Micrograph analyses

The morphology of each nanofibrous mat was estimated by means of micrograph analyses of SEM and transmission electron microscopy (TEM). The cross-section views of the nanofibrous layers were used to estimate the coaxial shape of the nanofibers in the observed point, whereas SEM images from above the nanofibrous mats provide information about discontinuities along the fibers axis or beads formations. Moreover, TEM images of the core/shell nanofibers estimated the continuity of the core-shell structure along the fiber length.

In the case of SEM cross-section view, the nanofibrous layers were previously cut in a nitrogen bath in order to have a fragile break of the fibers, thus leading to a smooth cross section. Afterward, the mats were soaked for 30 minutes in a distilled water bath in order to dissolve the PEDOT:PSS based core. In this way, the hollow fibers visible in the SEM images represent the previous core/shell nanofibers.

The most representative images for the aim of this work are shown in the following.

- Shell S1 and core C1

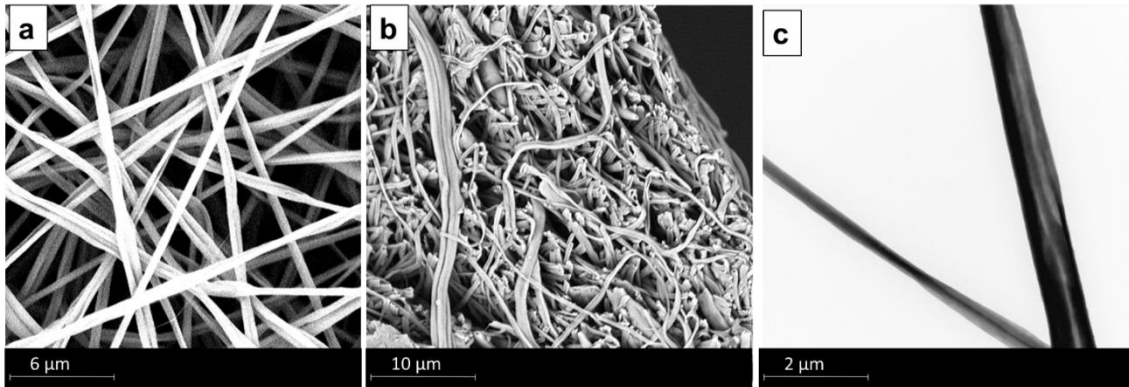


Figure 4-26 Micrographs of core shell nanofibers S1/C1 combination. (a) SEM overview; (b) SEM cross section view; (c) TEM image.

The viscosity of the shell solution S1 was equal to 0.11 Pa*s and the core solution C1 one was equal to 0.25 Pa*s. The SEM image of the nanofibrous layer of Figure 4-26a presents nanofibers with coarse and not regular surfaces. The very low viscosity of the shell polymeric solution resulted in a leakage of the core outside of the shell, thus deforming the nanofibers into split emptied entanglements. The compromised coaxial shape can be observed also in Figure 4-26b, where very few hollow fibers are visible and the fibers cross-section appears flat and crumpled. The TEM image of Figure 4-26c confirms the core leakage outside of the supposed position as the central part of the nanofiber is light grey colored. It is worth highlighting that in TEM images the black portions of the images correspond to conductive material (in this case PEDOT:PSS), whereas the light grey portions of the nanofibers correspond to PVdF-TrFE.

- Shell S2 and core C4

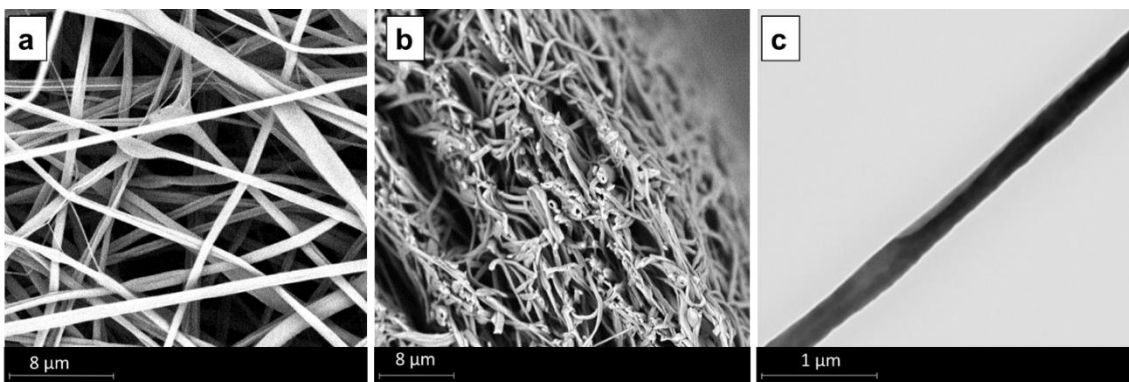


Figure 4-27 Micrographs of core shell nanofibers S2/C4 combination. (a) SEM overview; (b) SEM cross section view; (c) TEM image.

The viscosity of the shell solution S2 was equal to 0.25 Pa*s and the core solution C4 one was equal to 1.01 Pa*s. The coaxial morphology of this combination is not achieved as the core solution presents a very high viscosity value if compared with the shell one. This aspect leads to the formation of enlargements of the fibers (Figure 4-27a) such in a way that the core fills up the totality of the fiber diameter (Figure 4-27c). Moreover, very few hollow fibers are visible in the SEM image of the cross section of the nanofibrous layer of Figure 4-27b.

- **Shell S4 and core C2**

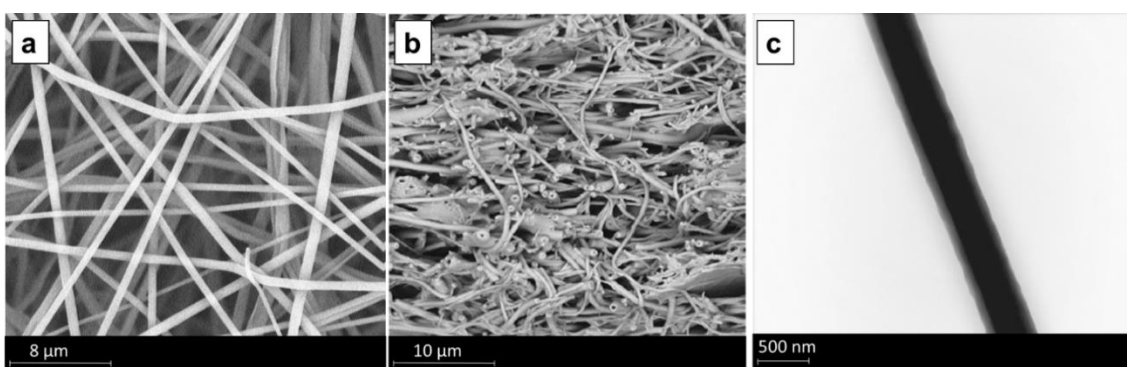


Figure 4-28 Micrographs of core shell nanofibers S4/C2 combination. (a) SEM overview; (b) SEM cross section view; (c) TEM image.

The viscosity of the shell solution S4 was equal to 0.56 Pa*s and the core solution C2 one was equal to 0.29 Pa*s. Smooth and beads-free nanofibers are visible in Figure 4-28a. The core leakage outside of the shell is not visible, as the viscosity of the shell solution S4 is considerably increased with respect to S1 and S2. In this case, the core is well confined inside the shell (Figure 4-28c) and most of the nanofibers present a hollow shape, as observable in Figure 4-28b. The presence of PVP in the core solution reasonably favors the continuity of the core along the fiber length.

- **Shell S4 and core C10**

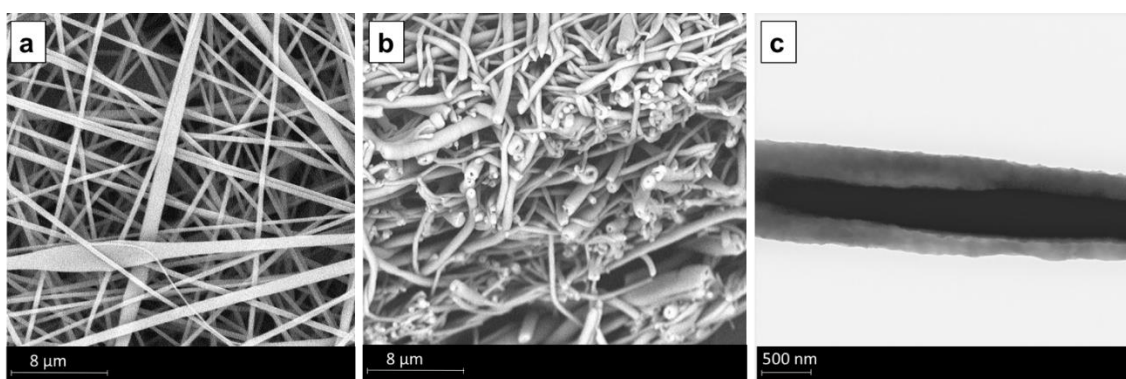


Figure 4-29 Micrographs of core shell nanofibers S4/C10 combination. (a) SEM overview; (b) SEM cross section view; (c) TEM image.

The viscosity of the shell solution S4 was equal to 0.56 Pa*s and the core solution C10 one was equal to 0.27 Pa*s. The viscosity values are very close to the previous combination (S4/C2) and the resulting fibers morphology is also very similar. No split fibers are visible in Figure 4-29a and a large amount of hollow fibers is visible in Figure 4-29b. Moreover, the nanofiber of Figure 4-29c shows a very smooth and defined coaxial morphology.

- **Shell S4 and core C7**

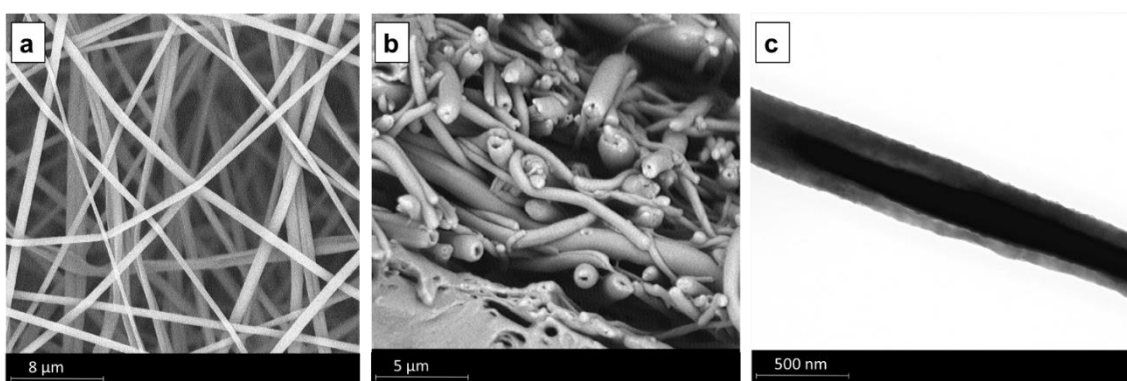


Figure 4-30 Micrographs of core shell nanofibers S4/C7 combination. (a) SEM overview; (b) SEM cross section view; (c) TEM image.

The viscosity of the shell solution S4 was equal to 0.56 Pa*s and the core solution C2 one was equal to 0.3 Pa*s. Also in this case the viscosity values of the polymeric solutions are close to the previous combinations (S4/C2 and S4/C10), but in the C7 polymeric solution the carrier polymer was not used (PVP). Nevertheless, smooth and

high quality nanofibers were still obtained (Figure 4-30a and Figure 4-30b) and the core continuity along the fiber is guaranteed (Figure 4-30c).

To summarize, micrograph analyses showed the importance of the viscosity of the polymeric solutions for the achievement of an optimal coaxial morphology of the nanofibers. Some specific viscosity values for shell and core polymeric solutions can be identified as reference parameters to obtain a good coaxial shape. Indeed, the best nanofibers were obtained by electrospinning polymeric solutions with a viscosity of 0.56 Pa*s and 0.27-0.3 Pa*s for the shell and the core, respectively. If a too low viscous solution is used for the shell, a not-complete covering of the core could occur, losing the coaxial morphology of the fibers. On the other hand, a highly viscous core solution could cause enlargements in the core thickness that would be hardly covered by the shell.

Moreover, by fixing the shell and core viscosity to 0.56 Pa*s and 0.3 Pa*s respectively, it was possible to produce high-quality core-shell nanofiber also without the addition of PVP in the core. This possibility is particularly interesting for the core electrical conductivity, which would be enhanced by means of a free-PVP electrospinning process.

4.2.6 Sensor manufacturing

The investigations performed on the morphology of the core-shell nanofibers as function of the viscosity of the solutions determined the reference parameters for the solutions composition. The core/shell combination used for the sensor manufacturing is C2/S4 (Core solution: 20.2%wt PEDOT:PSS, 75.4%wt DMF, 4.4%wt PVP; shell solution: 24%wt PVdF-TrFE, 21.3%wt DMF, 54.7% MEK). In this section all the steps for the manufacturing process of the position piezoelectric sensor are described.

Nanofibers metallization and disposition

The coaxial electrospinning process has taken place for 30 seconds, in order to produce a very thin layer of coaxial nanofibers aligned perpendicularly to two wires ground electrodes (Figure 4-31a), as schematically reported in the electrospinning setup of Figure 4-25. The electrospinning process was set in order to have a uniform distribution of the nanofibers over the collecting area. The nanofibers were then covered with a gold coating by means of Quorum SC7620 Sputter Coater. The final part of the nanofibers (1 cm length) was not metallized in order to avoid electric contact between the core and the metallization (Figure 4-31b). The piezoelectric nanofibers were then placed over a Teflon support. The same procedure was repeated and the second layer of aligned nanofibers was disposed perpendicularly to the previous one.

Shell electrodes manufacturing

With the aim to guarantee flexibility to the sensor and avoid any mechanical discontinuities, carbon black based electrodes were adopted. The solution composition, the deposition process of the electrodes and the polymeric matrix used as embedding medium (blend of polyurethane and epoxy resin) are the same described in section 4.1.5 and 4.1.6. Before curing, the metallized edge of the nanofibrous mat was deposited on the uncured electrode. A further carbon black based layer was deposited on it to create a sandwich-like structure for the electrical contact with the metallized part of the shell of the nanofibers. The same process was repeated for the other 90° oriented shell electrode, as shown in Figure 4-31c. The curing process was performed at 50°C for 2 hours. Thin signal cables were also added during the curing process.

Nanofibers integration

The body of the piezoelectric sensor was made by integrating the nanofibers in the same embedding medium described in section 4.1.5 (55% wt epoxy resin, 24% wt polyurethane, 21% wt curing agent). The blend was poured on Teflon support and cured for 2 hours at 50°C. The choice of the same polymeric blend both for the carbon black based electrodes and for the embedding medium results in a good adhesion at the interface. Metallic electrodes such as copper wires could cause structural failures in case of bending (Figure 4-31d).

Core electrodes manufacturing

The core electrodes are the ones designated to collect the charges flowing through the core of the nanofibers. They are carbon black based electrodes and their composition is the same used for the shell electrodes. As proof of concept, in this work three core electrodes were designed for each side of the sensor. Before their deposition, each not-metalized side of the sensor was fragile broken in a nitrogen bath in order to have a smooth and clear cross section area (Figure 4-31e). Thus, the whole cross section areas of the core of the nanofibers were exposed and the carbon black based solution was deposited on them to create the electrical contact (Figure 4-31f). The curing process was then carried out for 2 hours at 50°C and signal cables were added.

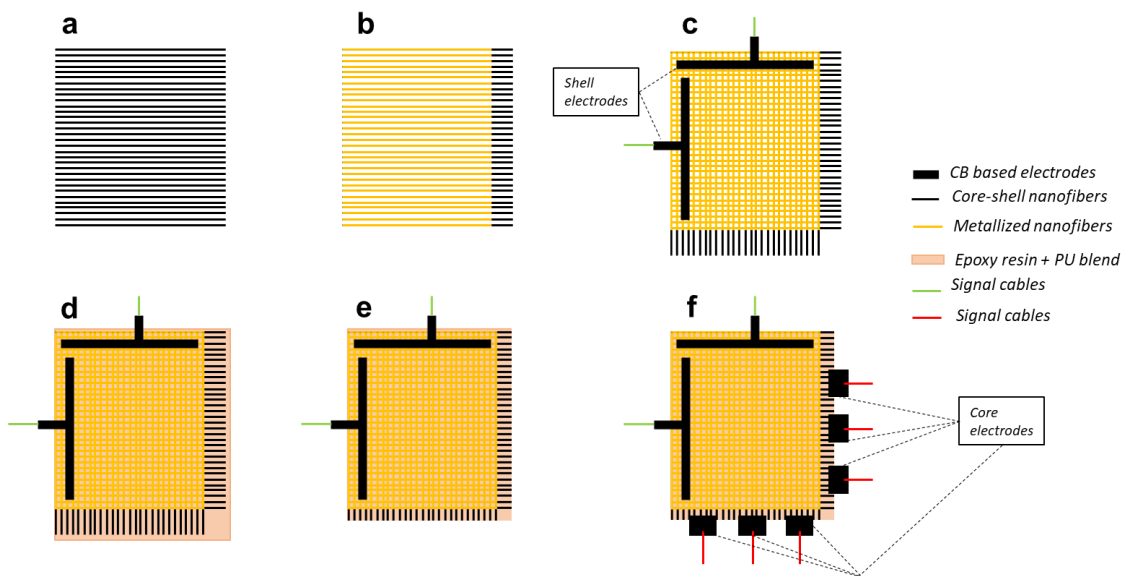


Figure 4-31 (a) Aligned core-shell nanofibers; (b) partial metallization of the nanofibers; (c) CB based electrodes for shell signal; (d) integration in hosting matrix; (e) fragile cut in nitrogen bath for the core exposing; (f) CB based electrodes for core signal.

The manufactured sensor (5 cm x 5 cm) of Figure 4-32 is a 3x3 matrix, where the grid disposition of the core-shell nanofibers generates an output piezoelectric signal higher in the region stressed by a mechanical impact. It is worth noting that the precision of the impact localization can be improved by increasing the number of core electrodes. Ideally by connecting the core of each nanofiber to a micrometric exterior CB-based electrode, the precision the sensor in impact localization could be enhanced up to a micrometric scale.

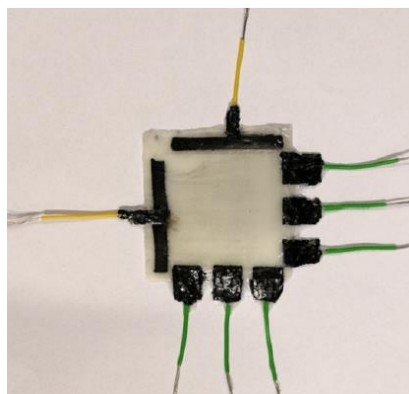


Figure 4-32 Piezoelectric position sensor

4.2.7 Characterization technique

Electromechanical tests were carried out to validate the effective working of the sensor. As shown in Figure 4-33, the nanofibrous piezoelectric sensor was fixed on a support placed over a 300 N capacity load cell (Model 1042, Single point load cells, Tede-Huntleigh). The slider initial position of a linear motor (LinMot, linear motor) was fixed such in a height that the amplitude of the impact force on the piezoelectric sensor was equal to 100 N. The indenter has a diameter equal to 1 cm. The impact position on the surface of the sensor was varied in all the 9 sensitive positions of the 3x3 matrix and the output piezoelectric signals of the shell and core electrodes were simultaneously acquired by means of a digital oscilloscope (Tektronix DPO 5034).

The piezoelectric response of the sensor and the impact localization efficiency are discussed in section 6.1.2.

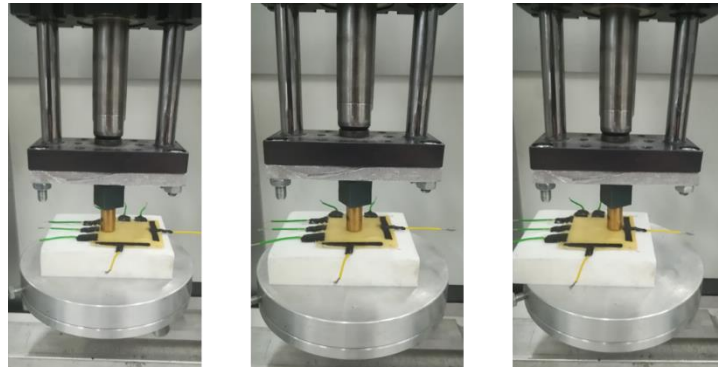


Figure 4-33 Linear motor impacting the sensor in three different sensing positions.

4.3 Self-sensing laminate based on piezo-ceramic nanopowder

4.3.1 Context

Piezoceramic piezoelectric materials such as PZT present higher piezoelectric coefficients if compared with the polymeric ones. They are often used for elastic waves detection thanks to their higher sensitivity. As previously mentioned, Saeedifar et al. designed an eight PZT wafers network attached on a CFRP composite plate surface for accurate damage localization [42]. PZT disks were successfully attached on the CFRP surface for the detection of acoustic waves originated by the debonding of structural components [110]. Higher precision in the damage localization could be achieved by integrating the PZT sensor into the composite laminate, as demonstrated by Yang et al. [111]; but mechanical damages and crack initiation could occur due to the brittle morphology of the PZT [30].

For this reason, efforts have been made to reduce the intrusiveness of the PZT by using different shapes, such as PZT microfibers [112] or powder [113]. The highly fragile nature of the microfibers resulted in dispersion problems in the matrix, whereas PZT powder represented a viable solution for the functionalization of the laminate without affecting its inherent strength.

In this section, a self-sensing composite material was designed and manufactured by dispersing piezoelectric PZT powder inside the epoxy matrix of the laminate. In particular, the PZT powder was interleaved between the GFRP prepreg plies of the laminate together with thin brass sheets electrodes to collect the piezoelectric signal. The effects of the sub-micrometric powder on the mechanical performances of the laminate were compared with the effects of the integration of a commercial PZT disk. Moreover, PZT/GFRP volume ratio were explored in terms of impact resistance of the hosting laminate and sensing performance.

A piezoelectric model was used to correlate the volumetric fractions of the two phases and the polarization process of the laminates with the electromechanical responses to impact.

4.3.2 PZT ceramic powder

The PZT powder was produced starting from the PZT commercial sensor of Figure 4-34a. The sensor was thermally treated at 350°C in order to remove the initial polarization (PZT Curie temperature= 300°C) and to burn the adhesive glue between the PZT disk and the commercial brass electrode. The disk was then grinded using an electrical mill for 20 seconds (IKA A 10 basic). The obtained PZT powder is visible in the SEM images of Figure 4-34b. The PZT particles size presents a bi-modal distribution with one peak at $24.6 \pm 10.9 \mu\text{m}$ and a second peak at $2.06 \pm 0.26 \mu\text{m}$.

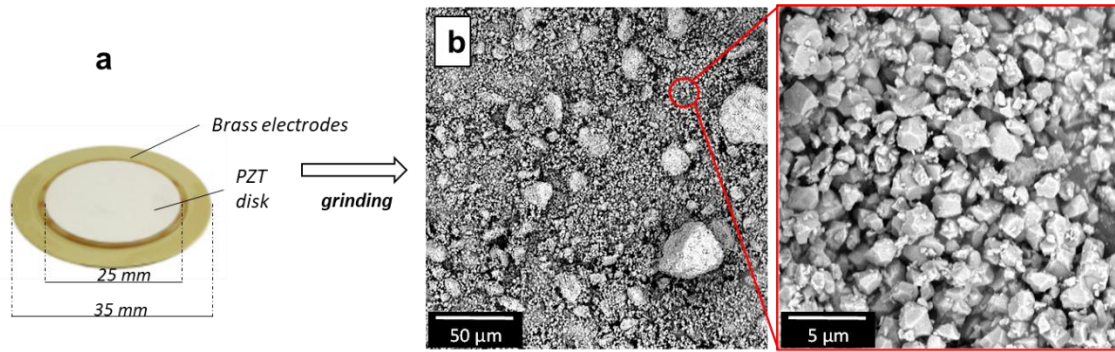


Figure 4-34 (a) PZT commercial disk; (b) SEM images of PZT powder obtained after grinding,

4.3.3 Laminates manufacturing

In order to evaluate the effect of the PZT and GFRP volume fractions, 11 different laminates were manufactured. The number of GFRP plies within the electrodes was varied (2, 4 and 8) in order to change the volume fraction of GFRP. On the other hand, the PZT powder was deposited in the midplane of the laminates with different areal densities (600, 1200 and 2400 g/m²).

In this way, the effects of the different stacking sequences and PZT volume fractions can be investigated in terms of impact resistance and piezoelectric signal response.

The fabrication of the 9 laminates with PZT powder interleaved (PWD laminates) is summarized in the schematic representation of Figure 4-35a. With the aim to compare the PZT powder piezoelectric performances with a commercial sensor, a COM laminate was fabricated by interleaving in the midplane a PZT commercial disk as provided by the manufacturer (Figure 4-35b). Moreover, for the sake of mechanical comparison, a pristine non-sensing laminate was produced by stacking 10 GFRP plies, without any piezoelectric element (REF laminate, Figure 4-35c). The use of 10 GFRP plies was done with the purpose to compensate the thickness of the piezoelectric element and to make all the laminates mechanically comparable.

All the specimens were composed of woven layers of GFRP prepreg (E-glass 8H Satin 300 g/m² - epoxy matrix, VV300S - DT121H-34 DeltaPreg, 50 × 50 × 0.245 mm). The interleaved electrodes are thin circular brass sheets (∅ 20 × 0.1 mm for the upper electrode and ∅ 30 × 0.1 mm for the bottom one), except for the REF laminate (no electrodes are used) and the COM laminate, where the electrodes are the commercial layers bonded to the PZT disk.

The curing process was carried out for 24 hours with a three-steps cycle in order to facilitate the impregnation of PZT within the GFRP plies [86].

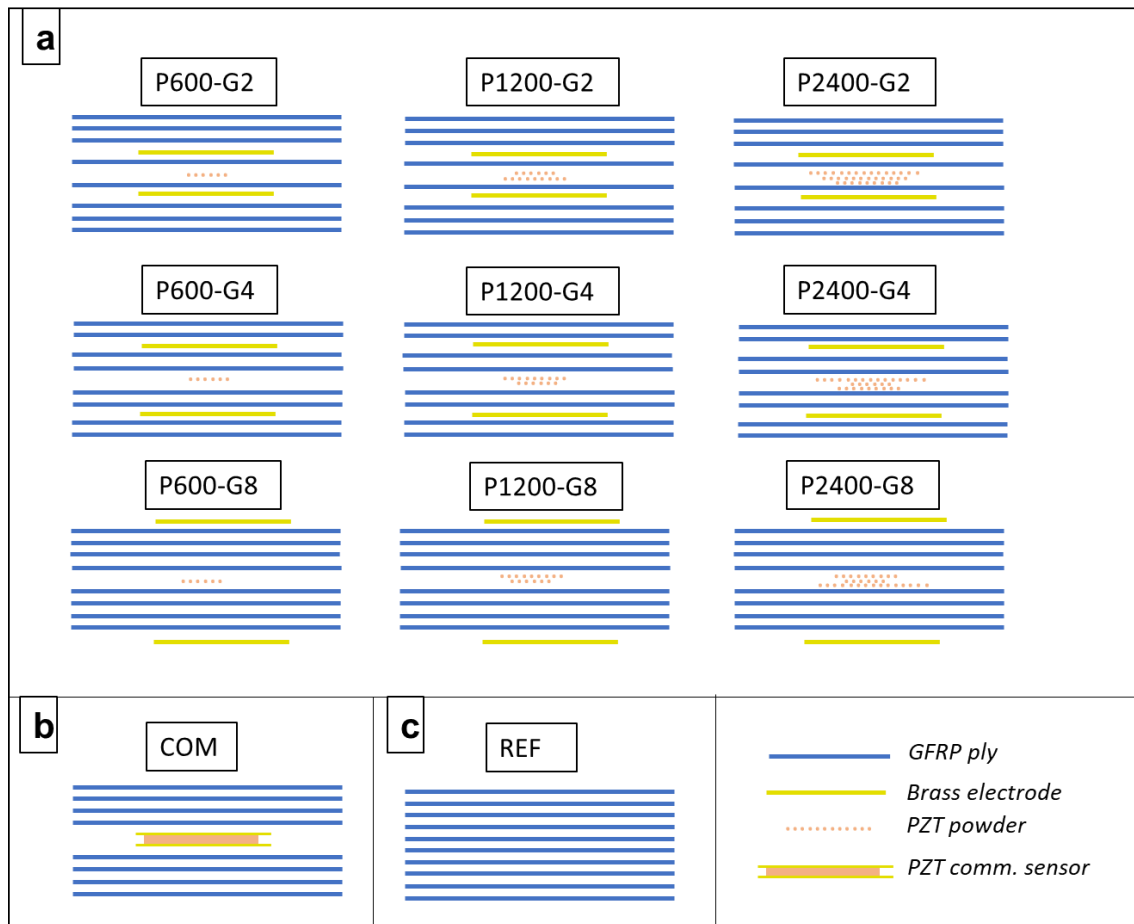


Figure 4-35 Laminates stacking sequences configurations: (a) laminate with different amounts of PZT powder areal weight and GFRP plies between the electrodes, (b) laminate with embedded commercial sensor, (c) reference non-sensing laminate.

4.3.4 Polarization

The polarization process was carried out on every specimen at the same electric field and temperature conditions. First, the process parameters are described in this section, then a polarization model based on the different volume fraction is proposed.

Polarization process

The PZT powder, once integrated in the GFRP laminate, does not present any piezoelectric behavior as the initial polarization was eliminated by the previous thermal treatment. For this reason, a poling process is required to align the ferroelectric domains by applying a strong external electric field [114]. The poling process was then carried out for 24 hours at 100°C by applying 4 kV/mm to the specimens. Even if the Curie temperature of PZT is considerably higher than 100°C, higher temperatures were not feasible for the system, as damages could occur to the polymeric matrix ($T_g=132^\circ\text{C}$). In the end, the system was cooled down to room temperature at 2°C/min keeping the electric field on.

Polarization model

As described in section 4.1.4. the piezoelectric element can be modeled as a multilayered system where the GFRP plies and the PZT layer are connected in series as schematically reported in Figure 4-36, where each phase can be represented as a resistance (R^P , R^G) in parallel with a capacitance (C^P , C^G) [96] (where the superscript P and G refer to the PZT and GFRP phases, respectively).

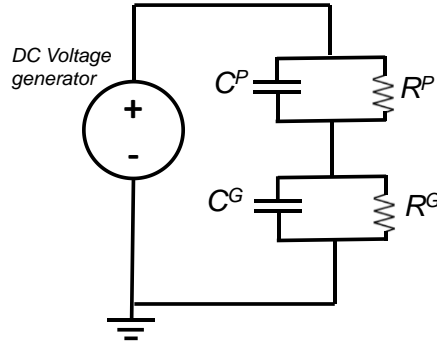


Figure 4-36 Polarization lumped model of the piezoelectric composite, where the PZT (P superscript) and GFRP (G superscript) phases are modeled as a capacitance and a resistor in parallel.

By applying the Kirchhoff's laws to the equivalent circuit, the effective electric field applied on the piezoelectric phase can be calculated as follow:

$$\tau = \tau^G * \tau^P \frac{\frac{1}{\varepsilon^P} + \frac{1 - \nu^P}{\nu^P \varepsilon^G}}{\frac{1}{\sigma^P} + \frac{1 - \nu^P}{\nu^P \sigma^G}} \quad (4.6)$$

$$E_3^P = \frac{\frac{E_3^C}{\sigma^P}}{\frac{\nu^P}{\sigma^P} + \frac{1 - \nu^P}{\sigma^G}} \quad (4.7)$$

where: E_3^C is the electric field applied to the composite laminate (4 kV/mm); E_3^P is the steady state electric field applied on the PZT phase; ε , σ and ν are the dielectric constant, the conductivity and volumetric fraction, respectively; τ is the time constant representing the time the system needs to reach the steady state regime, as previously described. Equations (4.6) and (4.7) are derived by equations (4.1) and (4.2) by using the volumetric fractions instead of the thicknesses of the phases.

The electrical properties of the GFRP and PZT phases (ε and σ) were measured at 100°C and ambient temperature, as reported in section 4.3.6.

Moreover, in order to predict the piezoelectric response of the PZT powder interleaved in the laminates as function of the applied electric field E_3^P , electrical tests were performed on PZT bulky disks. The d_{33}^P of the PZT disks was evaluated for different poling electric field intensities. The commercial disks were treated firstly in muffle to remove the initial polarization, as described

in paragraph 4.3.2. Then, each PZT disk was polarized at 100 °C (composite poling temperature) at different electric field magnitudes for 24 hours, in the range 0.1 ÷ 3 kV/mm. Electric fields higher than 3 kV/mm resulted in electrical breakdown across the ceramic layer. Differently, in the PZT powder-based laminates, it was possible to apply 4 kV/mm as the electric field distributes differently on the GFRP phase and on the PZT phase.

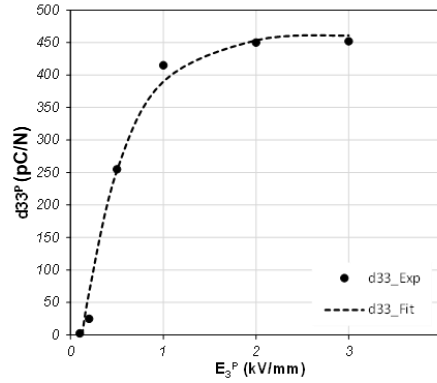


Figure 4-37 PZT piezoelectric strain coefficient d_{33}^P vs poling electric field E_3^P for 24 hours at a temperature of 100 °C.

In Figure 4-37, the experimentally measured d_{33}^P piezoelectric strain coefficients of the commercial PZT disks are reported as black dots for different electric field magnitudes. Those experimental data were then interpolated with the exponential function described in equation (4.8), by using the nonlinear least square method:

$$d_{33}^P = a * \left(1 - e^{bE_{3ss}^P}\right) - c \quad (4.8)$$

where the fitting coefficients a, b and c are equal to 614 pC/N, 2.19 mm/kV and 143 pC/N, respectively. The interpolating equation is represented in the graph by the dotted line and has a coefficient of determination (R^2) equal to 0.985. As it can be observed, the d_{33}^P rapidly increases with the electric field and then stabilizes at a value of 450 pC/N for poling fields > 2 kV/mm.

4.3.5 Piezoelectric model of the laminate

Depending on the amount of GFRP between the piezoelectric element and the electrodes, the flow of the generated charges towards the electrodes is affected. Consequently, the piezoelectric response amplitude of the laminate depends on the volume fractions of both PZT and GFRP. The piezoelectric behavior of the laminates can be described as a simple one-dimensional series connection model of the two phases, as depicted in Figure 4-38.

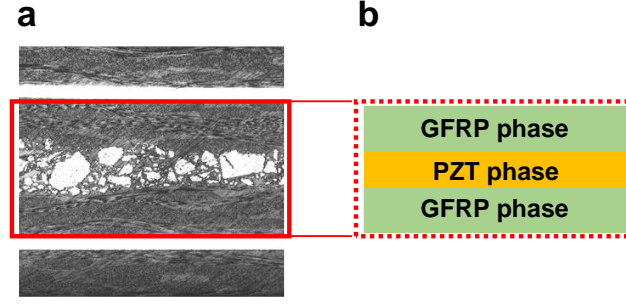


Figure 4-38 Micrograph (a) and equivalent series model (b) of the self-sensing laminate.

Then, according to [115] and [116], in case of a series connection model, the piezoelectric strain (d_{33}^C) and voltage (g_{33}^C) coefficients for the composite laminate can be obtained as follow:

$$d_{33}^C = \frac{\nu^P d_{33}^P \varepsilon^G + \nu^G d_{33}^G \varepsilon^P}{\nu^P \varepsilon^G + \nu^G \varepsilon^P} \quad (4.9)$$

$$g_{33}^C = \nu^P g_{33}^P + \nu^G g_{33}^G \quad (4.10)$$

where d_{33}^P and d_{33}^G are the piezoelectric strain coefficients of the PZT and GFRP phases, while g_{33}^P and g_{33}^G are the piezoelectric voltage coefficients of the PZT and GFRP phases. Equations (4.9) and (4.10) can be simplified considering that the piezoelectric strain and voltage coefficient of the GFRP phases are null.

Moreover, a connection with the polarization model can be established as the piezoelectric strain coefficient of the PZT phase d_{33}^P of equation (4.9) can be calculated by equation (4.8) of the polarization model described in the previous section. In the same way, repeating the procedure on equation (4.10), the piezoelectric voltage coefficient of the composite g_{33}^C can be obtained.

4.3.6 PZT and GFRP phases characterization

The polarization and the piezoelectric model predictions are based on the electrical properties of PZT and GFRP. The electrical conductivity (σ^P for PZT and σ^G for GFRP) and the permittivity (ε^P for PZT and ε^G for GFRP) are measured at 100°C for the polarization model, whereas for the piezoelectric model those values are measured at ambient temperature. Indeed, the polarization process is conducted at 100°C, although the real working of the sensor takes place at ambient temperature.

To measure electrical conductivity, the samples (0.24 mm thick of GFRP and 0.3 mm thick PZT disk) were placed between two electrodes and an electric field of 1 kV/mm was applied. The charging current flowing through the specimens was measured by a pico-amperemeter (Keysight

B2981A) from the electric field switching on moment until the steady-state conduction current was reached. The high voltage electrode presents a 25 mm diameter while the lower electrode consists of a central electrode for the measurement of 15 mm diameter surrounded by a 25 mm guard ring connected to the ground (Figure 4-39a). Each sample was preliminarily sputter-coated with gold replicating electrode area on the sample, as shown in Figure 4-39b.

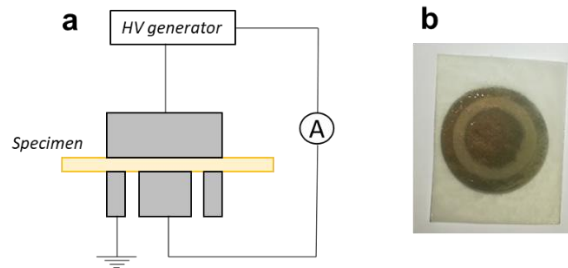


Figure 4-39 (a) Electrical conductivity setup measurement; (b) metallized sample.

The dielectric constants of the single phases were measured by means of the dielectric analyzer (Novocontrol alpha dielectric analyzer B2.2) in the frequency range of $10^{-2} \div 10^4$ Hz.

To summarize, the measured values of both conductivity and permittivity are reported in Table 4-9.

Table 4-9 Electric properties of PZT and GFRP phases, measured at 100°C and 20°C.

	ϵ @ 20°C (F/m 10^{-12})	ϵ @ 100°C (F/m 10^{-12})	σ @ 20°C (S/m 10^{-15})	σ @ 100°C (S/m 10^{-15})
PZT	15937	20364	223	2600
GFRP	58	60	4	143

Comparing PZT and GFRP permittivity values, a difference of three orders of magnitude can be observed for both temperatures. The conductivities difference between the two phases at 20°C is two orders of magnitude, which drops to one order of magnitude at 100°C. This conductivity gap reduction between the two phases at 100 °C is crucial for the polarization process, as will be described in the results section.

4.3.7 Signal conditioning

The acquisition circuit of a piezoelectric element connected to an instrumentation amplifier described in section 4.1.9 can be adapted, in this case, for the self-sensing laminates with PZT powder as schematically represented in Figure 4-40.

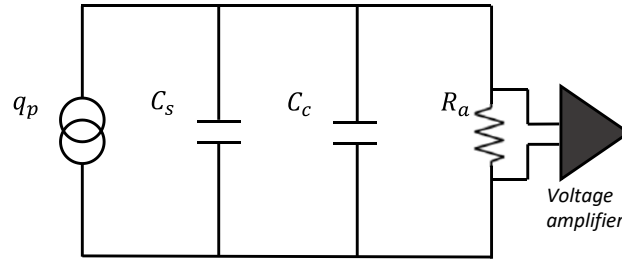


Figure 4-40 Equivalent electric circuit of the piezoelectric laminate.

The self-sensing laminate can be modeled as a charge generator q_p connected in parallel with its resistance and capacitance (R_s and C_s respectively), where R_s is generally high enough to be omitted [44]. The electrical charges generated by the PZT are collected by the two brass electrodes and flow through the cables (C_c) to the amplifier resistance R_a , generating a potential.

The measured cables capacitance was equal to 5 pF while the amplifier resistance is 10 G Ω , according to the INA118 Texas Instrument supplier datasheet. The signal was acquired by a National Instrument NI 9215.

4.3.8 Characterization techniques of the composite

The self-sensing laminates were characterized in terms of electrical properties (impedances and piezoelectric responses) and mechanical resistance. The instrumentations and the methods used for these analyses are reported in this section.

Composite electrical measurements

The capacitances of the sensing laminates were measured in the 40 Hz ÷ 400 kHz range by means of the precision impedance analyzer Agilent 4294A. Knowing the capacitance C , the electrodes surface S and their distance d for each composite laminate, the dielectric constant is derived as follow:

$$\epsilon_3^C = \frac{Cd}{S} \quad (4.11)$$

The piezoelectric responses of the sensing laminates were evaluated with a compressive cyclic load by means of a hydraulic testing machine Instron 8033, equipped with a 25 kN load cell. A compressive force oscillating between 0.5 kN and 1 kN at 25 Hz was applied on the specimen fixed on a support, by means of a 10 mm diameter indenter (Figure 4-41). The frequency value was chosen as result of the cutoff frequency calculation of the system. Indeed, with an equivalent capacitance C (comprising the sensor capacitance C_s and the capacitance of the cables C_c) equal

to 14.2 pF and $R_a=10\text{ G}\Omega$, the cutoff frequency was calculated to be equal to 1.1 Hz. Therefore, 25 Hz is a value sufficiently high to be above the 3 dB cut-off frequency of the RC circuit.

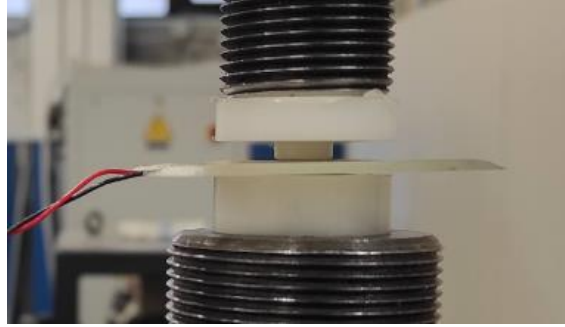


Figure 4-41 Cyclic force indentation setup.

Once the voltage outputs of the laminates were measured, the piezoelectric properties of the laminates can be calculated in terms of piezoelectric strain d_{33}^C (m/V) coefficient and piezoelectric voltage coefficient g_{33}^C (Vm/N). According to [116] and [117], the d_{33} coefficient is generally used to describe the capability of the piezoelectric material to work as an actuator, whereas the g_{33} coefficient is preferred for sensing applications.

Knowing the equivalent circuit parameters of the sensor connected to the amplifier described in Figure 4-40 and the voltage generated by the applied force, it is possible to calculate the piezoelectric strain coefficient of the composite laminate d_{33}^C . For a sinusoidal load, according to [116], the signal magnitude $|V|$ and phase shift φ for a piezoelectric sensor can be expressed as follow:

$$|V| = \frac{d_{33}^C F}{\sqrt{1 + \left(\frac{1}{\omega\tau}\right)^2} C} \quad \tan \varphi = \frac{1}{\omega\tau} \quad (4.12)$$

where $\tau = R_a C$ is the time constant.

For high $\omega\tau$ values, as in this case, equation (4.12) can be simplified as:

$$|V| = \frac{F d_{33}^C}{C} \quad (4.13)$$

and the d_{33}^C value can be simply calculated. Finally, the g_{33}^C coefficient can be calculated as the ratio between the d_{33}^C and the dielectric constant of the composite material ($g_{33}^C = d_{33}^C / \epsilon_3^C$).

This procedure can be replicated for the calculation of the PZT phase piezoelectric coefficients (d_{33}^P and g_{33}^P).

The experimental results are compared with the model predictions in section 6.1.3.

Low velocity impact tests

Low-velocity impact tests were performed to investigate the effect of the interleaving of the piezoelectric element (PZT powder and disk) between the GFRP plies on the mechanical structure of the laminates. The tests were performed on a low velocity impact machine with a 1.3 kg impactor mass equipped with a PCB 208C05 load cell and a 12.7 mm hemispherical steel tip, as described in [118] and shown in Figure 4-42.

The specimens were fixed over a support plate with a 20 mm diameter cylindrical hole, in order to increase the shear stress. The impact energy was equal to 3 J and the impact velocity was equal to 2.2 m/s. Micrograph analyses were performed on the cross-sections of the laminates to evaluate the damages of the structure and to compare the effect of the PZT powder integration with the PZT commercial disk one, as discussed in detail in section 6.1.3.



Figure 4-42 Low velocity impact setup.

5. Design of piezoelectric energy harvesting

5.1 Context

Among the various applications of the piezoelectric materials, energy harvesting devices are attracting great interest in recent years. Thanks to their transducing mechanism, electronic systems for extracting energy from body movements, walking or vibrations have been successfully developed. A wide variety of piezoelectric nanogenerators (PENGs) was investigated, relying on different piezoelectric materials [119], [120]. For instance, zinc oxide (ZnO) piezoelectric properties were deeply studied by manufacturing energy harvesting devices based on ZnO nanowires (NWs) arrays [121], [122]. Moreover, piezoelectric polymers such as PVDF and its copolymers are promising candidates for the development of flexible nanogenerators ([50], [123]), suitable for wearable applications or curvilinear geometries. However, their low piezoelectric strain coefficient d_{33} (~ 25 pC/N) makes them preferable for sensing applications, differently from ceramic piezoelectric materials such as lead zirconate titanate (PZT) which presents d_{33} values of one order of magnitude higher than the PVDF ones [39].

Wearable energy harvesting devices can be placed in strategic points to enhance the mechanical stress on the piezoelectric element. In literature, typical applications can be found for piezoelectric energy harvesters integrated into the shoe. Antaki et al. [124] proposed a stack of cylindrical PZT integrated in a structure that amplifies the force on the piezoelectric element. The high d_{33} value of the PZT led to a peak of 700 mW extracted power. The d_{31} piezoelectric coefficient was exploited to harvest energy from the bending movement of the sole. A stacked configuration of PVDF sheets was observed to generate a peak power of 1.3 mW [125]. Apart from the shoe, others high kinetical energy points of the human movements are the knee, elbow and wrist. By mounting a free-moving mass on a frame, useful electrical power was generated by the impact of this mass on piezoelectric cantilevers positioned at the end of the frame. When mounted on the

human wrist, such a device can theoretically generate up to 40 pW/cm³ [126]. A rotary piezoelectric device designed to be attached to the knee-joint was characterized in terms of harvested energy (in the range between 160-490 μJ) as a function of the angular speed [127]. Feenstra et al. developed a novel energy harvesting backpack that can generate electrical energy from the differential forces between the wearer and the pack [128]. By replacing the strap buckle with a stacked piezoelectric actuator, a mean power of 0.4 mW was obtained from the system.

In addition to improving power harvesting efficiency and energy generation capabilities, recent researches have focused on modifying the power harvesting circuit by adding devices such as capacitors and supercapacitors for energy storage. Indeed, despite these advancements, the working of the described energy harvesters is highly dependent on when and where they are available, making the energy storage devices essential for a stable power supply. Most of the circuits are based on a bridge rectifier that converts the alternate current from the energy harvester into direct current for charging batteries or capacitors [129]. For instance, Hu et al. coupled a piezoelectric nanogenerator based on ZnO nanowires (NWs) with a capacitor for the power-supply of a radio-frequency transmitter [130]. Yuan et al. also fabricated a paper-based flexible supercapacitor charged by a piezoelectric nanogenerator up to 2.6 V in 11 h [131], lighting a LED for about 5 min.

In this work, the experimental campaign for the development of energy harvesting techniques based on piezoelectric materials was developed on two main parallel tracks. First, the power transfer circuit from a piezoelectric generator to an external load was investigated; then the coupling circuit of a piezoelectric material with an energy storage element (capacitor) was optimized.

Moreover, with the aim to integrate the piezoelectric element in a hosting composite laminate (such as the prosthesis sole in MyLeg project), the piezoelectric response of PZT nanofibers was optimized for energy harvesting purposes. Indeed, considering the higher d_{33} coefficient of the ceramic PZT disks compared with polymeric (PVdF-TrFE) films, PZT nanofibers represent a promising solution for energy harvesting applications.

5.2 Power transfer

In this section, the possible extractable power was evaluated for ceramic and polymeric piezoelectric materials. In particular, every piezoelectric sample has been investigated in terms of power transferred to a variable resistive load connected to the circuit.

5.2.1 Piezoelectric materials

The piezoelectric materials used in this section are a PZT commercial disk (0,4 mm thickness and 6 mm of diameter) and a nanofibrous layer of PVdF-TrFE polarized and embedded in PDMS matrix, according to the procedures described in section 4.1.4 and 4.1.5, as shown in Figure 5-1.

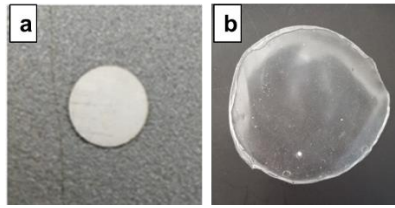


Figure 5-1 (a) PZT disk and (b) PVdF-TrFE nanofibers integrated in PDMS matrix.

5.2.2 Acquisition circuit

The piezoelectric strain coefficient d_{33} of each piezoelectric material is calculated by means of d_{33} -meter (d_{33} PiezoMeter System, Piezotest, Singapore, www.piezotest.com).

In order to reach the maximum power transfer condition, the impedance of the acquiring system has to be tuned with the impedance of the piezoelectric generator. With this aim, the piezoelectric response of the samples has been evaluated over a wide range of load resistances R_{load} , according to the equivalent electric circuit of Figure 5-2, where q_p is the piezoelectric charge generator, C_p and R_p are the capacitance and the resistance of the piezoelectric device respectively, C_c is the capacitance associated to the cables of the circuit and R_{load} was varied. The voltage measurement was performed by the electrometer (Keithley 6517B, input impedance $> 200 \text{ T}\Omega$).

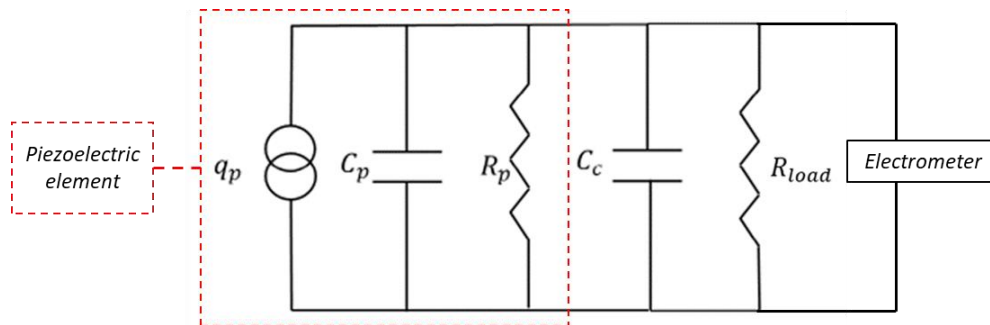


Figure 5-2 Equivalent circuit for power transfer from a piezoelectric element.

5.2.3 Characterization techniques

The power transfer capability of the piezoelectric specimens was evaluated over a frequency range from 2 to 100 Hz. The piezoelectric samples were fixed on a support using conductive tape as electrodes and their surface was stressed by a shaker with a 20 N magnitude force, measured by a load cell, as shown in Figure 5-3a. The measurements acquired by the electrometer were displayed on a digital oscilloscope (Figure 5-3b). Higher applied forces (up to 90 N) were applied on the PZT disk by means of the linear motor described in Figure 4-33 in order to achieve higher values of power transfer.

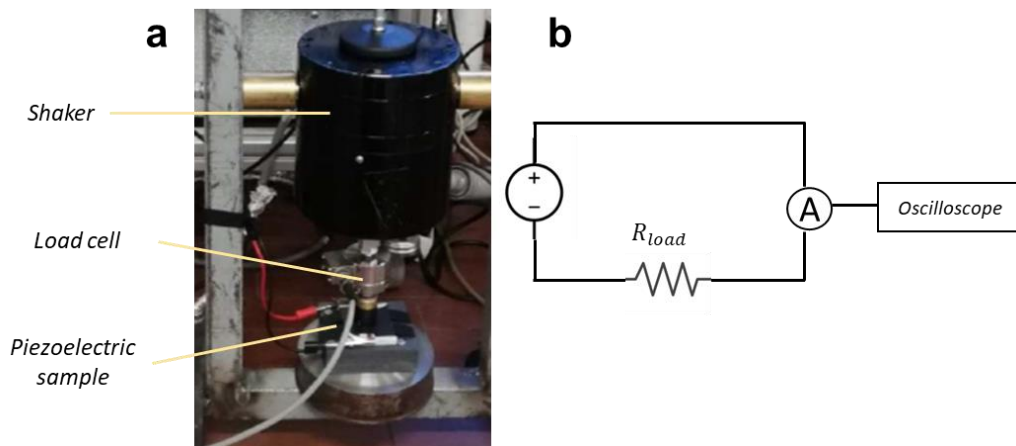


Figure 5-3 (a) Test setup with the shaker; (b) electrical circuit for the acquisition of the piezoelectric output.

5.3 Energy storage

In the case the energy collected by the piezoelectric circuit should be stored, a capacitor can be added to the system. Considered the higher d_{33} value of the PZT if compared with the PVdF-TrFE, in this section the experimental tests were carried out by using the ceramic disk. Two main investigations were conducted on the possibility to charge an energy storing unit. Preliminary tests were focused on the charging of a capacitor (section 5.3.1); then a deep investigation on the coupling system of a piezoelectric stack configuration with a supercapacitor was carried out (section 5.3.2).

5.3.1 Capacitor charging

A single PZT disk was firstly tested under the effect of mechanical stress typical of wearable applications. Then, Gait cycle typical loads (up to 700 N) were applied on a parallel connection of multiple PZT disks integrated in the sole of a shoe.

Capacitor charge

The energy E stored in a capacitor can be expressed as follow:

$$E = \frac{1}{2} C * V^2 \quad (5.1)$$

where C is the capacitance and V is the voltage of the capacitor.

In this work, a 100 nF capacitor was used and the PZT disk was mechanically stressed by the linear motor of Figure 4-33, with 30 N, 60 N and 90 N sinusoidal loads at 2 Hz frequency (wearable applications typical frequency) for 50 s. A bridge rectifier was connected before the capacitor in order to rectify the negative part of the waveform and the piezoelectric output is measured by the electrometer. An oscilloscope was also connected for a real time monitoring of the waveforms. The circuit configuration is schematically represented in Figure 5-4.

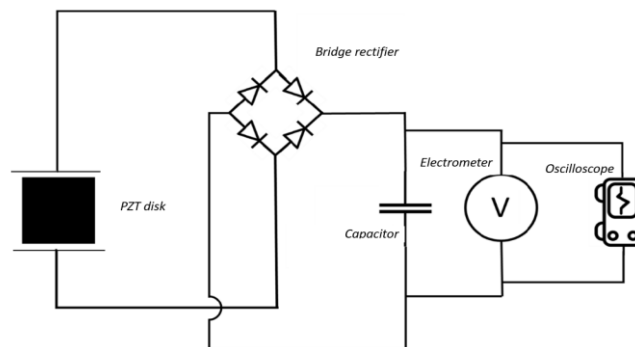


Figure 5-4 Electric circuit for capacitor charging.

Sole test

In order to simulate a close-to-reality condition, four PZT disks were fixed in the heel of the sole of a shoe during a 5 minute walk of a 70 kg person.

With the purpose to increase the available energy, the four PZT disks were disposed in parallel as shown in Figure 5-5 and the energy produced was stored in a 47 μF electrolytic capacitor, connected with the same electric circuit of Figure 5-4, without the electrometer and the oscilloscope.

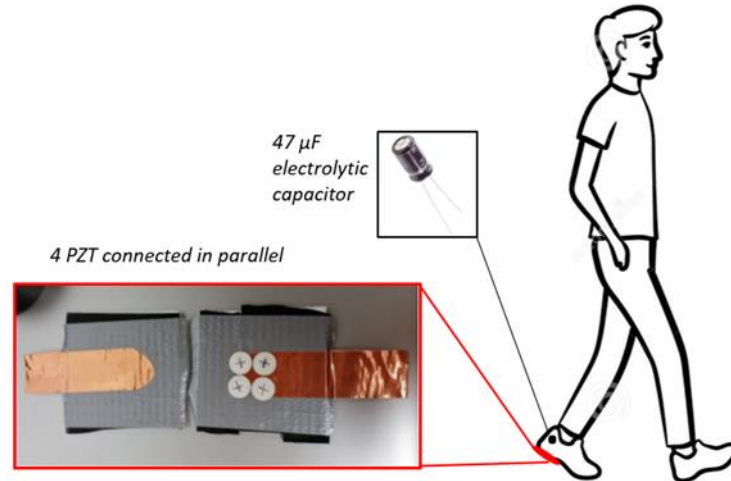


Figure 5-5 Test on the sole.

5.3.2 Piezoelectric-supercapacitor coupling

A stack system of PZT disks was used as energy harvesting source to charge a supercapacitor made of a glass fiber-based commercial separator and organic electrolyte. Aluminum foils with activated carbon YP-80F and superC45 additive were used to realize water processable electrodes by means of a pullulan-glycerol binder. Electromechanical tests were performed in order to estimate the charging time and the harvestable energy from the piezoelectric transducers. The piezoelectric-supercapacitor coupling circuit comprises a full-wave diode bridge rectifier.

The supercapacitor was developed and manufactured at the Department of Chemistry “Giacomo Ciamician” of the University of Bologna.

Single PZT disk characterization

The piezoelectric strain coefficient d_{33} of the PZT disk was evaluated using the Piezometer, by stressing the samples with a compressive sinusoidal force of 10 N at 100 Hz frequency. Furthermore, the measurements of capacitance, permittivity and resistance have been performed by means of the Novocontrol Alpha Dielectric Analyzer v2.2. It is based on a voltage amplifier

for the application of variable frequency electric fields and a measuring cell comprising the high voltage and ground electrodes. Measurements of the capacitance (C_p), $\tan(\delta)$ and permittivity ϵ of the PZT disk have been carried out by applying an oscillating electric field in the frequency range 10^{-1} and 10^4 Hz.

The properties of the PZT ceramic disk are summarized in Table 5-1.

Table 5-1 PZT disk properties.

	C_p (nF)	$\tan \delta$	d_{33} (pC/N)	ϵ_r	g_{33}
PZT disk	21.1	0.0352	200	1445	0.0156

Energy harvesting unit

After having characterized the single piezoelectric disk, multiple PZT disks have been stacked in a proper way to build the piezoelectric energy harvesting unit. This solution consists in physically stacking the piezoelectric disks one on top of the other, building a mechanical anti-series. Each PZT disk side faces the adjacent PZT disk one, while each brass electrode faces the adjacent brass electrode. So, it has been possible to have one single electrode made of copper adhesive tape connecting the same side, brass or PZT, of two different piezoelectric transducers. As a consequence, this configuration permits to have $N+1$ outgoing electrodes for N piezoelectric elements, thus significantly reducing the system dimensions.

Following the explained building strategy, 15 piezoelectric disks were stacked together to have a considerable electrical output which can be used for the supercapacitor charging, as shown in Figure 5-6. The whole piezoelectric energy harvesting generator has been placed over a stiff insulating layer to preserve its consistency. Every electrode coming from the same piezoelectric transducer's side ends with a wire, while the electrodes of the same type are kept together to get the electrical parallel output.

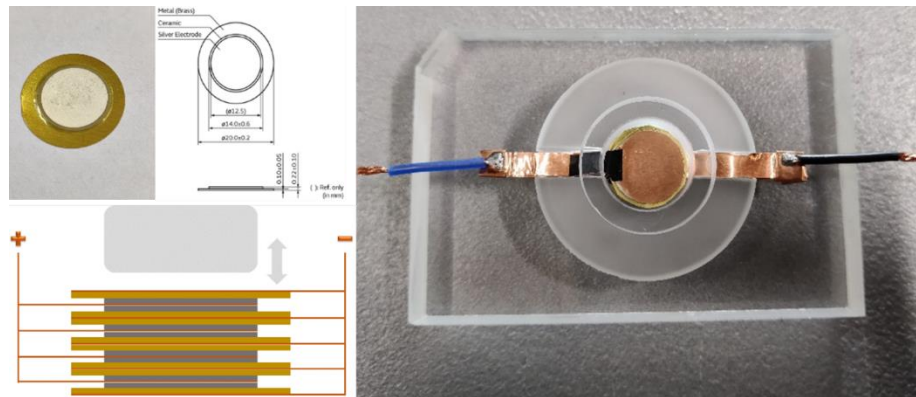


Figure 5-6 Piezoelectric energy harvesting unit.

Piezo-supercapacitor coupling system

The electrical circuit used to couple the piezoelectric energy harvester with the supercapacitor consists of a full wave diode bridge rectifier. It is a well-known solution that has the advantage of being composed of only passive components and for this reason many researchers have chosen this coupling circuit. The main losses of this configuration are inherent to the nature of the diodes' working principle. The full wave diode bridge rectifier consists of four SD-103-A. They are small signal Schottky diodes (Vishay) which can work with a peak inverse voltage smaller than 40 V and present a low forward voltage drop which is about 370 mV for a 20 mA current. The piezoelectric generator is mechanically stimulated by a sinusoidal force and gives an alternating electrical output which passes through the full wave diode bridge rectifier and, once it has been rectified, goes to the Single Pole Double Throw (SPDT) relay. The SPDT relay has been introduced inside the circuit to easily swap from the supercapacitor's charging circuit to the discharging one, as schematically represented in Figure 5-7.

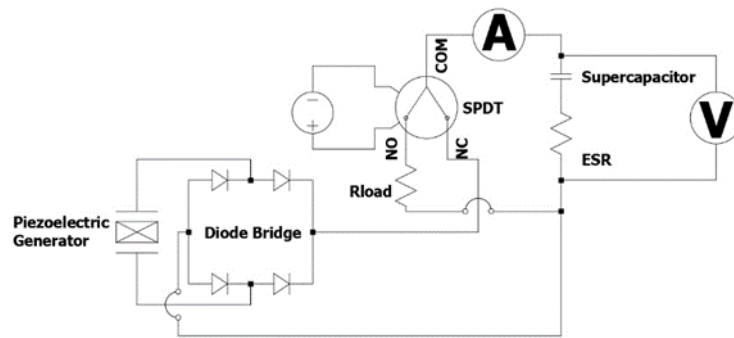


Figure 5-7 Scheme of the electrical circuit used to couple the piezoelectric generator with the supercapacitor.

For the charging stage, the current leaves the diode bridge rectifier and flows through the SPDT relay because NC and COM are connected, is measured in the ammeter and then charges the supercapacitor, while a voltmeter measures the voltage across the supercapacitor. During the discharge process, the current coming out from the diode bridge gets blocked and cannot reach the supercapacitor anymore. Indeed, the relay now connects NO and COM, creating a circuit where the supercapacitor discharges on a fixed-value resistive load (R_{load}) and the current and voltage data are acquired both during the charge and the discharge processes. The discharge tests were carried out on a resistive load of 10 k Ω . This resistance value was chosen in order to clearly see the initial ohmic drop caused by the equivalent series resistance (ESR) of the supercapacitor and to increase the RC time constant of the circuit such in a way to properly appreciate the voltage and current trends over the time.

5.4 PZT nanofibers

The manufacturing process of the nanofibrous ceramic PZT mats was carried out in the Department of Chemistry “Giacomo Ciamician” of the University of Bologna. In this section, the production process of the PZT nanofibers and their polarization process are described.

5.4.1 PZT nanofibers production

The first step consists of the realization of precursors polymeric solutions suitable for the electrospinning process. The precursor solutions were based on lead (II) acetate trihydrate, zirconium (IV) n-propoxide, titanium (IV) isopropoxide, glacial acetic acid and 2-methoxyethanol. To achieve the right rheological properties, a carrier polymer (PVAc) was added to the precursors solution in order to obtain a stable electrospinning process. The obtained pristine nanofibers were heat pre-treated in the oven and later calcined at 700°C in air. During the calcination process in air the organic polymer completely degraded and PZT crystal nucleation and grain densification occurred, thus leading to PZT nanofibers.

The most relevant problem of PZT nanofibers regards their extreme brittleness. Indeed, even a very low pressure leads to mechanical degradation of the nanofibrous mats, preventing any possible piezoelectric characterization. Consequently, a mechanical stabilization procedure was conceived by pouring small drops of Nylon-66-based polymeric solution on the nanofibers. As the solvents evaporated, the nanofibers were coated by the Nylon-66 and the nanofibrous layer tremendously enhanced its mechanical stability. In this way, bending and compressive deformations limitedly impact the morphology of the layer. Besides its toughness and flexibility, Nylon-66 was adopted as a coating polymer considering also its high melting point (>250°C), which prevents thermal degradations during the polarization process (100-130°C). A PZT nanofibrous mat can be observed in Figure 5-8a and the SEM images of Figure 5-8b shows the fibers morphology and the Nylon-66 coating. Differently from the polymeric nanofibers of PVdF-TrFE, some breakages along the fibers are observable, but the Nylon-66 coating maintains the structure integrity at the macroscopic level.

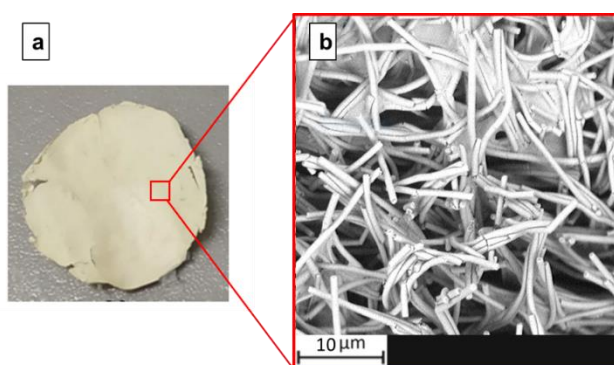


Figure 5-8 (a) PZT nanofibrous mat; (b) SEM images of PZT nanofibers with Nylon-66 coating.

5.4.2 PZT nanofibers polarization

As previously mentioned, the piezoelectric behavior of a PZT sample can be enhanced by applying a strong external electric field in order to align the ferroelectric domains of the material in the electric field direction. The process is carried out at high temperatures with the aim to facilitate dipole mobility. The Curie temperature of PZT is 300°C, but such a high temperature is not affordable for the setup instruments. Nevertheless, literature reports poling processes of PZT nanofibers even for values lower than T_c , so the temperature used in this work was set at 130°C and the poling setup was the same of Figure 4-3, used in case of PVdF-TrFE.

As previously described in detail (section 4.1.4), the polarization process of a nanofibrous layer can be modeled as a multilayered system where the electric field distribution depends on the electrical properties of the components of the system. Consequently, the polarization of a nanofibrous layer strongly depends on the embedding medium where the process is carried out. According to equation (2), the higher the conductivity of the embedding medium σ_{em} , the higher the electric field applied on the nanofibers E_{nf} . At the same time, the conductivity σ_{em} cannot be too high in order to avoid electrical breakdowns across the sample during the process.

The experimental campaign aimed to identify the proper embedding medium to be used in the poling process that maximizes the piezoelectric behavior of the PZT membranes. The same embedding medium materials described in section 4.1.4 (silicon oil, seeds oil, ester oil and blend of polyurethane and epoxy resin) were tested and the d_{33} values were measured for each specimen by means of a Piezometer (Figure 5-9). The polarizing electric field value and the conductivity values of the embedding mediums are the same as Table 4-2, whereas the duration time of the process was equal to 30 minutes.

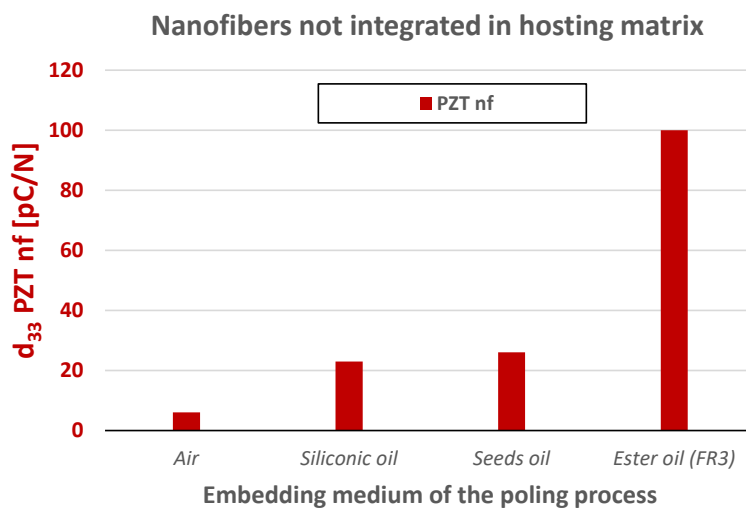


Figure 5-9 d_{33} values of PZT layers polarized in different embedding mediums.

Similarly to what was reported for PVdF-TrFE specimens, the highest piezoelectric coefficient is registered for a polarization process carried out in ester oil, which is the most electrical conductive medium used in this experimental test. Moreover, 100 pC/N is a d_{33} value comparable with commercial PZT disk (300-350 pC/N).

Afterwards, as previously described in section 4.1.5 for PVdF-TrFE, the PZT nanofibers were integrated with a polymeric soft matrix made of a blend of epoxy resin (Itapox 108, kindly provided by Ddchem S.l.r., Verona, Italy) and blocked isocyanate polyurethane prepolymer (Synthane 2095, Synthesia Technology, Barcelona, Spain). The d_{33} values of such composite piezoelectric layers were measured and compared with a further piezoelectric layer in which the poling process was performed after the integration in the soft matrix, as reported in Figure 5-10. In this way the soft polymeric matrix was considered as an embedding medium of the poling process.

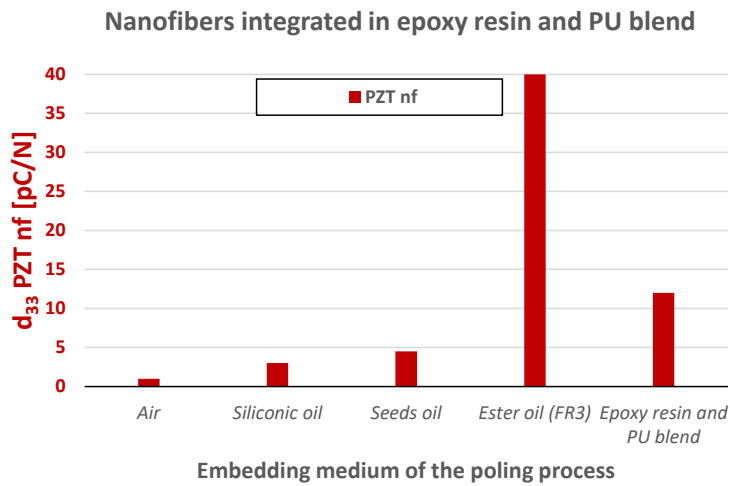


Figure 5-10 d_{33} values of PZT layers polarized in different embedding mediums and integrated in a soft hosting matrix.

The overall decreasing of the d_{33} values can be attributed to the stiffness of the polymeric hosting matrix which reduces the load transferred to the nanofibers. However, the polarization process in ester oil results in a d_{33} value of 40 pC/N, whereas the polarization performed after the integration of the nanofibers in the hosting matrix resulted in a lower d_{33} value (12 pC/N).

5.4.3 Characterization technique

According to the setup previously described in section 5.2.3 and the equivalent circuit of Figure 5-2, a sinusoidal compressive force was applied on the PZT nanofibrous layer at a frequency of 2 Hz. The R_{load} value was varied in order to identify the maximum power point transfer and the energy harvesting capability of the piezo-ceramic layer. The energy harvesting capability are discussed in section 6.2 in terms of both power transfer and energy storage.

6. Results and discussion

6.1 Piezoelectric response of the self-sensing materials

The results of the electromechanical characterizations of the self-sensing materials described in the Chapters 4 and 5 are illustrated in the following.

6.1.1 Self-sensing material based on piezo-polymeric nanofibers

Different analyses were performed to characterize the self-sensing laminate response and to verify its ability to function as a sensor even for low-frequency applications. The piezoelectric output of the sensor was characterized in terms of curve fitting with the measured ground reaction force and stability over the time by means of accelerated fatigue tests. The signal linearity was evaluated over a wide force range and the parameters of the signal acquisition circuit were deeply studied with the aim to optimize the sensing capability of the sensor for quasi-static loads.

Together with the self-sensing laminate, the flexible piezoelectric sensor reported in Figure 4-8e was characterized without being integrated with the composite material. The purpose is to understand the effect of the integration in a GFRP matrix on the magnitude of the piezoelectric output.

Piezoelectric response to sinusoidal stimulus

The variation of the RC constant of the circuit of Figure 4-16 results in a variation of the amplitude of the piezoelectric response and a phase shift between the piezoelectric curve and the measured force [86]. In Figure 6-1 the piezoelectric output of flexible sensor, generated as response of a 200-500 N peak-to-peak compressive sinusoidal load at a frequency of 2 Hz, is reported for different RC values of the equivalent circuit by changing the values of R_{load} and C_{load} . The test setup is described in section 4.1.10. The same tests are repeated for the self-sensing laminate, as reported in the graphs of Figure 6-2.

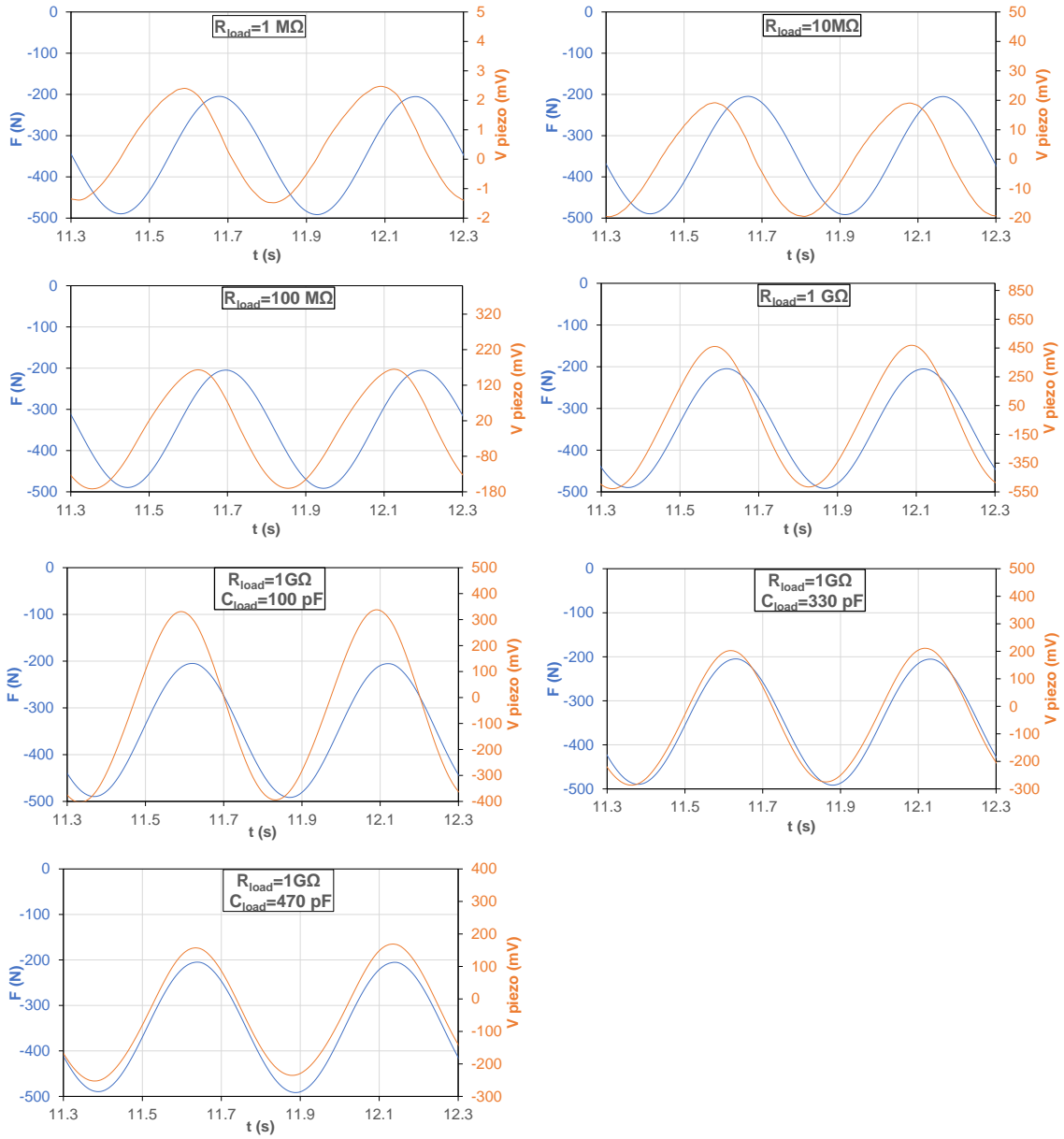


Figure 6-1 Piezoelectric output of the flexible sensor compared with the applied 2 Hz sinusoidal compression force of 300 N for different RC constant, obtained by changing R_{load} and C_{load} .

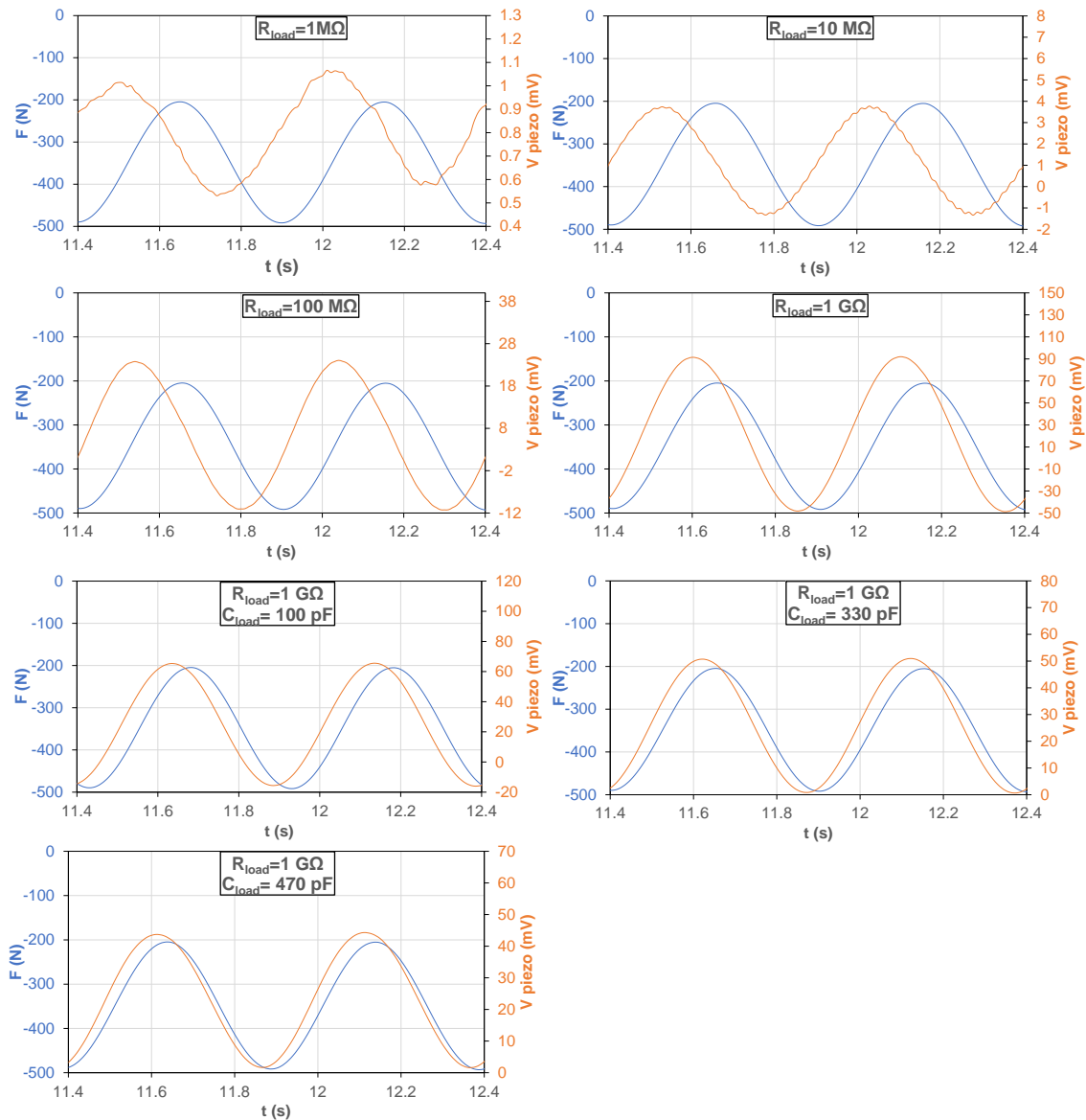


Figure 6-2 Piezoelectric output of self-sensing laminate compared with the applied 2 Hz sinusoidal compression force of 300 N for different RC constant, obtained by changing R_{load} and C_{load} .

Similar behaviors are registered for the piezoelectric outputs of the flexible piezoelectric sensor (Figure 6-1) and of the self-sensing laminate (Figure 6-2), but an attenuation of the piezoelectric output amplitude is observable for the self-sensing laminate, due to the presence of the external GFRP layer which reduces the load transferred to the nanofibers. For both the specimens, a remarkable phase shift between the piezoelectric curve (orange curve) and the load cell signal (blue curve) occurs in case of low values of the RC constant of the circuit, as shown in the cases of $R_{load} = 1 \text{ M}\Omega$ and $R_{load} = 10 \text{ M}\Omega$. The phase shift between the two signals is gradually reduced by increasing the value of R_{load} , whose maximum value in this work was set at $1 \text{ G}\Omega$. In this case ($R_{load} = 1 \text{ G}\Omega$), the amplitude of the piezoelectric response presents its maximum value, but still a phase shift with the applied force curve is noticeable. Therefore, a further increase of the R_{load}

value could result in a decrease of the mismatch between the two curves, but higher R_{load} values would be in the range of the insulating resistances of the system and would not affect the piezoelectric output. Consequently, a strategy to boost the RC constant of the circuit consisted in adding a capacitor C_{load} in parallel to R_{load} (Figure 4-16), which was fixed equal to 1 G Ω . The C_{load} capacity values tested in this work are equal to 100 pF, 330 pF and 470 pF. As observable in Figure 6-1 and Figure 6-2, the higher the C_{load} value the lower the phase shift between the two curves, in particular in the case of $C_{load}= 470$ pF, where the piezoelectric output curve and the load cell signal basically overlap.

However, an increase of the C_{load} value results in a reduction of the magnitude of the piezoelectric response. Therefore, a compromise between the sensitivity of the piezo-sensor and the phase shift with the force curve has to be defined accordingly with the designed application of the sensor and the frequency range of the mechanical stimuli. For instance, if the piezoelectric sensor is supposed to work in a high-frequency environment (e.g. 100 Hz or 1 kHz), the addition of C_{load} could be unnecessary as the time period of the mechanical stimulus is already sufficiently lower than the RC constant. Instead, for the purpose of this PhD work, $C_{load} = 470$ pF is the minimal requirement for a proper detection of the ground reaction force during the Gait cycle, whose period is in the order of 1 second.

Sensitivity vs frequency

A change in the RC constant leads to a variation in the cut-off frequency f_c of the circuit. A deep investigation was then carried out by evaluating the sensitivities [mV/N] of the piezoelectric samples as the ratio between the peak-to-peak value of the piezoelectric voltage and the applied compressive force. A sinusoidal load oscillating between 200 N and 500 N was applied on the samples surfaces at different frequencies, by varying the R_{load} and C_{load} values. The experimental test were carried out both on the flexible piezoelectric sensor (Figure 6-3 and Figure 6-4) and on the self-sensing laminate (Figure 6-5 and Figure 6-6). The continuous lines of the graphs represent the theoretical value of the sensitivity, while the dots represent the experimental results.

The theoretical output voltage was calculated according to equation (4.4), where the d_{33} value of the flexible piezoelectric sensor and the self-sensing laminate can be calculated from the simplified form illustrated in equation (6.1). Indeed, in the case of high RC values compared to the frequency of the applied force ω , the exponential term and the first steady-state one can be neglected and equation (4.4) can be simplified as:

$$V(t) = \frac{F d_{33}}{C} \sin(\omega t) \quad (6.1)$$

For the piezoelectric flexible sensor, a piezoelectric coefficient of 0.4 pC/N was calculated according to equation (6.1) by setting a high RC values of the equivalent circuit (R_{load} equal to 1 G Ω , C_{load} equal to 100 pF) and compressing the sample with a sinusoidal load at of 20 Hz. The same procedure was repeated for the self-sensing laminate, whose d_{33} value was calculated equal to 36×10^{-3} pC/N. If compared with the coefficient of the original nanofibrous membrane (13 pC/N), such a lower d_{33} values can be attributed to the integration of the nanofibers into the hosting matrix (Figure 4-6) and then of the sensor in the composite (Figure 4-9), whose stiffnesses reduce the load transferred on the nanofibers and thus the generated charges.

In Figure 6-3 and Figure 6-4 are reported the results of the tests carried out on the piezoelectric flexible sensor, while Figure 6-5 and Figure 6-6 refer to the self-sensing laminate ones.

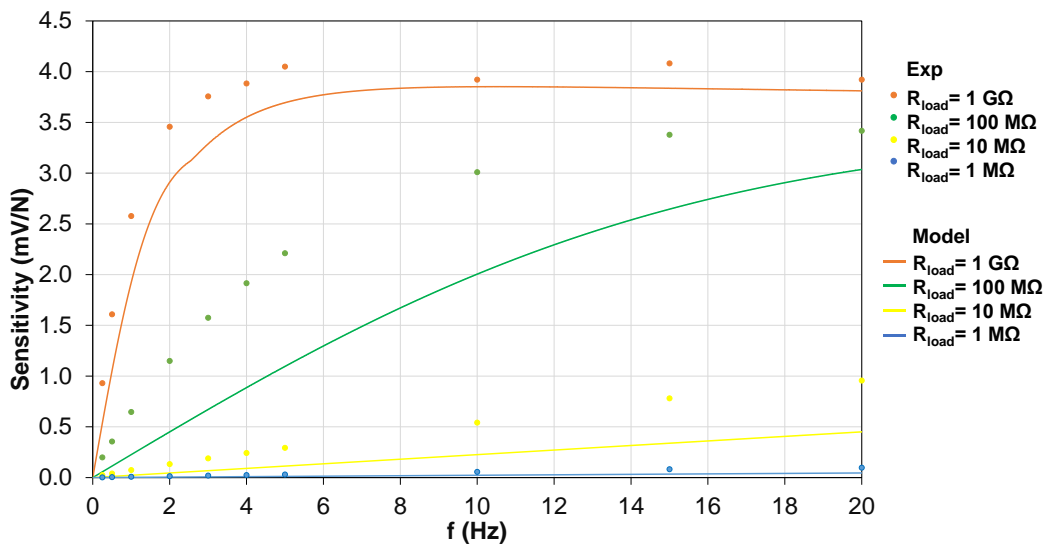


Figure 6-3 Sensitivity values of the piezoelectric flexible sensor versus frequency for different R_{load} and $C_{load} = 0$.

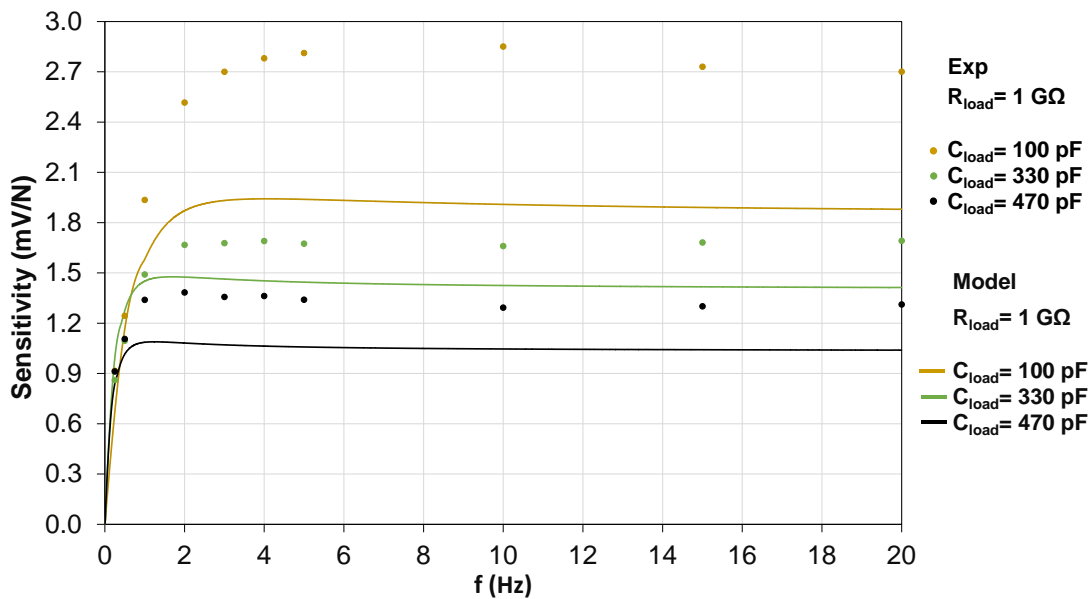


Figure 6-4 Sensitivity values of the piezoelectric flexible sensor versus frequency for $R_{load} = 1 \text{ G}\Omega$ and variable C_{load} .

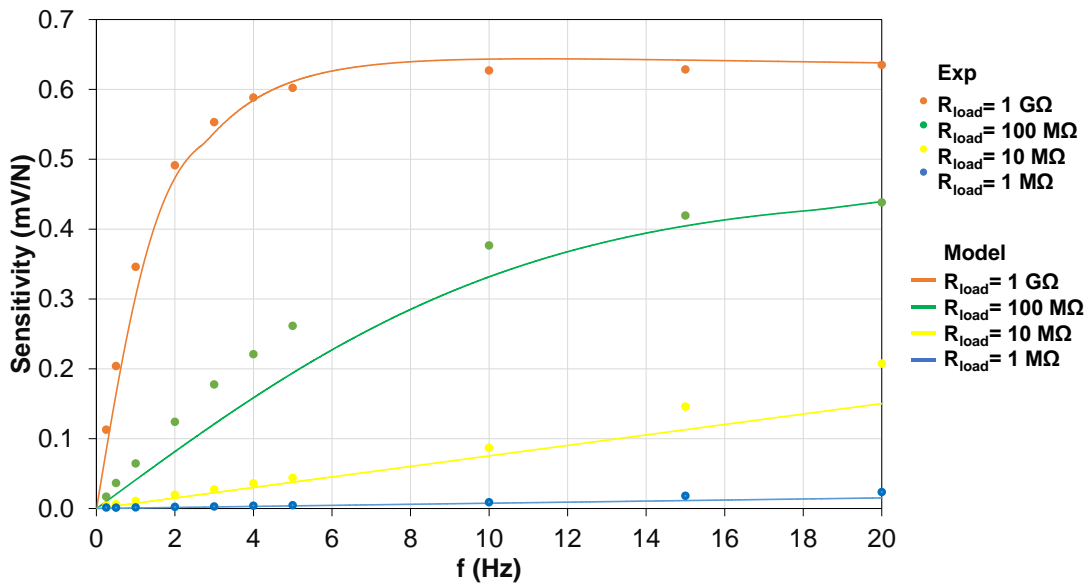


Figure 6-5 Sensitivity values of the self-sensing laminate versus frequency for different R_{load} and $C_{load} = 0$.

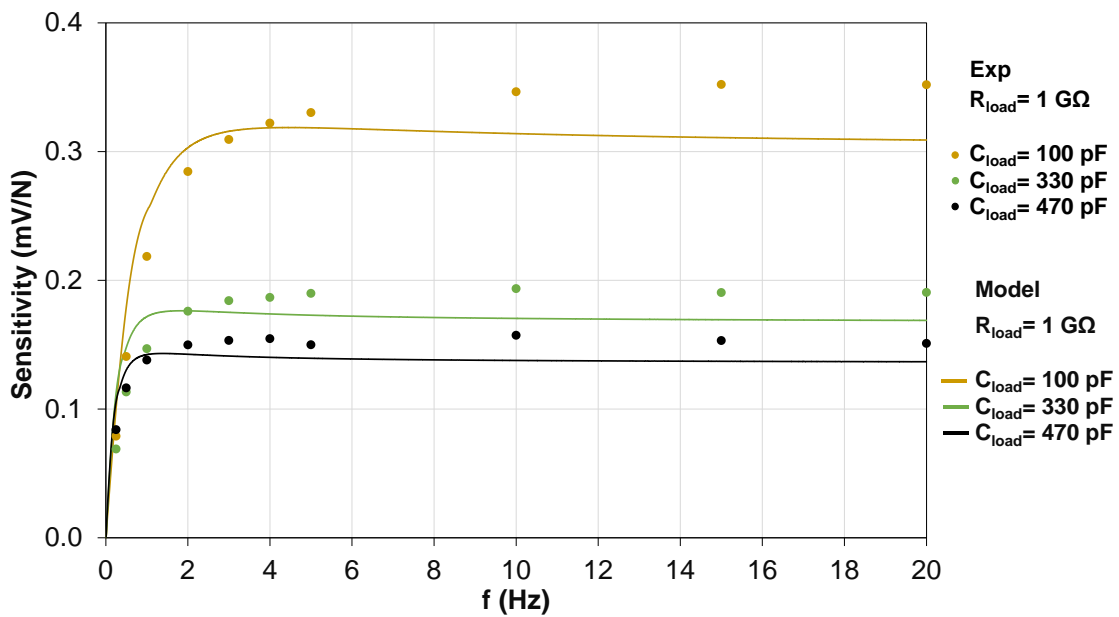


Figure 6-6 Sensitivity values of the self-sensing laminate versus frequency for $R_{load} = 1 \text{ G}\Omega$ and variable C_{load} .

Considering the cases where C_{load} was not connected, the general trend of the graphs of Figure 6-3 and Figure 6-5 shows a decrease of the f_c value as the RC constant increases, accordingly with the model prediction of equation (4.4) (continuous lines). In cases of R_{load} equal to $1 \text{ M}\Omega$ and $10 \text{ M}\Omega$ the plateau region is not reached at 20 Hz (the frequency limit of the compression stiffness was 20 Hz), both before and after the integration of the sensor in the laminate.

For each curve the cut-off frequency can be located in correspondence of a signal attenuation of 3 dB in the Bode diagram ($1/\sqrt{2}$ of the regime value). For $1 \text{ G}\Omega$ resistor the cut-off frequencies are equal to 1.6 Hz in both cases. Therefore, lower f_c values can be achieved only by connecting

in parallel to R_{load} (set at $1\text{ G}\Omega$) a capacitor (C_{load}), in order to increase the RC constant of the circuit. In Figure 6-4 and Figure 6-6 the sensitivity vs frequency responses are reported for C_{load} set at 100 pF , 330 pF and 470 pF .

Generally, by adding a capacitor C_{load} in parallel to the circuit, an attenuation of the sensitivity can be observed. In the case of $C_{load} = 470\text{ pF}$ and $R_{load} = 1\text{ G}\Omega$ resistance, the sensitivity is considerably reduced and the cutoff frequency f_c decreases from 1.6 Hz to 0.5 Hz . This configuration makes the sensor suitable for low-frequencies applications, such as ground reaction force detection capability in prosthetic systems, where the Gait cycle period is in the order of 1 second. With this circuit configuration, the sensitivity of the piezoelectric sensor is 1.3 mV/N and for the self-sensing laminate is 0.14 mV/N .

Linearity

For the aforementioned configuration ($C_{load} = 470\text{ pF}$ and $R_{load} = 1\text{ G}\Omega$), a linearity analysis has been performed by recording the piezoelectric peak-to-peak output voltage of the piezoelectric sensor (Figure 6-7) and the self-sensing laminate (Figure 6-8) for different exciting force amplitudes (up to 1 kN). The frequency was set at 2 Hz and the lower peak force at 200 N .

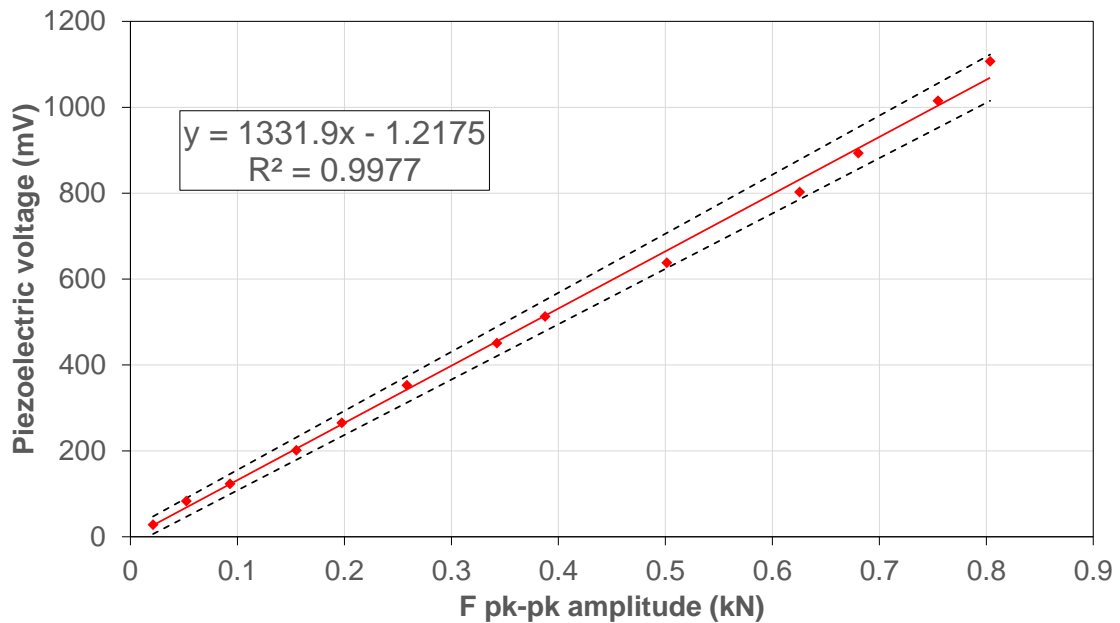


Figure 6-7 Linearity test of the flexible piezoelectric sensor, with $R_{load} = 1\text{ G}\Omega$ and $C_{load} = 470\text{ pF}$.

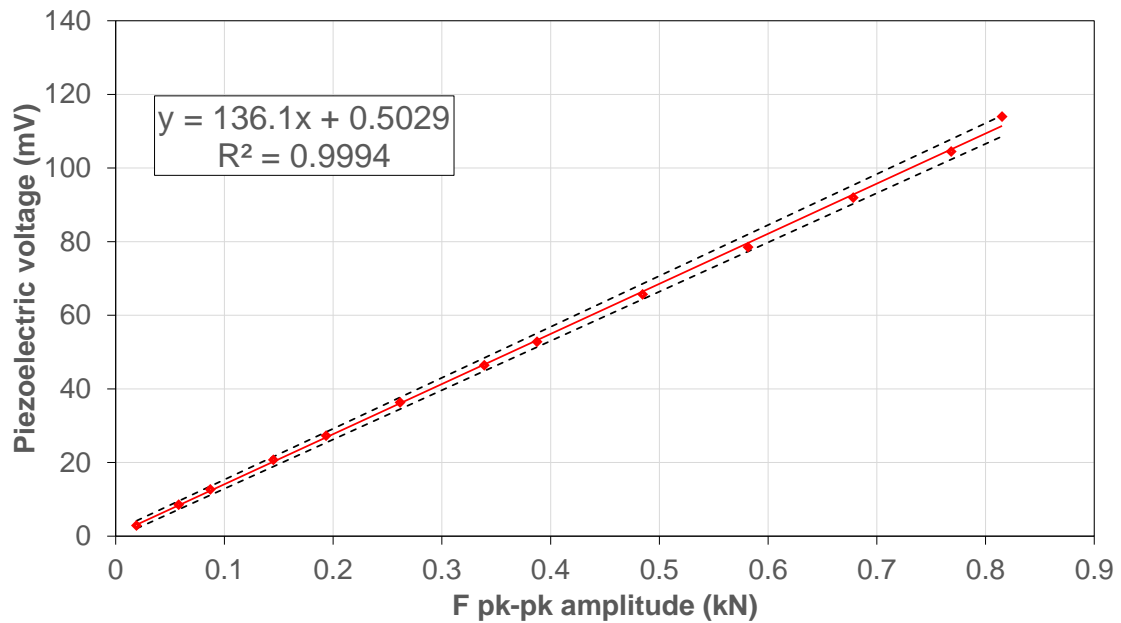


Figure 6-8 Linearity test of the self-sensing laminate, with $R_{load} = 1 \text{ G}\Omega$ and $C_{load} = 470 \text{ pF}$.

The piezoelectric sensor, before the integration in the composite, shows a sensitivity equal to $1332 \pm 62 \text{ mV/kN}$ with a coefficient of determination R^2 equal to 0.997 (Figure 6-7); whereas Figure 6-8 shows a sensitivity of the self-sensing equal to $136 \pm 3 \text{ mV/kN}$ with $R^2=0.999$.

Fatigue test

Accelerated cyclic fatigue tests were performed on the self-sensing laminate by applying a sinusoidal load oscillating between 1000 N and 400 N at 10 Hz frequency for 10^6 cycles by using the same setup described in section 4.1.10. For accurate detection of any alterations, the R_{load} value was set at $1 \text{ G}\Omega$ and $C_{load} = 0$, which is the condition with the highest amplitude of the piezoelectric response.

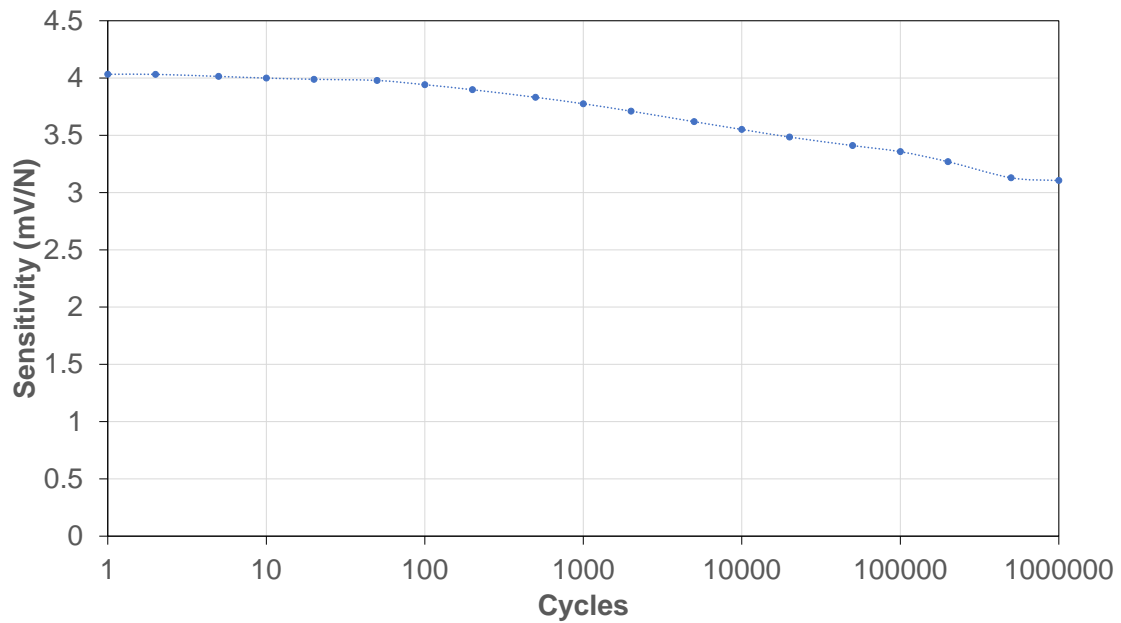


Figure 6-9 Sensitivity of the flexible piezoelectric sensor during the 10^6 cycles fatigue test..

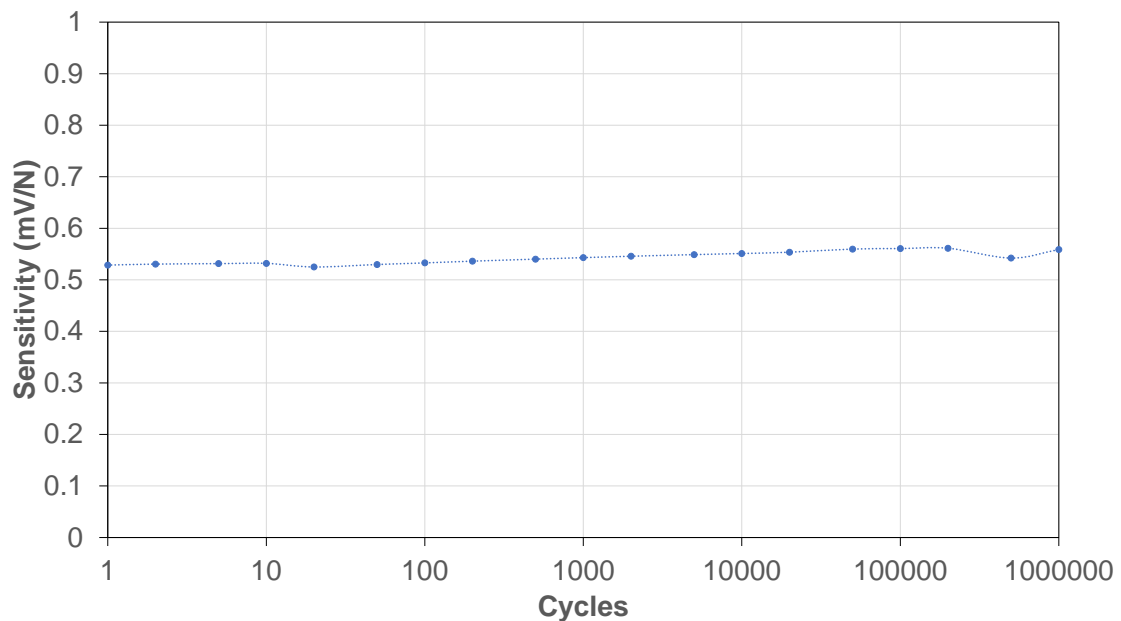


Figure 6-10 Sensitivity of the self-sensing laminate during the 10^6 cycles fatigue test..

As observable in Figure 6-9, at the end of the 10^6 cycles fatigue test the sensitivity of the piezoelectric sensor decreased from 4 mV/N down to 3.1 mV/N. In Figure 6-10, the self-sensing laminate output voltage did not present any significant variations during the test, preserving its sensitivity over the time. This difference is clearly attributable to the presence of the external layer of GFRP in the self-sensing laminate, which on the one hand decreases the sensitivity value but on the other protects the sensor, whose sensitivity is not affected during the 10^6 cycles.

Prosthesis sole

In the end, the sole was then mounted on the ankle-foot prosthesis (Figure 6-11) and compression tests were carried out by applying a load on the heel oscillating between 200 N and 800 N at 1 Hz frequency, in order to mimic the Gait cycle period. The piezoelectric response was acquired by using the same circuit configuration of Figure 4-16. In these tests, no amplifications were performed and R_{load} was set at 1 G Ω and C_{load} at 470 pF.

As it can be observed in Figure 6-11a, the piezoelectric signal accurately follows the ground reaction force, with a sensitivity value equal to 0.11 mV/N. Further analyses were then carried out with the same procedure by putting on the prosthetic foot the footshell and then the shoe, as shown in Figure 6-11b and Figure 6-11c. Indeed, normally the prosthesis users wear a footshell and often a shoe during their motorial activities. It can be observed that with the footshell the piezoelectric signal amplitude is reduced by 75%, due to the soft rubbery material which attenuates the load transferred to the nanofibers and thus the generated charges. No further reductions are observed by adding the shoe.

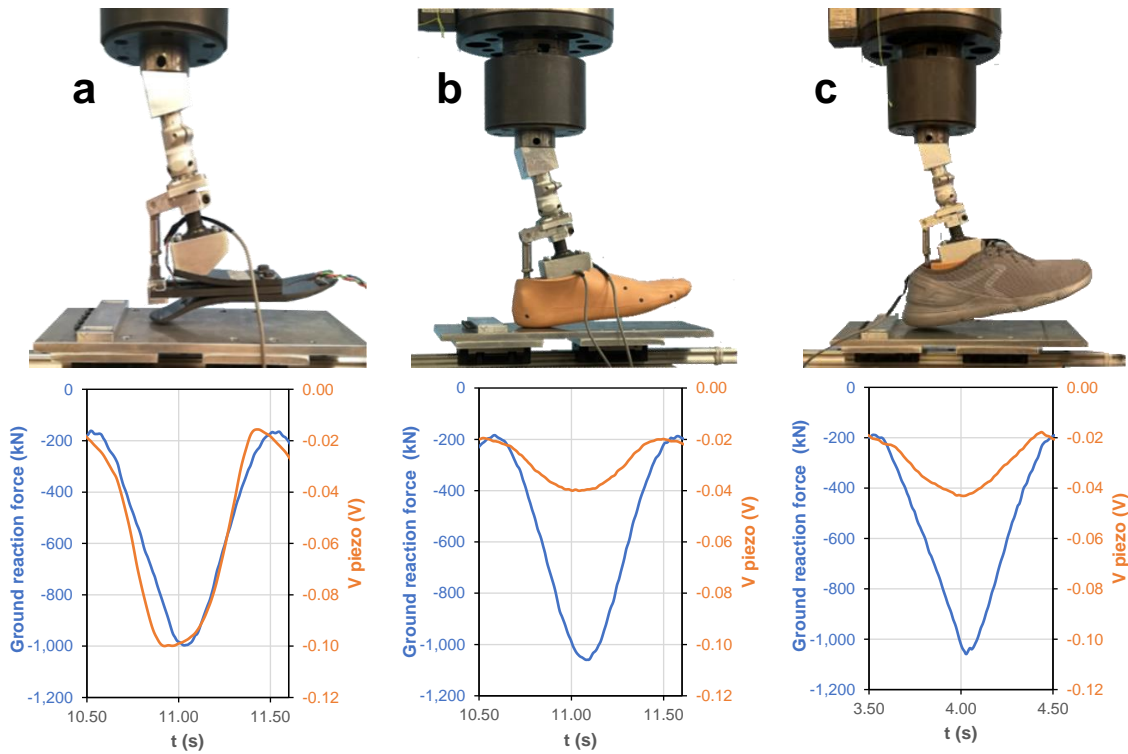


Figure 6-11 Piezoelectric response of the sensor integrated in the heel of the prosthetic sole (a); with footshell (b) and shoe (c) mounted on it.

6.1.2 Position flexible piezoelectric sensor based on core-shell nanofibers

The piezoelectric core-shell nanofiber-based sensor was characterized as described in section 4.2.7. The indenter impact position on the surface of the sensor was changed and the piezoelectric signal was simultaneously acquired for each electrode. The surface of the sensor presents 9 impactable positions, as result of the 3-core electrodes placed on the edges. Obviously, an increase of the number of the core electrodes would lead to a finer localization of the impact position.

As the indenter of Figure 4-33 impacts one of the 9 available positions with a force of 100 N, the three signal amplitudes of each side sides of the sensor are compared. Qualitative representations of the outputs comparison are reported in Figure 6-12 and Figure 6-13 for an impact occurred in the central position of the sensor (red circle). As desirable, the signal amplitudes of the electrodes number 2 and number 5 exceed the other electrode ones of the corresponding belonging side. Such a comparison easily leads back to the impact position thanks to the matrix disposition of the aligned nanofibers.

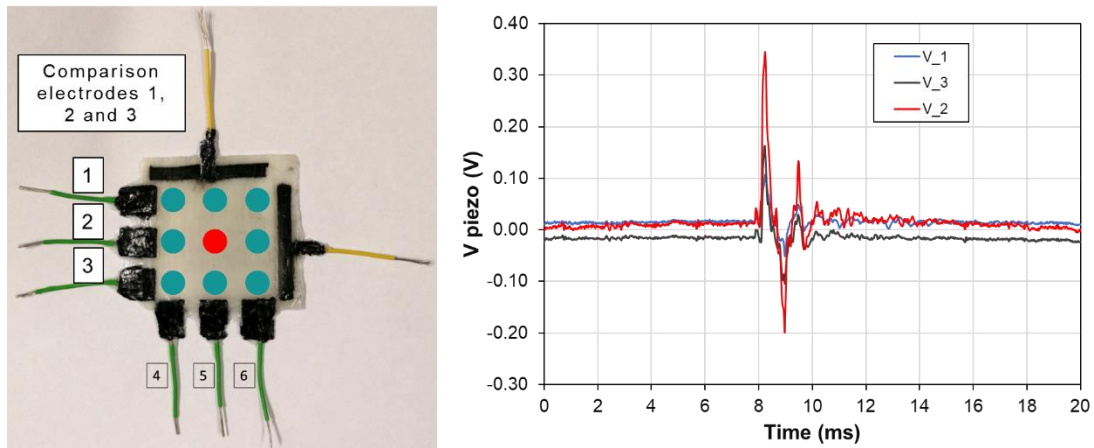


Figure 6-12 Comparison of the output voltage of electrodes 1, 2 and 3 for an impact in the central position.

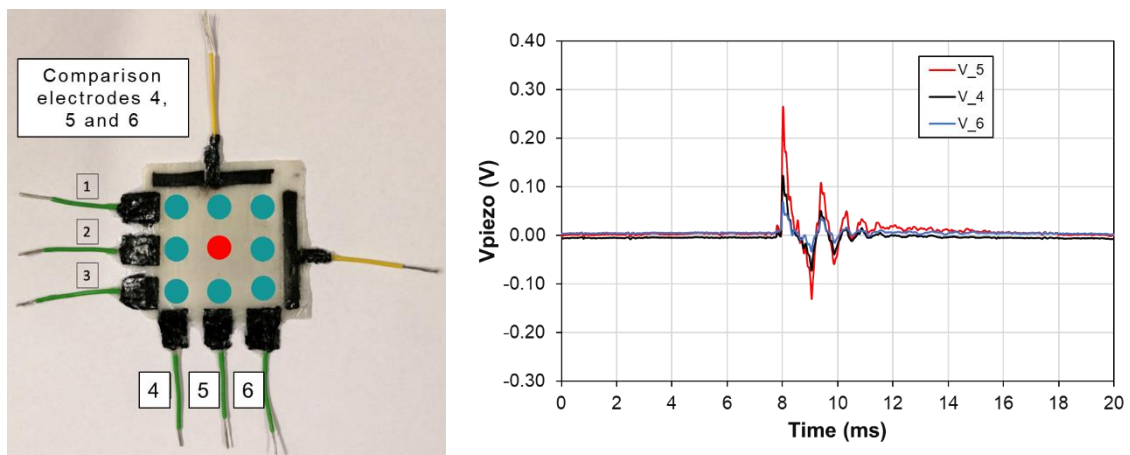


Figure 6-13 Comparison of the output voltage of electrodes 4, 5 and 6 for an impact in the central position.

The sensor reliability was tested by impacting its surface for three times in all the 9 available positions. The average of the peak-to-peak output voltage values of the three measurements are reported in Table 6-1 for each impacting position and the highest piezoelectric output for each electrode row is written in red.

Table 6-1 Piezoelectric outputs of the sensor for each impacting position.

Impact position	Electrodes piezo output (mV)					
	V_1	V_2	V_3	V_4	V_5	V_6
1 x 4	433	118	95	341	201	113
1 x 5	345	98	93	151	413	117
1 x 6	418	83	122	134	181	332
2 x 4	111	301	99	289	85	77
2 x 5	155	532	253	181	390	101
2 x 6	62	250	147	133	160	279
3 x 4	97	88	295	380	109	73
3 x 5	112	91	301	94	293	132
3 x 6	129	132	334	116	111	354

6.1.3 Self-sensing laminate based on ceramic nanopowder

The effect of the PZT powder interleaving between the plies of the composite material was studied as a function of the volumetric fractions of the laminates. First, the piezoelectric responses are reported and compared with the commercial PZT disk one. The measured piezoelectric strain coefficients of the laminates (g_{33}^C) are the parameters that were considered for the model validation. Indeed, their theoretical calculation requires the application of both the polarization and piezoelectric models (sections 4.3.4 and 4.3.5, respectively).

In the end, the use of PZT powder instead of a PZT commercial disk is evaluated in terms of mechanical integrity of the structure at the impact point.

Piezoelectric response

The piezoelectric response of the sensing laminates was evaluated by compressive cyclic loads at a frequency of 25 Hz, as described in section 4.3.8. As reported in Figure 6-14, the piezoelectric output voltages of the samples accurately follow the applied force. The effect of the variable GFRP volume fraction is clearly observable for all the cases of PZT areal densities. The number of GFRP plies between the piezoelectric element and the electrode was varied, resulting in a reduction of the insulating thicknesses from the -G8 laminates to the -G2 ones. Indeed, an increase of the piezoelectric response amplitude from the -G8 laminates to the -G2 ones is registered. Moreover, for the same number of GFRP layers between the electrodes, the sensitivity increases for higher PZT powder amounts.

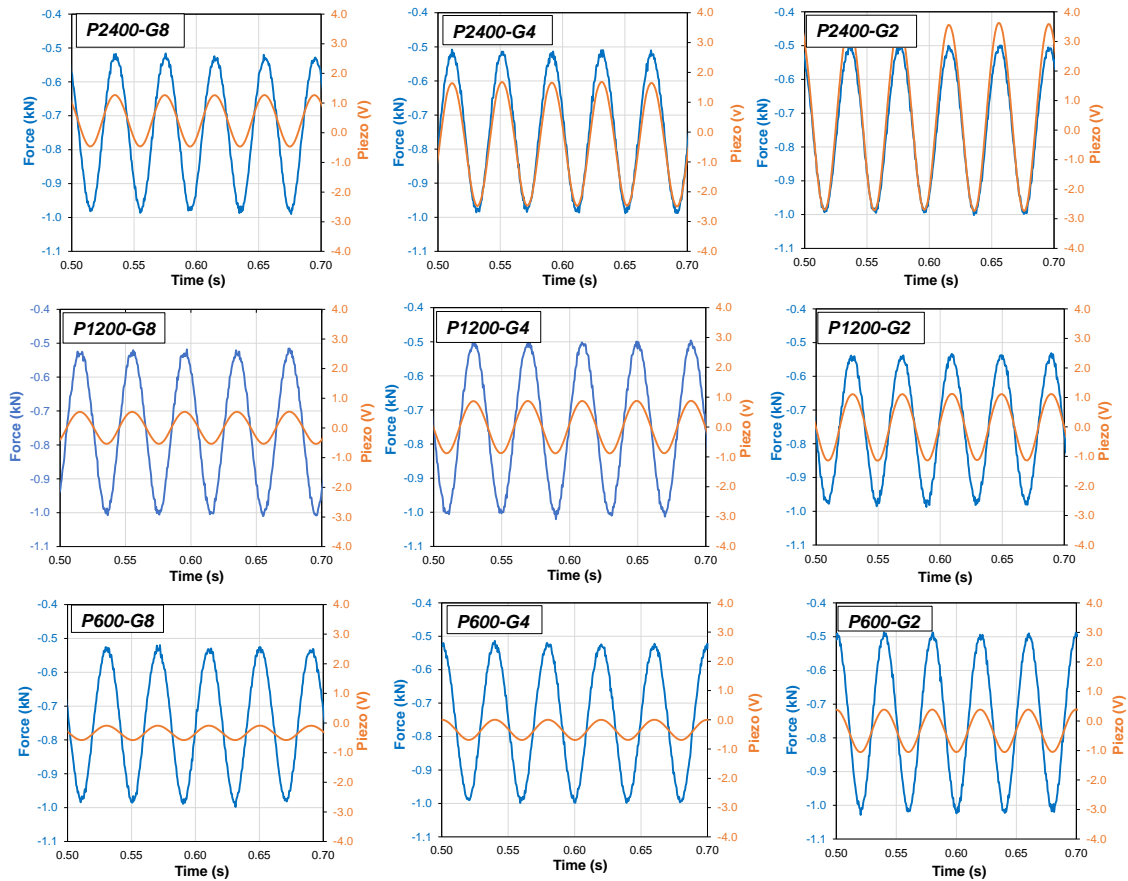


Figure 6-14 Piezoelectric response of the sensing laminate (orange curve) compared to the contact force measured by the indenter load cell (blue curve) for powder sensor with different plies of GFRP within the electrodes (8-4-2, respectively) and different amount of PZT powder.

The effect of the different GFRP/PZT volume fractions was also investigated in terms of sensitivity of the laminates. The sensitivity of each laminate is calculated as the ratio of the peak-to-peak value of the piezoelectric output to the applied force and is reported in Figure 6-15 as function of the number of GFRP plies between the electrodes. If compared with the COM laminate – where the piezoelectric element is a commercial PZT disk – the sensitivity presents higher values in the case of PZT powder interleaving, especially 2400 g/m² PZT powder areal densities.

Moreover, a lower amount of GFRP plies between the piezoelectric phase and the electrodes results in higher sensitivities, as the path of the charges towards the electrodes is reduced. On the other hand, lower value of sensitivity is registered in case of 600 g/m² of PZT areal density and 8 GFRP plies within the electrodes, which is the configuration with the thickest insulating layer that the generated charges have to flow through.

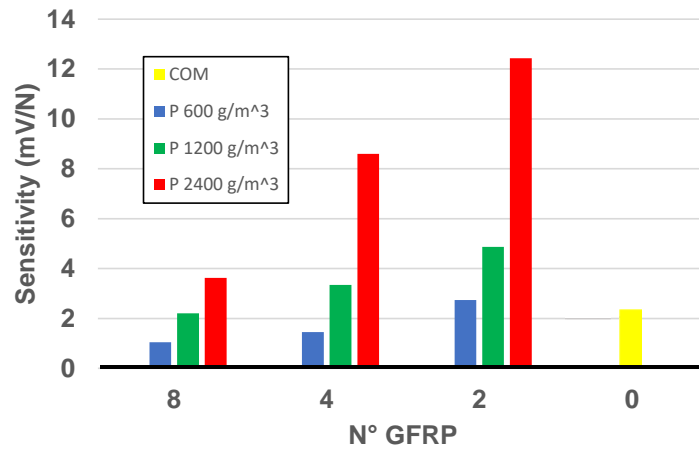


Figure 6-15 Sensitivity vs number of GFRP plies for commercial and powder sensing laminates.

To summarize, for the PWD laminates configurations, the experimental results and the model predictions are reported in Table 6-2. The experimental piezoelectric voltage coefficient of the composite laminates g_{33}^C was used as reference parameter for the validation of the model-predicted voltage piezoelectric coefficients g_{33}^{C*} .

Table 6-2 Experimental vs model electrical parameters for each laminate configuration.

	CONFIGURATION		EXPERIMENTAL				MODEL		
	d within the electrodes (mm)	v^P PZT vol fraction	C (pF 10^{-12})	ϵ_3^C (F/m 10^{-12})	d_{33}^C (pC/N)	g_{33}^C (Vm/N 10^{-3})	E_3^P (kV/mm)	g_{33}^P (Vm/N 10^{-3})	g_{33}^{C*} (Vm/N 10^{-3})
P2400-G8	2.42	0.14	14.5	73	0.05	0.72	0.87	6.9	0.95
P2400-G4	1.44	0.24	27.5	103	0.24	2.29	0.96	8.3	2.04
P2400-G2	1.08	0.39	44.7	136	0.56	4.07	1.13	11.0	4.31
P1200-G8	2.17	0.07	14.4	65	0.03	0.49	0.82	6.1	0.45
P1200-G4	1.29	0.14	23.8	77	0.08	1.03	0.87	6.9	0.95
P1200-G2	0.88	0.24	44.3	110	0.22	1.96	0.96	8.3	2.04
P600-G8	2.06	0.04	16.1	73	0.02	0.23	0.80	5.6	0.22
P600-G4	1.11	0.07	24.2	68	0.04	0.52	0.82	6.1	0.45
P600-G2	0.72	0.14	45.0	92	0.12	1.35	0.87	6.9	0.95

The experimental and the model parts of Table 6-2 summarize the procedure for the evaluation of the g_{33}^C and g_{33}^{C*} (red highlighted), respectively. In the configuration part, for each laminate the distance between the two brass sheets electrodes and the volume fractions of the piezoelectric phase are reported for all the specimens. The procedure to evaluate the experimental piezoelectric voltage coefficient of the laminates g_{33}^C is reported in the experimental part of Table 6-2. First, the capacitance of each self-sensing laminate is measured (see section 4.3.8). The dielectric constants of the composite materials ϵ_3^C were then calculated according to equation (4.11) by knowing the distance between the electrodes, d , and their surface, S . Furthermore, the

d_{33}^C values of the composite laminates were indirectly calculated according to equation (4.12), where the voltage piezoelectric outputs were measured in the compressive cycle tests described in section 4.3.8. In the end, the experimental g_{33}^C were easily calculated as the ratio of the d_{33}^C and the dielectric constant ϵ_3^C for each laminate.

The model-predicted g_{33}^{C*} coefficients of the composite laminates are red highlighted in the third part of Table 6-2. The procedure for their evaluation is the results of the combination of the polarization model (section 4.3.4) with the piezoelectric model (section 4.3.5) for the composite structures. The polarization model allowed the electric field that was applied on the piezoelectric phase E_3^P during the polarization process of the laminates to be evaluated. Consequently, the piezoelectric strain coefficient of the piezoelectric phase (d_{33}^P) was derived by the interpolating equation (4.8), which correlates the polarization electric field values with the correspondent d_{33}^P of a commercial PZT disk. This approach is very approximate, because the same d_{33} value measured on the PZT disk is used as the d_{33}^P value of the PZT phase in the laminate, which is, instead, in the shape of powder. In the end, consistently with [115] and [116] - where the piezoelectric composite laminate is modeled as the series connection between the structural phase (GFRP) and the piezoelectric phase (PZT) - the piezoelectric voltage coefficients g_{33}^{C*} of the self-sensing laminates were calculated according to equation (4.10).

The differences between the g_{33}^C coefficients calculated from the experimental results and the model-predicted g_{33}^{C*} ones can be observed by comparing the last columns of the experimental part and of the model part of Table 6-2. For the sake of clarity, the g_{33}^C and g_{33}^{C*} coefficients are also graphed in Figure 6-16 as a function of the PZT volumetric fraction, v^P .

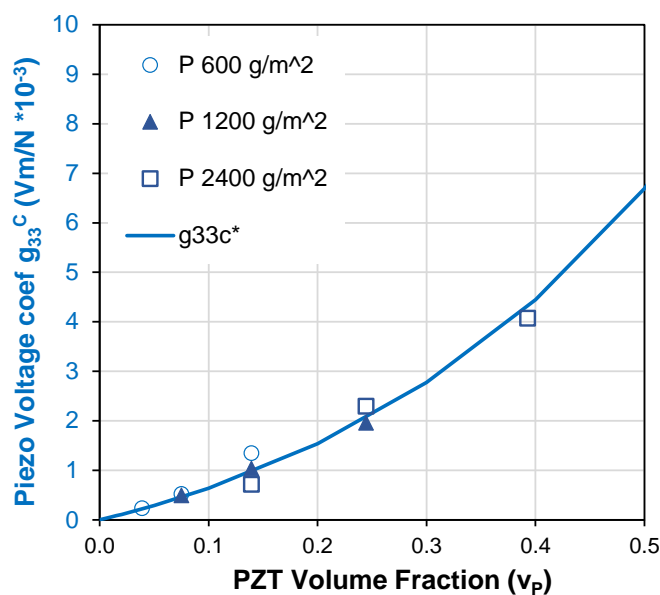


Figure 6-16 Model-predicted (g_{33}^{C*}) and experimental (g_{33}^C) piezoelectric voltage coefficients of the composite laminates.

Overall, the experimental g_{33}^C values match with good approximation the model predictions with a coefficient of determination $R^2 = 0.967$. Nevertheless, some differences are observable, in particular in the case of P600-G2 laminate – where the model underestimates the experimental g_{33}^C with a 29% error – and in the case of P2400-G8, which present a g_{33}^{C*} that is 33% higher than the experimental g_{33}^C .

As previously mentioned, some discrepancies between the model-predicted g_{33}^{C*} and the experimental g_{33}^C were reasonably expectable. Indeed, the polarization model describes the poling electric field distribution between the two phases of the laminate by approximating the PZT powder as a stiff layer. Instead, the PZT powder presents some differences in the particles size distribution and the dispersion between the laminate plies is not perfectly uniform, with consequent inhomogeneity of the electric field that is applied on every single particle during the polarization process. Moreover, a further approximation occurs when the d_{33} value measured on the commercial PZT disk is assumed as d_{33}^P value for the PZT powder in the laminate. However, this is an unavoidable approximation, as the polarization and the d_{33} measurement of the PZT powder by itself is not practically feasible.

Impact resistance

The effect of embedding piezoelectric PZT with different morphologies and quantities on the impact resistance of the hosting material was evaluated by low-velocity impact, following the procedure described in section 4.3.8 and by micrograph analyses of the impacted zone. Only one sample was manufactured for each configuration.

In Figure 6-17 the impact contact force vs displacement responses for the different laminate types are plotted. For all the graphs, the non-sensing laminate (REF) was plotted for comparison. As shown in Figure 6-17a, the curve of the laminate with the embedded commercial sensor (COM, red line) presents multiple load drops, correlated to the fragile breakages of the ceramic disk. Such remarkable drops are not observed in the case of PZT powder interleaving, as shown in Figure 6-17b-d, suggesting a limited impact of the PZT powder on the mechanical performance of the laminates.

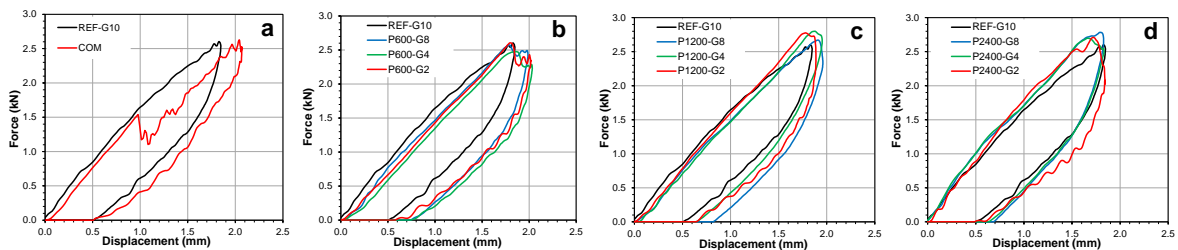


Figure 6-17 Low velocity impact test at 3 J: impact contact force vs displacement response.

In the end, the cross-sections of the laminates at the impact point were observed at the optical microscope. In Figure 6-18, the most significant samples are shown and the crack or delamination are highlighted with red arrows.

Reference laminate shows few small 45°-oriented matrix cracks which propagate as negligible delamination between the GFRP layers at the midplane.

A completely opposite behavior is observed in the case of PZT commercial sensor integration (COM laminate), where the lower brass sheet electrode totally debonded from the piezoelectric disk, as previously predicted from the force-displacement graphs of Figure 6-17. Moreover, cracks can be observed also in the PZT disk.

Concerning the powder laminates with PZT areal density equal to 1200 g/m², P1200-G8 shows debonding of the electrodes, but it does not occur in case of P1200-G4 and P1200-G2, where the electrodes are interleaved into the laminate. At the midplane, a 45° oriented crack propagating in a reverse pine tree pattern is observable in the case of P1200-G2; whereas P1200-G4 presents a slightly visible crack.

By analyzing the images as a function of the areal density, all the specimens with 600 g/m² PZT powder do not show matrix cracks through the PZT layer, as observable in Figure 6-17 in the case of P600-G4. On the other hand, P2400-G4 presents a remarkable 45° oriented crack across the PZT layer which propagates parallelly at the interface between the GFRP ply and the PZT layer.

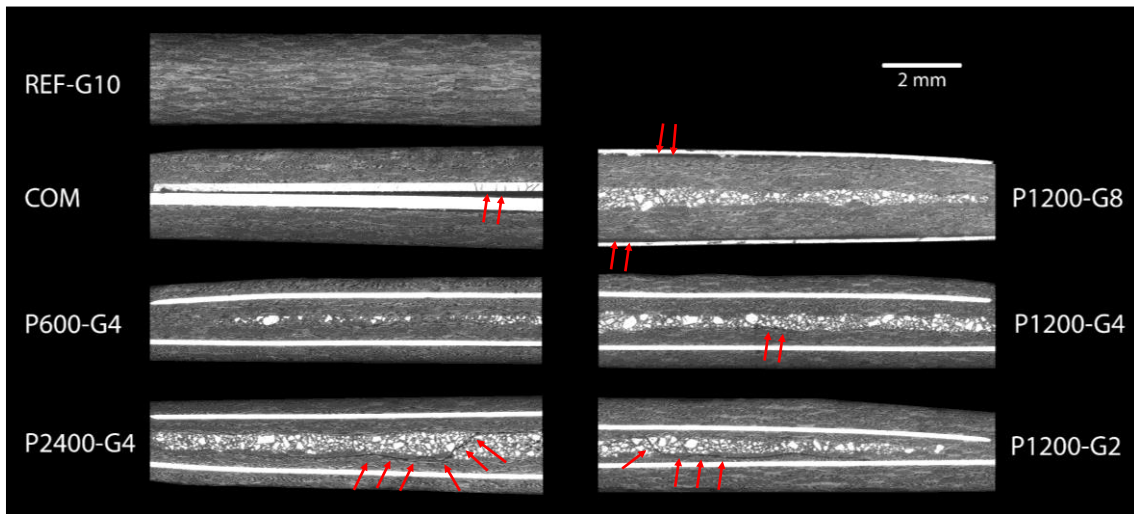


Figure 6-18 Micrograph analysis of the cross-section laminates at the impact point.

6.2 Piezoelectric-based device for energy harvesting

6.2.1 Maximum power transfer

PVdF-TrFE nanofibers and PZT disk

A first analysis conducted on the power transfer capability of the piezoelectric samples (PVdF-TrFE nanofibers embedded in PDMS matrix and PZT commercial disk) provided information about the generated power for different R_{load} and frequency values with the instrumentation setup of Figure 5-3. The comparison between the two considered specimens is shown in the graphs of Figure 6-19 for the PZT disk and of Figure 6-20 for the PVdF-TrFE nanofibers.

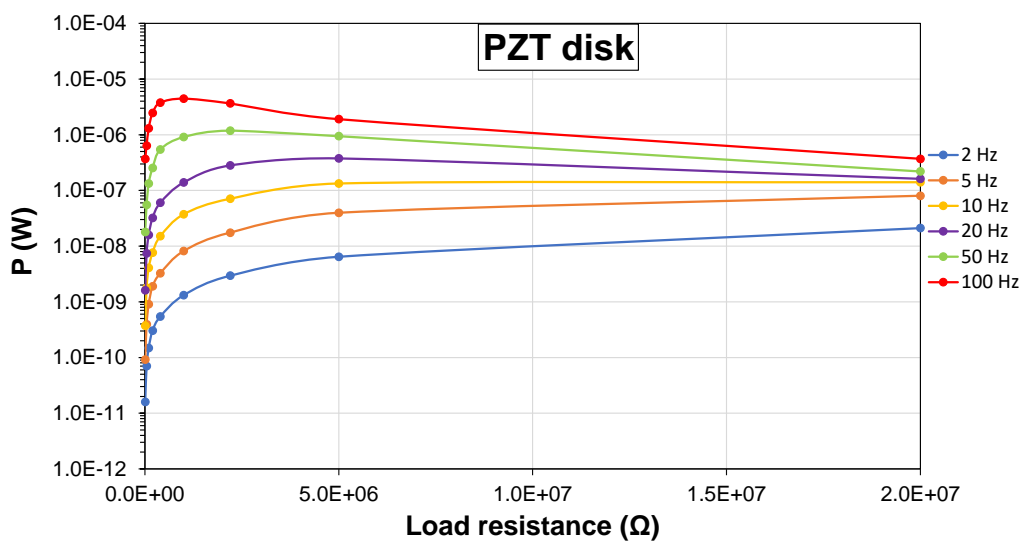


Figure 6-19 RMS power of the PZT disk at different values of frequency and load resistance, as result of a sinusoidal compressive load of 20 N.

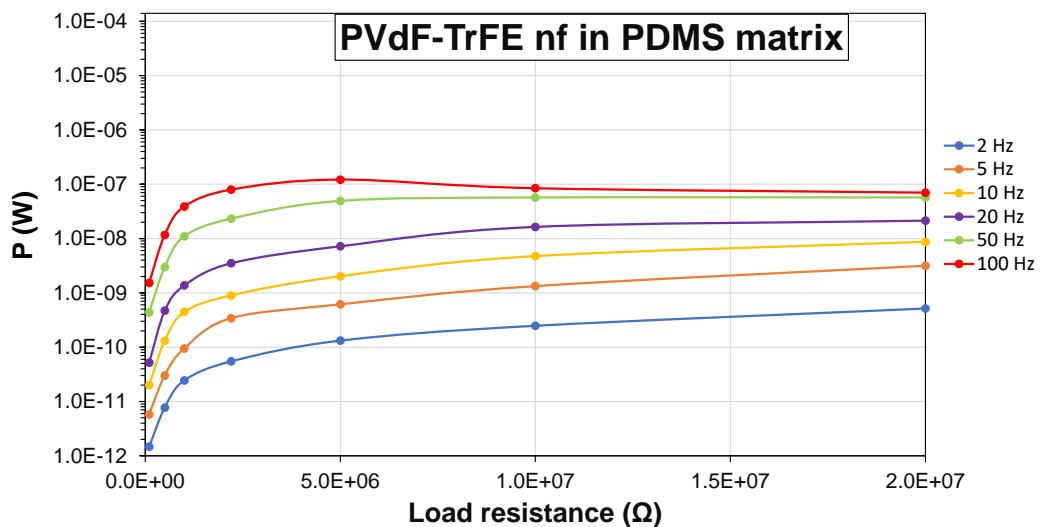


Figure 6-20 RMS power of the PVdF-TrFE nanofibers embedded in PDMS at different values of frequency and load resistance, as result of a sinusoidal compressive load of 20 N.

For both the tested specimens, an increase of the output power with the compressive load frequency is observable. In the case of 100 Hz frequency, the PZT disk presents an output power 50 times greater than that of PVdF-TrFE and similar differences are observable for all the frequency curves. For decreasing frequency values, the resistive load value corresponding to the maximum power point increases. For instance, with a resistive load of 1 M Ω , the 100 Hz power curve of the PZT disk (red line of Figure 6-19) presents a power peak of 5 μ W, which is 5000 times higher than the power value obtained in case of 2 Hz power curve (blue line of Figure 6-19). An appropriate tuning between the resistance load and the frequency of the application is then a crucial aspect for the optimization of the system efficiency.

However, in Figure 6-19 and in Figure 6-20 the peak power outputs of PZT and PVdF-TrFE are not reached in the case of low-frequency values (e.g. 2 Hz, 5 Hz and 10 Hz curves), which are the most interesting ones for wearable applications or prosthetic systems designed to harvest energy from the walking cycle. Therefore, further analyses were performed on the PZT commercial disk by fixing the frequency of the compressive load at 2 Hz, as shown in Figure 6-21. The output power of the piezoelectric disk was measured for higher mechanical loads (30 N, 60 N and 90 N) and the load resistance range was broadened from 1 k Ω to 1 G Ω . In this case the sinusoidal loads were applied on the specimen by a linear motor, as described in section 5.2.3.

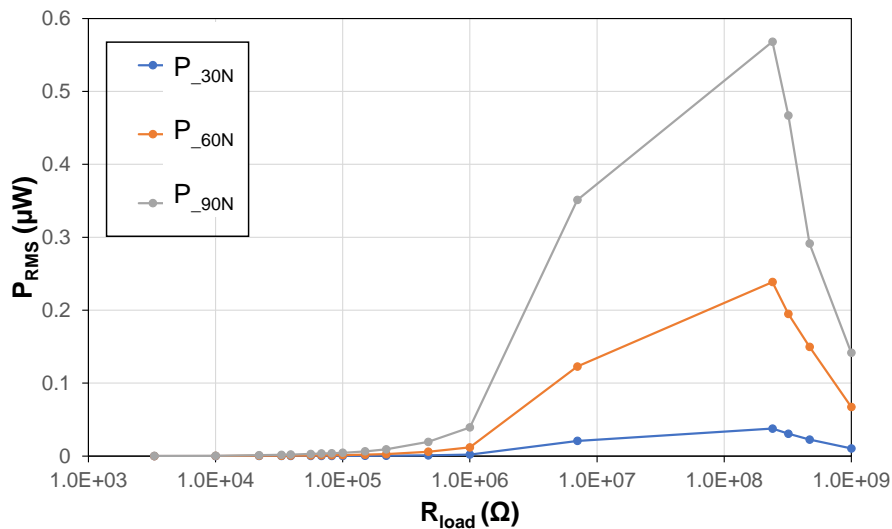


Figure 6-21 P_{RMS} values for PZT for different R_{load} values at 30N, 60N and 90N, 2 Hz sinusoidal loads.

The maximum power point for all the three force values corresponds to a load resistance of 200 M Ω . In the case of a 90 N compressive force (yellow curve), the power peak is equal 0.57 μ W, which is a relative low value, but further improvements to the systems are possible, for instance by connecting in parallel multiple PZT disks. Moreover, by considering a 90 kg person, with a simple interpolation it is possible to predict a peak value of power RMS around 50 μ W.

However, it is worth highlighting that the extremely brittle and fragile morphology of the PZT

disk dramatically narrows its application fields. Excessively high mechanical loads applied on its surface would easily break the ceramic disk and in case of flexible applications even small bends would result in dramatic failures of the component. In this context, PZT nanofibers are a promising way to conjugate the feasibility of the nanofibrous layers to be integrated into flexible hosting materials and the high piezoelectric response of the ceramic PZT.

PZT nanofibers

After the polarization in ester oil, the nanofibrous ceramic layer was characterized in terms of transferable power for different R_{load} values, as shown in Figure 6-22.

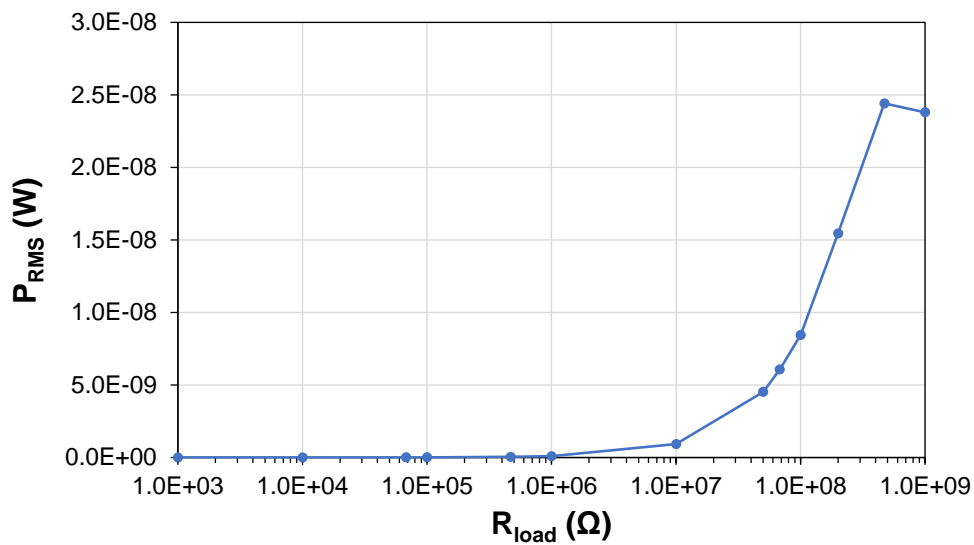


Figure 6-22 P_{RMS} value of the PZT nanofibrous layer as function of R_{load} .

Similarly with the value obtained with the PZT disk, the load resistance for the PZT nanofibers is around 400 M Ω , but the power peak reaches 24 nW, which is still considerably lower than the PZT disk maximum power (570 nW). However, despite the lower amount of power, the nanofibers integration still results in better mechanical properties if compared with the integration of a PZT disk, avoiding any delamination risks.

6.2.2 Energy storage

Capacitor charging

The 100 nF capacitor was charged by compressing the piezoelectric PZT disk with a sinusoidal load at 2 Hz frequency. The charging curves are graphed in Figure 6-23.

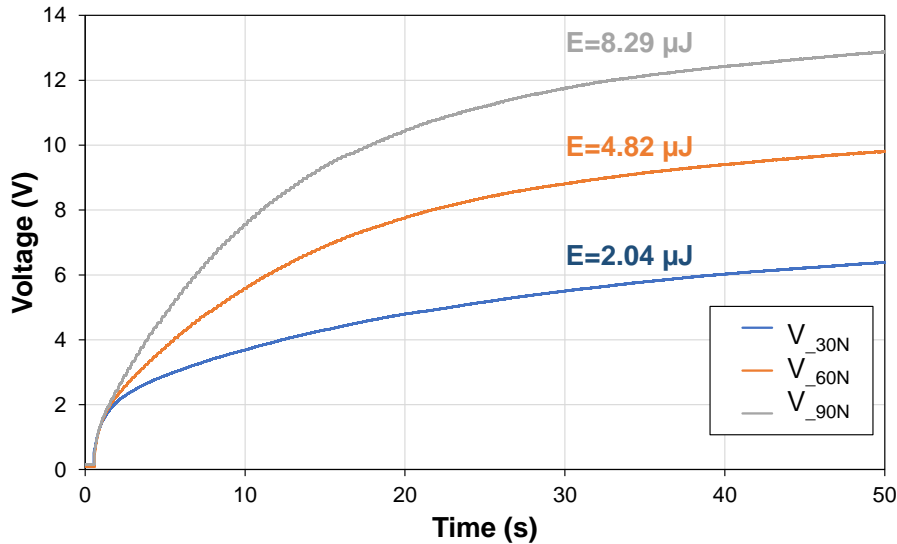


Figure 6-23 Capacitor charging curves at 30N, 60N and 90N sinusoidal forces.

As expected, the higher values of energy and power were achieved with the 90 N amplitude force, with an average power value of 0.17 μW and 8.3 μJ of collected energy.

By connecting in parallel two or more PZT disks the output current would increase proportionally and the charging process of the capacitor would result faster, allowing the collection of a bigger amount of energy.

For this purpose, four parallel-connected PZT disks were fixed in the sole of a shoe and protected by an encapsulating structure, as reported in section 5.3.1. After the 5 minute walk, the voltage across the capacitor was measured by the electrometer to be around 2.9 V, which corresponds to 0.2 mJ with an average power of 0.7 μW .

Piezoelectric-supercapacitor coupling

The energy unit and the coupling system of the piezo-supercapacitor system were described in section 5.3.2.

The supercapacitor charge process was performed by applying a sinusoidal load to the energy harvesting unit of 90 N amplitude at 2 Hz. The quantities measured during the charging process

(Figure 6-24) are the voltage of the supercapacitor, the current provided by the piezoelectric unit and the power, calculated as $P = V \cdot I$.

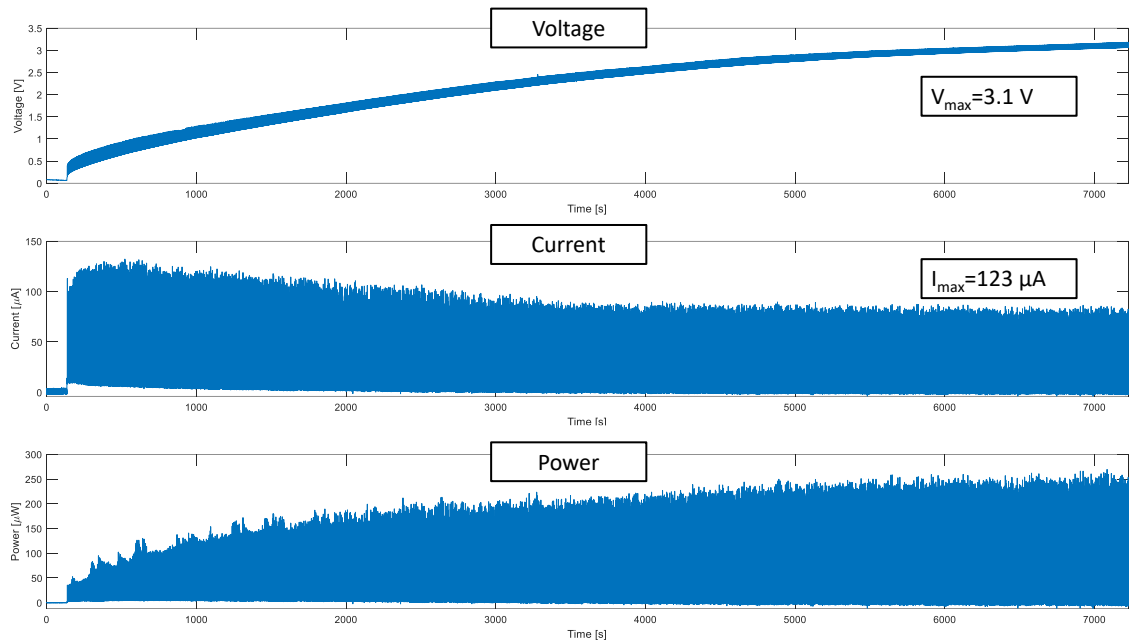


Figure 6-24 Charging process curves: voltage, current and power.

The voltage charging curve follows the typical charging trend of a capacitor and after 2 hours reaches a value slightly higher than 3 V. It is worth highlighting that as the linear motor applies a 2 Hz frequency sinusoidal load on the piezoelectric samples, the supercapacitor receives a 4 Hz electric signal thanks to the full wave diode bridge rectifier. The thicker aspect of the initial part of the voltage curve is attributable to the presence of higher voltage peaks that are correlated to the internal resistance of the supercapacitor. The current presents a maximum value of 120 μA in the initial part of the process and follows a decreasing trend, before stabilizing finally at 80 μA.

The amount of energy provided by the piezoelectric unit to the supercapacitor can be calculated by integrating the power over the time with the trapezoidal rule (equation 6.2) and is equal to 227 mJ.

$$E = \int_t^{t+\delta t} P(t') dt' \quad (6.2)$$

The supercapacitor discharge process was initiated by switching the SPDT relay and was monitored by simultaneously measuring the voltage drop of the supercapacitor and the output current (Figure 6-25). The power and the energy were calculated as reported above.

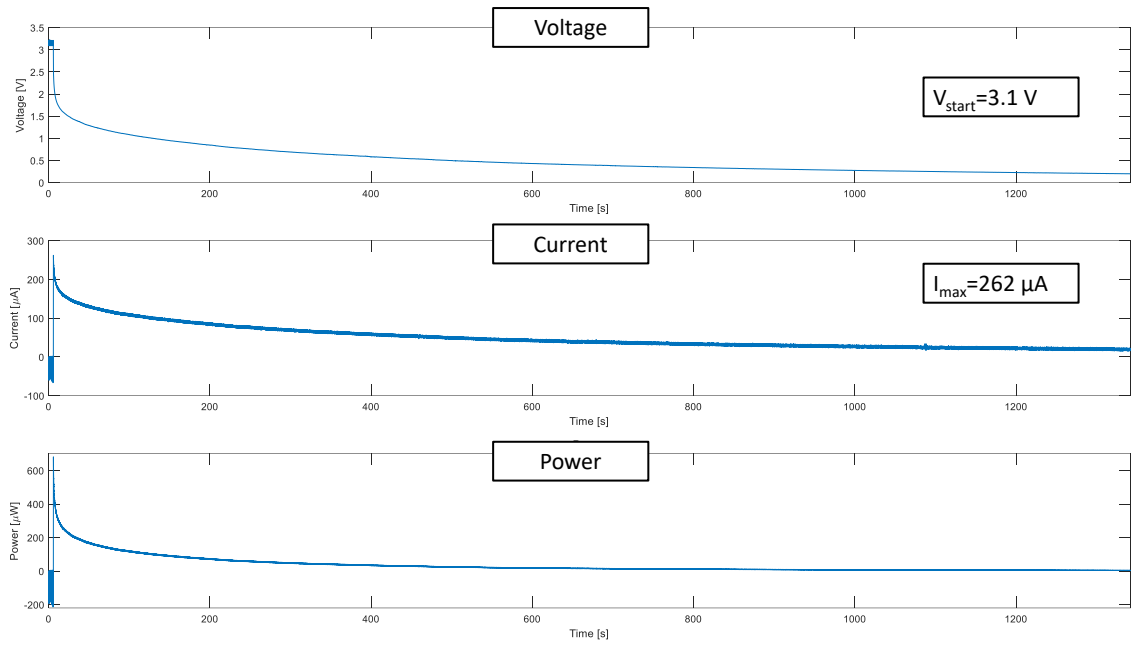


Figure 6-25 Discharge process curves: voltage, current and power.

The load resistance R_{load} was accurately chosen to be 10 k Ω . Indeed, lower resistances would have concealed the initial vertical drop associated to the losses of the not negligible internal resistance of the supercapacitor. Of course, with such high value of load resistance the RC circuit time constant increases and the discharge time period of the supercapacitor extended up to 15 minutes.

7. Conclusive remarks

PVdF-TrFE nanofibers in composite materials

The interleaving of PVdF-TrFE nanofibers within a composite material successfully resulted in the realization of a self-sensing laminate, that exploit the self-powering capability of the piezoelectric phase for the detection of pressures on its surface. The advantages of adopting nanofibrous membranes instead of piezo-films were clearly evidenced by micrograph analyses of the cross section of the laminate, that did not present delamination. The sensing capability of the laminate was optimized by properly tuning the acquisition circuit parameters (R_{load} and C_{load}) and the piezoelectric signal fit the measured ground reaction force also in case of quasi-static loads. Indeed, by modeling the piezoelectric element as a voltage generator, the resulting behavior of the sensor is similar to a high-pass filter, whose cut-off frequency depends on the RC constant of the equivalent circuit. By setting $R_{load} = 1 \text{ G}\Omega$ and $C_{load} = 470 \text{ pF}$, the cut-off frequency of the sensor was reduced down to 0.5 Hz, making the sensor suitable for low-frequency applications, such as Gait cycle or wearable devices. Before to be integrated in the laminate, the flexible sensor was electromechanically characterized and the piezoelectric output voltage presented a linear behavior over a wide force range (0 - 800 N), with a directly proportionality coefficient equal to $1.3 \pm 0.06 \text{ mV}$. The measured linearity of the sensor showed coefficient of determination R^2 equal to 0.997. The integration of the sensor in a flat composite material - whose epoxy matrix is compatible with the epoxy resin/polyurethane mixture that constitutes the piezoelectric sensor – was successfully achieved. Carbon black based electrodes were preferred to traditional metallic sheets in order to remove any material discontinuities and to increase the mechanical adhesion with the epoxy matrix of the laminate. As predictable, lower sensitivity values were measured for such a piezo-composite material, as the external GFRP layer encapsulating the sensor reduces the load transferred to the nanofibers and thus the generated charges. The sensitivity of the self-sensing laminate resulted to be one order of magnitude lower than the piezoelectric sensor one ($0.14 \pm 0.01 \text{ mV/N}$). However, the external GFRP layer protects the sensor both mechanically and electrically, reducing the noise caused by triboelectric effects. Moreover, accelerated fatigue tests (10^6 cycles at 10 Hz, compressive force oscillating between 400 N and 1000 N) did not affect the sensitivity of the laminate, whereas the piezoelectric flexible

sensor shows a drop of its sensitivity equal to 21% of its initial value.

A piezoelectric model was used to predict the response of both the flexible piezoelectric sensor and the self-sensing laminate, based on the piezoelectric strain coefficient d_{33} of the specimens. The experimental results matched with a good approximation the theoretical value of the sensitivity, measured for different value of R_{load} and C_{load} .

The integration of the nanostructured sensor in the sole of the prosthesis was successfully performed thanks to the flexibility of the materials, that adapts to curvilinear geometries. The mechanical test on the sole showed a sensitivity of 0.11 mV/N, coherently with the behavior investigated for the flat self-sensing specimen tested in the previous characterization.

Even if the sensing performances of the piezoelectric materials can be adapted for quasi-static loads, drawbacks are evident in the case of measurements of constant pressures. If a patient with the transfemoral prosthesis stands for an extended time of period, the piezoelectric nanofibrous membrane will provide sensing information for a partial period, as result of the intrinsic nature of piezoelectricity.

Future developments of the PVdF-TrFE nanofibrous piezoelectric sensor regard the possibility to further enhance its piezoelectric performance. In this work, the polarization process carried out in ester oil resulted in a d_{33} value equal to 15 pC/N, which is still comparable with the d_{33} coefficients of the commercial PVdF-TrFE films. Moreover, considering the highly porous structure of the nanofibrous membrane, the specific piezoelectric properties are then dramatically enhanced. However, a further increment of the d_{33} value can be obtained by initially applying to the nanofibers an alternate electric field which increases the dipoles movement. In this way, as second stage of the process, the DC field action would be more effective also on the hardly orientable dipoles, thus enhancing the piezoelectric behavior of the nanofibers.

Piezoelectric core-shell nanofibers for impact localization

The core-shell nanofibers were produced by coaxially electrospinning a conductive polymer (PEDOT:PSS) as a core and a piezoelectric polymer (PVdF-TrFE) as shell. The study of the rheological properties of the solutions used during the electrospinning process led to the optimization of the core-shell morphology of the nanofibers; whereas the micrograph analyses provided an ex post approach to identify which are the viscosity values of the polymeric solutions that ascertain the coaxial morphology of the fibers. The geometrical matrix disposition of the aligned fibers provided a free-electrodes surface area with 9 impactable positions (3 x 3 electrodes on the sensor edges). The impact load applied on the different positions of the sensors was properly localized by comparing the signal output of the electrodes. Multiple tests confirmed the repeatability of the measurements and the feasibility of such a sensor to work as impact locator.

If compared with the traditional pressure nanofibrous piezoelectric sensors produced via mono-fluid electrospinning, the core-shell geometry of those nanofibers enables to arrange the nanostructured electrodes (polymeric conductive core and thin metal coating) adjacent to the piezoelectric part of the fiber, thus enhancing the amplitude of the output signal. Indeed, in the traditional sandwich-like structures, the flow of the piezo-generated electric charges is reduced proportionally to the insulating thickness between the electrodes and the central piezoelectric layer; whereas in the designed core-shell nanofibers the charges are immediately collected by the electrodes without any dissipative paths.

The drawbacks mainly regards the manufacturing process of the sensor. During the electrospinning process, a not-uniform deposition of the core-shell nanofibers on the collecting area could lead to a mismatch of sensitivities in the sensing surface. Moreover, the electrical connection between the nanoscale electrode with the macroscale ones that are disposed on the edge of the sensor is a critical aspect during the manufacturing process. In this work, the six core electrodes provided a surface with 3x3 sensitive positions, each of which has a 0.5×0.5 cm dimensions. To fully exploit the potentiality of using every single nanofiber as a nano-sensor and achieve a nanometric resolution of the impact localization, ideally every single nanostructured electrode should be connected to the macroscale acquisition system, as schematically represented in Figure 7-2. Therefore, to achieve such a high resolution, the electrical connections with the conductive cores require techniques with a micrometric precision. Moreover, it is not always ensured that the cores of the nanofibers face the cross section of the sensor in a clear and smooth manner, making its connection further challenging even after a fragile break in nitrogen.

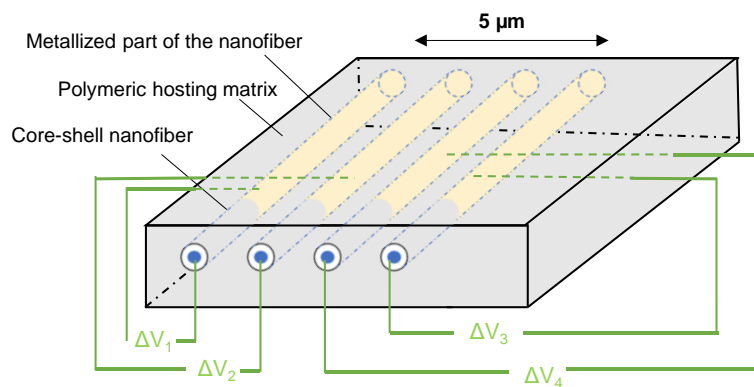


Figure 7-1 Ideal nanometric resolution of the sensor: every single nanofiber works as a sensor.

The future developments of this self-sensing technique are then oriented toward a substantial improvement of the impact localization resolution of the sensor by designing methods for a finer connection between the core signals and the external electrodes. As before mentioned, the higher

the number of electrodes disposed in the edges of the sensor surface, the higher the impact localization efficiency.

PZT nano-powder in composite materials

PZT ceramic powder was successfully produced and interleaved between the laminates plies of GFRP-based composite materials. The amount of piezoelectric powder and the number of GFRP layers between the electrodes were varied with the purpose to understand the effect of different volume fractions on the piezoelectric output and on the impact resistance of the laminates.

The piezoelectric powder generally presents higher sensitivity values if compared with commercial PZT disk. This behavior can be attributed to a higher surface-volume ratio that enhance the charges generation and their flowing towards the electrodes. Moreover, the powder interleaving limitedly impacts the mechanical strength of the laminates, as demonstrated by the micrograph analyses of the cross section at the impact point. On the contrary, the PZT disk debonded from the brass sheets electrodes and initiated the crack propagation, whereas smaller or null delamination occurred in case of PZT powder interleaving in the laminates.

A polarization model was adopted to predict the piezoelectric strain coefficient of the PZT phase (d_{33}^P) and combined with a piezoelectric model for the theoretical evaluation of the piezoelectric voltage coefficient of the self-sensing composite material (g_{33}^{C*}). The so calculated trend of g_{33}^{C*} was validated with a good approximation by the experimental results (g_{33}^C , see Figure 6-16). The specimens fabricated in the experimental campaign present variable PZT volumetric fractions, up to $\nu^P=0.39$.

Further considerations can be added by extending the model up to $\nu^P=1$, as reported in Figure 7-2. The piezoelectric voltage coefficient g_{33}^{C*} (blue curve) presents a parabolic-like trend which increases with the volume fraction ν^P . This behavior suggests that enhanced value of sensitivity could be achieved by increasing the amount of piezoelectric phase within the laminate plies. However, a compromise between the piezoelectric performances of the laminate and its mechanical strength has to be identify, as an excessive value of the PZT areal density could initiate the crack propagation.

Therefore, this model can provide important information for the design of piezoelectric self-sensing laminates according to its final application. If the composite material is designed for high impacts monitoring, then low volumetric fraction of PZT are recommended in order to preserve its mechanical integrity. On the other hand, if the application field does not present excessive mechanical stresses, higher self-sensing performances can be explored without mechanical failure

risks. In both cases, the amplitude of the piezoelectric response can be priorly predicted after the manufacturing process of the laminate.

Moreover, the red curve of Figure 7-2 represents the model prediction of the piezoelectric strain coefficient of the composite d_{33}^C , which rapidly decreases for small amounts of the GFRP phase. Indeed, for $v^P = 0.9$ the d_{33}^C of the composite drops to 3% of the d_{33}^P value of the pure PZT. This behavior suggests that the composite laminate can be properly used for sensing applications with a wide range of PZT volumetric fractions (v^P), whereas high and unfeasible v^P values are necessary for actuator applications.

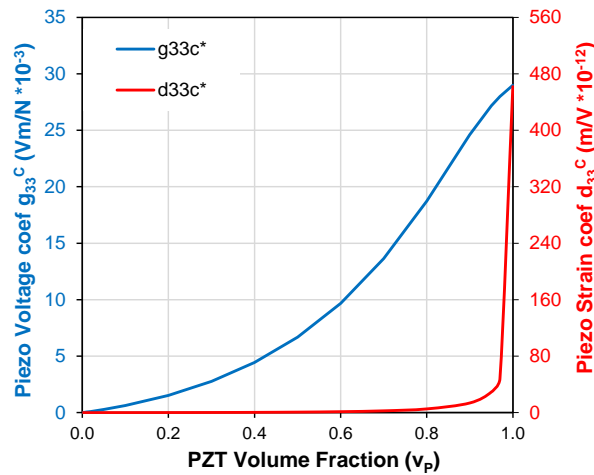


Figure 7-2 Composite piezoelectric voltage coefficient g_{33}^{C*} (blue curve) and strain coefficient d_{33}^C (red curve) vs PZT volume fraction v^P , estimated by the model.

Future works will focus on the production of self-sensing laminates with higher piezoelectric volumetric fractions v^P , in order to validate the model even for $v^P > 0.39$. Moreover, with the aim to further reduce the risk of delamination in the composite, semi-conductive electrodes can be used to replace the original brass sheets ones. Micrograph analyses evidenced cases of debonding of the brass sheets electrodes from the GFRP ply, with consequent risk of cracks initiation. A promising strategy to increase the adhesion in this interface is to add conductive nanoparticles to the epoxy layer which is compatible with the resin of the GFRP plies, creating a semi-conductive electrode.

Energy harvesting

The energy harvesting capability of piezoelectric materials was explored both in terms of instant power transferring to a resistive load and energy storing.

As predictable from the d_{33} values of the materials, the power obtained with a PZT disk is considerably higher if compared with a polymeric PVdF-TrFE nanofibrous layer. For a

compressive load of 90 N applied on the PZT disk at a frequency of 2 Hz, 57 μ W were registered as a power peak for a resistive load of 200 M Ω . Reasonably higher powers can be obtained in case of higher compressive load amplitudes and by connecting in parallel multiple piezoelectric elements. However, the integration of a brittle PZT ceramic disk in a composite material easily results in mechanical problem of the hosting structure. Indeed, too high compressive loads could break the disk and subsequently start a crack propagation in the composite material. For this reason, the power transfer capability of ceramic PZT nanofibers was evaluated. In the case of wearable and flexible applications or integration in a hosting matrix, the use of nanofibers is more recommended as the intimate contact between the nanofibers and the hosting material prevents delamination risk. The maximum power point transfer measured at 2 Hz for the PZT nanofibrous layer was found for a resistive load of 400 M Ω , with a power peak of 24 nW. Even if the output power is three orders of magnitude lower than a commercial PZT disk, improvements can be done in the polarization process of the nanofibers in order to achieve higher d_{33} , for instance by poling the nanofiber under an AC electric field or with corona poling procedure.

The parallel investigation on the coupling of the piezoelectric element with a storage system were performed on PZT ceramic disk. The insertion of 4-parallel connected PZT disks in the sole of a shoe was performed to store energy in a 100 nF capacitor after 5 minutes walking of a 70 kg person. The 0.2 mJ stored in the capacitor were then used to light a LED for half a second.

In conclusion, a scale-up of the system was made by stacking 15-parallel connected PZT disk in a vertical disposition, thus transferring the same force magnitude on each element. The charging process of the energy storage unit – consisting of a supercapacitor manufactured in the Department of Chemistry “Giacomo Ciamician” at the University of Bologna – took place for 2 hours under a 90 N compressive force. Remarkably higher values of energy stored were reached and the supercapacitor exhibits a typical discharge curve trend over a resistive load of 10 k Ω . An energy transfer efficiency equal to 21% was calculated as the ratio between the energy provided by the piezoelectric unit ($E_{\text{piezo}} = 227$ mJ) and the extractable energy from the supercapacitor ($E_{\text{supercap}} = 48$ mJ).

With the aim to adapt the piezoelectric-supercapacitor system to wearable devices, future activities will focus on the replacement of the PZT disks with PZT nanofibers as energy harvesting unit. In this way, such a system would be suitable to be placed in strategic point to capture energy from the body movements, such as the elbow, the ankle, the knee or the shoulder straps of a backpack. To do this, the piezoelectric performances of the PZT nanofibers are to be enhanced; for example by studying more effective polarization processes (e.g. corona poling or alternate electric fields) or by designing a system with multiple PZT nanofibrous layers connected in parallel.

Final considerations

Multifunctional composite materials were successfully manufactured in this work by means of nanostructured piezoelectric materials. The research activities were carried out on two main strands, regarding the self-sensing and energy harvesting capabilities of the produced specimens.

Piezoelectric-based self-sensing materials were successfully fabricated by using both polymeric PVdF-TrFE and ceramic PZT. The polymeric nanofibers flexibility was exploited for the production of flexible specimens based on the direct piezoelectric effect. Two nanofiber-based sensors were developed according to two distinct working principles. First, a flexible pressure sensor was designed and integrated into a composite material. The experimental results showed a great capability of such a nanofibrous sensor to detect also quasi-static loads and micrograph analyses were carried out after fatigue tests. The absence of delamination and mechanical damages demonstrated the high potential of piezo-nanofibers to functionalize composite materials in a non-intrusive manner. Second, piezoelectric core-shell nanofibers were successfully used to create a multifunctional material able to detect the impact position on its surface. The disposition of the core-shell nanofibers resulted in a sensor with free-electrode surfaces, which is a useful feature in specific applications (e.g. in. biomedical field). The non-intrusiveness of the piezo-sensing technique was demonstrated also in case of PZT micrometric powder dispersion in the composite laminate, in particular if compared with the integration of commercial PZT disk. However, some mechanical problems could still occur in case of high PZT powder areal density and at the interface between the brass electrodes and the GFRP plies.

The next natural steps will be to improve and to refine the self-sensing capabilities of the produced materials. This means, in the cases of the PVdF-TrFE nanofiber-based and the PZT powder-based composite materials, to enhance piezoelectric performances keeping an eye on the mechanical compactness of the laminate. Instead, for the core-shell nanofiber-based sensor, the improvements regard the achievement of a finer spatial resolution of the impact position on the sensor surface. Together with the self-sensing laminate development, energy harvesting strategies have been explored by using piezoelectric transducers. The high piezoelectric coefficient of ceramic PZT disks makes them more recommended for energy harvesting purposes if compared with piezo-polymers. The piezoelectric source was successfully coupled with a storage system (capacitor and supercapacitor) and the designs of wearable systems are under investigations by using PZT nanofibers, which can be embedded in flexible materials but still present piezoelectric performances considerably lower than the PZT disk.

References

- [1] J. Cai, L. Qiu, S. Yuan, L. Shi, P. Liu, and D. Liang, *Structural Health Monitoring for Composite Materials*, vol. 32. 2012.
- [2] F. C. Campbell, “Structural Composite Materials,” *Struct. Compos. Mater.*, 2010, doi: 10.31399/asm.tb.scm.9781627083140.
- [3] R. Jones, *Mechanics of Composite Materials.*, vol. v. 1999.
- [4] R. Le Riche and R. T. Haftka, “Optimization of laminate stacking sequence for buckling load maximization by genetic algorithm,” *AIAA J.*, vol. 31, no. 5, pp. 951–956, 1993, doi: 10.2514/3.11710.
- [5] N. J. Pagano, “Interlaminar response of composite materials,” *Compos. Sci. Technol.*, vol. 39, pp. 377–379, 1990.
- [6] R. M. Koide, G. von Z. de França, and M. A. Luersen, “An ant colony algorithm applied to lay-up optimization of laminated composite plates,” *Lat. Am. J. Solids Struct.*, vol. 10, no. 3, pp. 491–504, 2013, doi: 10.1590/S1679-78252013000300003.
- [7] D. Montalvão, N. M. M. Maia, and A. M. R. Ribeiro, “A review of vibration-based structural health monitoring with special emphasis on composite materials,” *Shock Vib. Dig.*, vol. 38, no. 4, pp. 295–324, 2006, doi: 10.1177/0583102406065898.
- [8] J. B. Ihn and F. K. Chang, “Pitch-catch active sensing methods in structural health monitoring for aircraft structures,” *Struct. Heal. Monit.*, vol. 7, no. 1, pp. 5–19, 2008, doi: 10.1177/1475921707081979.
- [9] D. D. L. Chung, “A review of multifunctional polymer-matrix structural composites,” *Compos. Part B Eng.*, vol. 160, no. November 2018, pp. 644–660, 2019, doi: 10.1016/j.compositesb.2018.12.117.
- [10] S. Wang, D. P. Kowalik, and D. D. L. Chung, “Self-sensing attained in carbon-fiber-polymer-matrix structural composites by using the interlaminar interface as a sensor,” *Smart Mater. Struct.*, vol. 13, no. 3, pp. 570–592, 2004, doi: 10.1088/0964-1726/13/3/017.
- [11] L. Vertuccio, L. Guadagno, G. Spinelli, P. Lamberti, V. Tucci, and S. Russo, “Piezoresistive properties of resin reinforced with carbon nanotubes for health-monitoring of aircraft primary structures,” *Compos. Part B Eng.*, vol. 107, pp. 192–202, 2016, doi: 10.1016/j.compositesb.2016.09.061.
- [12] S. J. Joo, M. H. Yu, W. S. Kim, and H. S. Kim, “Damage detection and self-healing of carbon fiber polypropylene (CFPP)/carbon nanotube (CNT) nano-composite via addressable conducting network,” *Compos. Sci. Technol.*, vol. 167, no. March, pp. 62–70, 2018, doi: 10.1016/j.compscitech.2018.07.035.
- [13] M. C. Koecher, J. H. Pande, S. Merkley, S. Henderson, D. T. Fullwood, and A. E. Bowden, “Piezoresistive in-situ strain sensing of composite laminate structures,” *Compos. Part B Eng.*, vol. 69, pp. 534–541, 2015, doi: 10.1016/j.compositesb.2014.09.029.

- [14] T. CARLSON and L. E. ASP, “An Experimental Study Into the Effect of Damage on the Capacitance of Structural Composite Capacitors,” *J. Multifunct. Compos.*, vol. 2, no. 2, pp. 71–77, 2015, doi: 10.12783/issn.2168-4286/2.2/carlson.
- [15] Z. Shen and H. Zhou, “Mechanical and electrical behavior of carbon fiber structural capacitors: Effects of delamination and interlaminar damage,” *Compos. Struct.*, vol. 166, pp. 38–48, 2017, doi: 10.1016/j.compstruct.2016.12.062.
- [16] J. Yan, A. Downey, A. Chen, S. Laflamme, and S. Hassan, “Capacitance-based sensor with layered carbon-fiber reinforced polymer and titania-filled epoxy,” *Compos. Struct.*, vol. 227, no. July, p. 111247, 2019, doi: 10.1016/j.compstruct.2019.111247.
- [17] R. Matsuzaki, M. Melnykowycz, and A. Todoroki, “Antenna / sensor multifunctional composites for the wireless detection of damage,” *Compos. Sci. Technol.*, vol. 69, no. 15–16, pp. 2507–2513, 2009, doi: 10.1016/j.compscitech.2009.07.002.
- [18] S. Wang and D. D. L. Chung, “Carbon fiber polymer-matrix composite interfaces as thermocouple junctions,” *Compos. interfaces*, 2012, doi: 10.1163/156855499X00198.
- [19] T. Mizutani, Y. Okabe, and N. Takeda, “Quantitative evaluation of transverse cracks in carbon fiber reinforced plastic quasi-isotropic laminates with embedded small-diameter fiber Bragg grating,” *Smart Mater. Struct.*, vol. 12, pp. 898–903, 2003.
- [20] K. Satori, K. Fukuchi, Y. Kurosawa, A. Hongo, and N. Takeda, “Polyimide-coated small-diameter optical fiber sensors for embedding in composite laminate structures,” *SPIE Proc.*, vol. 4328, pp. 285–294, 2001.
- [21] Y. Okabe, S. Yashiro, and T. Kosaka, “Detection of transverse cracks in CFRP composites using embedded fiber Bragg grating sensors,” *Smart Mater. Struct.*, vol. 9, no. 832–838, 2000.
- [22] S. Takeda, Y. Okabe, T. Yamamoto, and N. Takeda, “Detection of edge delamination in CFRP laminates under cyclic loading using small-diameter FBG sensors,” *Compos. Sci. Technol.*, vol. 63, pp. 1885–1894, 2003, doi: 10.1016/S0266-3538(03)00159-3.
- [23] H. Song, W. Wang, Y. Zhou, and G. Zhou, “Mechanical Properties of Composites with Embedded FBG Sensors in Different Layer,” in *IEEE 5th International Conference on Cybernetics and Intelligent Systems*, 2011, pp. 52–56.
- [24] M. Salvetti *et al.*, “On the mechanical response of CFRP composite with embedded optical fibre when subjected to low velocity impact and CAI tests,” *Compos. Struct.*, 2017, doi: 10.1016/j.compstruct.2017.07.063.
- [25] A. Raghavan, C. E. S. Cesnik, A. Raghavan, and C. E. S. Cesnik, “Review of Guided-wave Structural Health Monitoring,” *Shock Vib. Dig.*, 2008, doi: 10.1177/058310240.
- [26] G. Haghiashtiani and M. A. Greminger, “Fabrication , polarization , and characterization of PVDF matrix composites for integrated structural load sensing,” *Smart Mater. Struct.*, vol. 24, 2015, doi: 10.1088/0964-1726/24/4/045038.
- [27] L. De Marchi, A. Perelli, N. Testoni, A. Marzani, and D. Brunelli, “A small, light and low-power passive node sensor for SHM of composite panels,” *9th Int. Work. Struct. Heal. Monit.*, pp. 2218–2224, 2013.
- [28] L. De Marchi, M. Dibiase, and N. Testoni, “Piezoelectric Sensors for Lamb Waves’ Direction of Arrival (DoA) Estimation,” *Proceedings*, vol. 2, no. 13, p. 806, 2018, doi: 10.3390/proceedings2130806.
- [29] S. Masmoudi, A. El, and S. Turki, “Fatigue behaviour and structural health monitoring by acoustic emission of E-glass / epoxy laminates with piezoelectric implant,” *Appl. Acoust.*, vol. 108, pp. 50–58, 2015, doi: 10.1016/j.apacoust.2015.10.024.
- [30] S. Butler *et al.*, “Effect of embedded sensors on interlaminar damage in composite structures,” *J. Intell. Mater. Syst. Struct.*, vol. 22, no. 16, pp. 1857–1868, 2011, doi: 10.1177/1045389X11414225.

- [31] R. Riemer and A. Shapiro, "Biomechanical energy harvesting from human motion : theory , state of the art , design guidelines , and future directions," *J. Neuroeng. Rehabil.*, pp. 1–13, 2011.
- [32] F. R. Fan, Z. Q. Tian, and Z. Lin Wang, "Flexible triboelectric generator," *Nano Energy*, vol. 1, no. 2, pp. 328–334, 2012, doi: 10.1016/j.nanoen.2012.01.004.
- [33] G. Zhu *et al.*, "A shape-adaptive thin-film-based approach for 50% high-efficiency energy generation through micro-grating sliding electrification," *Adv. Mater.*, vol. 26, no. 23, pp. 3788–3796, 2014, doi: 10.1002/adma.201400021.
- [34] Y. Zi, H. Guo, Z. Wen, M.-H. Yeh, C. Hu, and Z. L. Wang, "Harvesting Low-Frequency (<5 Hz) Irregular Mechanical Energy: A Possible Killer Application of Triboelectric Nanogenerator," *ACS Nano*, 2016, doi: 10.1021/acsnano.6b01569.
- [35] Y. S. Zhou, Y. Liu, G. Zhu, Z. Lin, C. Pan, and Q. Jing, "In Situ Quantitative Study of Nanoscale Triboelectric fi cation and Patterning," *Nano Lett.*, 2013.
- [36] P. A. Kumar, P. S. S. Balpande, and P. S. C. Anjankar, "Electromagnetic Energy Harvester for Low Frequency Vibrations using MEMS," *Procedia - Procedia Comput. Sci.*, vol. 79, pp. 785–792, 2016, doi: 10.1016/j.procs.2016.03.104.
- [37] S. Meninger, J. O. Mur-miranda, R. Amirtharajah, A. P. Chandrakasan, and J. H. Lang, "Vibration-to-Electric Energy Conversion," *IEEE Trans.*, vol. 9, no. 1, pp. 64–76, 2001.
- [38] X. Pu, W. Hu, and Z. L. Wang, "Toward Wearable Self-Charging Power Systems: The Integration of Energy-Harvesting and Storage Devices," *Small*, vol. 14, no. 1, pp. 1–19, 2018, doi: 10.1002/sml.201702817.
- [39] N. Sezer and M. Koç, "A comprehensive review on the state-of-the-art of piezoelectric energy harvesting," *Nano Energy*, vol. 80, no. November 2020, p. 105567, 2021, doi: 10.1016/j.nanoen.2020.105567.
- [40] M. S. Vijaya, *Piezoelectric Materials and Devices Applications in Engineering and Medical Sciences* 0. 2008.
- [41] B. Jaffe, W. R. Cook, and H. L. Jaffe, "Piezoelectric Ceramics," *Handbook of Advanced Ceramics: Materials, Applications, Processing and Properties*, vol. 2–2. pp. 107–159, 1971, doi: 10.1016/B978-012654640-8/50029-8.
- [42] M. Saeedifar, J. Mansvelder, R. Mohammadi, and D. Zarouchas, "Using passive and active acoustic methods for impact damage assessment of composite structures," *Compos. Struct.*, vol. 226, no. July, p. 111252, 2019, doi: 10.1016/j.compstruct.2019.111252.
- [43] U. Pierre Claver and G. Zhao, "Recent Progress in Flexible Pressure Sensors Based Electronic Skin," *Adv. Eng. Mater.*, vol. 23, no. 5, pp. 1–17, 2021, doi: 10.1002/adem.202001187.
- [44] M. Serridge and T. R. Licht, "Accelerometers Piezoelectric and Vibration Preamplifiers. Theory and Application Handbook," p. 151, 1987, [Online]. Available: <http://www.bksv.com/Products/transducers/vibration/accelerometers/handbook.aspx>.
- [45] Y. Sugawara, K. Onitsuka, S. Yoshikawa, Q. Xu, R. E. Newnham, and K. Uchino, "Metal–Ceramic Composite Actuators," *J. Am. Ceram. Soc.*, vol. 75, no. 4, pp. 996–998, 1992, doi: 10.1111/j.1151-2916.1992.tb04172.x.
- [46] D. Arnold, W. Kinsel, W. W. Clark, and C. Mo, "Exploration of new cymbal design in energy harvesting," *Act. Passiv. Smart Struct. Integr. Syst.* 2011, vol. 7977, no. March, p. 79770T, 2011, doi: 10.1117/12.880614.
- [47] H. P. Hu, Z. J. Cui, and J. G. Cao, "Performance of a piezoelectric bimorph harvester with variable width," *J. Mech.*, vol. 23, no. 3, pp. 197–202, 2007, doi: 10.1017/S1727719100001222.
- [48] S. R. Anton and H. A. Sodano, "A review of power harvesting using piezoelectric materials (2003-

2006),” *Smart Mater. Struct.*, vol. 16, no. 3, 2007, doi: 10.1088/0964-1726/16/3/R01.

- [49] D. Motter, J. V. Lavarda, F. A. Dias, and S. da Silva, “Vibration energy harvesting using piezoelectric transducer and non-controlled rectifiers circuits,” *J. Brazilian Soc. Mech. Sci. Eng.*, vol. 34, no. spe, pp. 378–385, 2012, doi: 10.1590/s1678-58782012000500006.
- [50] Z. Pi, J. Zhang, C. Wen, Z. bin Zhang, and D. Wu, “Flexible piezoelectric nanogenerator made of poly(vinylidene fluoride-co-trifluoroethylene) (PVDF-TrFE) thin film,” *Nano Energy*, vol. 7, no. JULY, pp. 33–41, 2014, doi: 10.1016/j.nanoen.2014.04.016.
- [51] C. K. Jeong, C. Baek, A. I. Kingon, K. Il Park, and S. H. Kim, “Lead-Free Perovskite Nanowire-Employed Piezopolymer for Highly Efficient Flexible Nanocomposite Energy Harvester,” *Small*, vol. 14, no. 19, pp. 1–8, 2018, doi: 10.1002/sml.201704022.
- [52] F. Narita and M. Fox, “A Review on Piezoelectric, Magnetostrictive, and Magnetoelectric Materials and Device Technologies for Energy Harvesting Applications,” *Adv. Eng. Mater.*, vol. 20, no. 5, pp. 1–22, 2018, doi: 10.1002/adem.201700743.
- [53] Newhnam, “United States Patent [19],” pp. 2–7, 1983.
- [54] J. Doshi and D. H. Reneker, “Electrospinning process and applications of electrospun fibers,” *J. Electrostat.*, vol. 3, pp. 1698–1703, 1995, doi: 10.1109/ias.1993.299067.
- [55] G. K. A. N. N. Turdakyn, I. Abay, and A. M. D. A. Z. Bakenov, “A Review of Piezoelectric PVDF Film by Electrospinning and Its Applications,” *Sensors*, vol. 20, 2020, doi: 10.3390/s20185214.
- [56] M. Wang, D.-G. Yu, X. Li, and G. R. Williams, “The Development and Bio-applications of Multifluid Electrospinning,” *Mater. Highlights*, vol. 1, no. 1–2, p. 1, 2020, doi: 10.2991/mathi.k.200521.001.
- [57] J. Xue, T. Wu, Y. Dai, and Y. Xia, “Electrospinning and electrospun nanofibers: Methods, materials, and applications,” *Chem. Rev.*, vol. 119, no. 8, pp. 5298–5415, 2019, doi: 10.1021/acs.chemrev.8b00593.
- [58] J. M. Aamodt and D. W. Grainger, “Extracellular matrix-based biomaterial scaffolds and the host response,” *Biomaterials*, vol. 86, pp. 68–82, 2016, doi: 10.1016/j.biomaterials.2016.02.003.
- [59] X. Wang, B. Ding, and B. Li, “Biomimetic electrospun nanofibrous structures for tissue engineering,” *Mater. Today*, vol. 16, no. 6, pp. 229–241, 2013, doi: 10.1016/j.mattod.2013.06.005.
- [60] J. Xie, M. R. MacEwan, A. G. Schwartz, and Y. Xia, “Electrospun nanofibers for neural tissue engineering,” *Nanoscale*, vol. 2, no. 1, pp. 35–44, 2010, doi: 10.1039/b9nr00243j.
- [61] L. Ma *et al.*, “Trap effect of three-dimensional fibers network for high efficient cancer-cell capture,” *Adv. Healthc. Mater.*, vol. 4, no. 6, pp. 838–843, 2015, doi: 10.1002/adhm.201400650.
- [62] L. Sun *et al.*, “Enhanced wound healing in diabetic rats by nanofibrous scaffolds mimicking the basketweave pattern of collagen fibrils in native skin,” *Biomater. Sci.*, vol. 6, no. 2, pp. 340–349, 2018, doi: 10.1039/c7bm00545h.
- [63] A. K. Selvam and G. Nallathambi, “Polyacrylonitrile/silver nanoparticle electrospun nanocomposite matrix for bacterial filtration,” *Fibers Polym.*, vol. 16, no. 6, pp. 1327–1335, 2015, doi: 10.1007/s12221-015-1327-8.
- [64] Z. He, F. Rault, M. Lewandowski, E. Mohsenzadeh, and F. Salaün, “Electrospun PVDF nanofibers for piezoelectric applications: A review of the influence of electrospinning parameters on the β phase and crystallinity enhancement,” *Polymers (Basel)*, vol. 13, no. 2, pp. 1–23, 2021, doi: 10.3390/polym13020174.
- [65] C. J. Buchko, K. M. Kozloff, and D. C. Martin, “Surface characterization of porous, biocompatible protein polymer thin films,” *Biomaterials*, vol. 22, no. 11, pp. 1289–1300, 2001, doi: 10.1016/S0142-9612(00)00281-7.

- [66] T. Jarusuwannapoom *et al.*, “Effect of solvents on electro-spinnability of polystyrene solutions and morphological appearance of resulting electrospun polystyrene fibers,” *Eur. Polym. J.*, vol. 41, no. 3, pp. 409–421, 2005, doi: 10.1016/j.eurpolymj.2004.10.010.
- [67] D. Fabiani, G. Selleri, F. Grolli, and M. Speranza, “Piezoelectric nanofibers for multifunctional composite materials,” *Conf. Electr. Insul. Dielectr. Phenomena, CEIDP*, vol. 2020-Octob, pp. 247–250, 2020, doi: 10.1109/CEIDP49254.2020.9437547.
- [68] K. Gulnur *et al.*, “A Review of Piezoelectric PVDF Film by Electrospinning and Its Applications,” *Sensors*, vol. 1, no. 4, 2020, doi: 10.1088/2043-6262/1/4/043002.
- [69] L. F. Zhu, Y. Zheng, J. Fan, Y. Yao, Z. Ahmad, and M. W. Chang, “A novel core-shell nanofiber drug delivery system intended for the synergistic treatment of melanoma,” *Eur. J. Pharm. Sci.*, vol. 137, no. July, p. 105002, 2019, doi: 10.1016/j.ejps.2019.105002.
- [70] C. Zhang *et al.*, “Nanoporous hollow fibers as a phantom material for the validation of diffusion magnetic resonance imaging,” *J. Appl. Polym. Sci.*, vol. 136, no. 23, pp. 1–12, 2019, doi: 10.1002/app.47617.
- [71] S. Wu, B. Wang, Z. Ahmad, J. Huang, M. W. Chang, and J. S. Li, “Surface modified electrospun porous magnetic hollow fibers using secondary downstream collection solvent contouring,” *Mater. Lett.*, vol. 204, pp. 73–76, 2017, doi: 10.1016/j.matlet.2017.06.015.
- [72] M. Shibuya, M. J. Park, S. Lim, S. Phuntsho, H. Matsuyama, and H. K. Shon, “Novel CA/PVDF nanofiber supports strategically designed via coaxial electrospinning for high performance thin-film composite forward osmosis membranes for desalination,” *Desalination*, vol. 445, no. January, pp. 63–74, 2018, doi: 10.1016/j.desal.2018.07.025.
- [73] F. Li, T. Zhang, X. Gao, R. Wang, and B. Li, “Coaxial electrospinning heterojunction SnO₂/Au-doped In₂O₃ core-shell nanofibers for acetone gas sensor,” *Sensors Actuators, B Chem.*, vol. 252, pp. 822–830, 2017, doi: 10.1016/j.snb.2017.06.077.
- [74] G. H. Lee, J. C. Song, and K. B. Yoon, “Controlled wall thickness and porosity of polymeric hollow nanofibers by coaxial electrospinning,” *Macromol. Res.*, vol. 18, no. 6, pp. 571–576, 2010, doi: 10.1007/s13233-010-0607-9.
- [75] D. Li and Y. Xia, “Direct fabrication of composite and ceramic hollow nanofibers by electrospinning,” *Nano Lett.*, vol. 4, no. 5, pp. 933–938, 2004, doi: 10.1021/nl049590f.
- [76] J. Ning, M. Yang, H. Yang, and Z. Xu, “Tailoring the morphologies of PVDF nanofibers by interfacial diffusion during coaxial electrospinning,” *Mater. Des.*, vol. 109, pp. 264–269, 2016, doi: 10.1016/j.matdes.2016.07.074.
- [77] T. Sharma, S. Naik, J. Langevine, B. Gill, and J. X. J. Zhang, “Aligned PVDF-TrFE nanofibers with high-density PVDF nanofibers and PVDF core-shell structures for endovascular pressure sensing,” *IEEE Trans. Biomed. Eng.*, vol. 62, no. 1, pp. 188–195, 2015, doi: 10.1109/TBME.2014.2344052.
- [78] S. Rana, P. Subramani, R. Fanguero, and A. G. Correia, “A review on smart self-sensing composite materials for civil engineering applications,” *AIMS Mater. Sci.*, vol. 3, no. 2, pp. 357–379, 2016, doi: 10.3934/materci.2016.2.357.
- [79] M. Sun, W. J. Staszewski, and R. N. Swamy, “Smart sensing technologies for structural health monitoring of civil engineering structures,” *Adv. Civ. Eng.*, vol. 2010, 2010, doi: 10.1155/2010/724962.
- [80] C. Tuloup, W. Harizi, Z. Aboura, and Y. Meyer, “Integration of piezoelectric transducers (PZT and PVDF) within polymer-matrix composites for structural health monitoring applications: new success and challenges,” *Int. J. Smart Nano Mater.*, vol. 00, no. 00, pp. 1–27, 2020, doi: 10.1080/19475411.2020.1830196.
- [81] K. B. Kim *et al.*, “Transparent and flexible piezoelectric sensor for detecting human movement with a boron nitride nanosheet (BNNS),” *Nano Energy*, pp. 91–98, 2018, doi: 10.1016/j.nanoen.2018.09.056.

- [82] Y. Xin, J. Zhu, H. Sun, Y. Xu, T. Liu, and C. Qian, "A brief review on piezoelectric PVDF nanofibers prepared by electrospinning," *Ferroelectrics*, vol. 526, no. 1, pp. 140–151, 2018, doi: 10.1080/00150193.2018.1456304.
- [83] X. Wang *et al.*, "Bionic single-electrode electronic skin unit based on piezoelectric nanogenerator," *ACS Nano*, vol. 12, no. 8, pp. 8588–8596, 2018, doi: 10.1021/acsnano.8b04244.
- [84] K. Maity, S. Garain, K. Henkel, D. Schmeißer, and D. Mandal, "Self-Powered Human-Health Monitoring through Aligned PVDF Nanofibers Interfaced Skin-Interactive Piezoelectric Sensor," *ACS Appl. Polym. Mater.*, vol. 2, no. 2, pp. 862–878, 2020, doi: 10.1021/acsapm.9b00846.
- [85] A. Closson, H. Richards, Z. Xu, C. Jin, L. Dong, and J. X. J. Zhang, "Method for Inkjet-printing PEDOT:PSS polymer electrode arrays on piezoelectric PVDF-TrFE fibers," *IEEE Sens. J.*, vol. XX, no. XX, 2021, doi: 10.1109/JSEN.2021.3071321.
- [86] T. M. Brugo *et al.*, "Self-sensing hybrid composite laminate by piezoelectric nanofibers interleaving," *Compos. Part B Eng.*, vol. 212, no. October 2020, p. 108673, 2021, doi: 10.1016/j.compositesb.2021.108673.
- [87] T. Brugo and R. Palazzetti, "The effect of thickness of Nylon 6,6 nanofibrous mat on Modes I–II fracture mechanics of UD and woven composite laminates," *Compos. Struct.*, vol. 154, pp. 172–178, 2016, doi: 10.1016/j.compstruct.2016.07.034.
- [88] P. Martins, A. C. Lopes, and S. Lanceros-Mendez, "Electroactive phases of poly(vinylidene fluoride): Determination, processing and applications," *Prog. Polym. Sci.*, vol. 39, no. 4, pp. 683–706, 2014, doi: 10.1016/j.progpolymsci.2013.07.006.
- [89] S. Park, Y. Kwon, M. Sung, B. S. Lee, J. Bae, and W. R. Yu, "Poling-free spinning process of manufacturing piezoelectric yarns for textile applications," *Mater. Des.*, vol. 179, p. 107889, 2019, doi: 10.1016/j.matdes.2019.107889.
- [90] A. C. Choi *et al.*, "Polarization Mechanisms in P(VDF-TrFE) Ferroelectric Thin Films," *Phys. Status Solidi - Rapid Res. Lett.*, vol. 12, no. 10, pp. 1–7, 2018, doi: 10.1002/pssr.201800340.
- [91] X. Liu, S. Xu, X. Kuang, D. Tanb, and X. Wang, "Nanoscale investigations on β -phase orientation, piezoelectric response, and polarization direction of electrospun PVDF nanofibers," *RSC Adv.*, 2016, doi: 10.1039/x0xx00000x.
- [92] F. Calavalle, M. Zaccaria, G. Selleri, T. Cramer, D. Fabiani, and B. Fraboni, "Piezoelectric and Electrostatic Properties of Electrospun PVDF-TrFE Nanofibers and their Role in Electromechanical Transduction in Nanogenerators and Strain Sensors," *Macromol. Mater. Eng.*, vol. 305, no. 7, pp. 1–8, 2020, doi: 10.1002/mame.202000162.
- [93] G. Eberle, E. Bihler, and W. Eisenmenger, "Polarization Dynamics of VDF-TrFE Copolymers," *IEEE Trans. Electr. Insul.*, vol. 26, no. 1, pp. 69–77, 1991, doi: 10.1109/14.68230.
- [94] H. L. W. Chan *et al.*, "Polarization of thick polyvinylidene fluoride/trifluoroethylene copolymer films," *J. Appl. Phys.*, vol. 80, no. 7, pp. 3982–3991, 1996, doi: 10.1063/1.363356.
- [95] H. Naderiallaf, P. Seri, and G. C. Montanari, "Designing a HVDC Insulation System to Endure Electrical and Thermal Stresses under Operation. Part I: Partial Discharge Magnitude and Repetition Rate during Transients and in DC Steady State," *IEEE Access*, vol. 9, pp. 35730–35739, 2021, doi: 10.1109/ACCESS.2021.3062440.
- [96] G. Selleri *et al.*, "Study on the polarization process for piezoelectric nanofibrous layers," *IEEE Conf. Electr. Insul. Dielectr. Phenom.*, pp. 31–34, 2021.
- [97] H. Naderiallaf, P. Seri, and G. Montanari, "On the calculation of the dielectric time constant of DC insulators containing cavities," in *IEEE Conf. Electr. Insul. Dielectr. Phenom.*, 2021, pp. 668–671.
- [98] F. H. Kreuger, *Industrial High DC Voltage 1. Fields 2. Breakdowns 3. Tests.* 1995.

- [99] G. Selleri, D. Fabiani, A. Zucchelli, T. M. Brugo, F. Grolli, and L. Bordoni, “Development of flexible sensors based on piezoelectric nanofibers,” *Proc. IEEE Int. Conf. Prop. Appl. Dielectr. Mater.*, vol. 2021-July, no. Icpadm, pp. 358–361, 2021, doi: 10.1109/ICPADM49635.2021.9493957.
- [100] R. Schueler, J. Petermann, K. Schulte, and H. P. Wentzel, “Percolation in carbon black filled epoxy resin,” *Macromol. Symp.*, vol. 104, pp. 261–268, 1996, doi: 10.1002/masy.19961040122.
- [101] H. J. Choi, M. S. Kim, D. Ahn, S. Y. Yeo, and S. Lee, “Electrical percolation threshold of carbon black in a polymer matrix and its application to antistatic fibre,” *Sci. Rep.*, vol. 9, no. 1, pp. 1–12, 2019, doi: 10.1038/s41598-019-42495-1.
- [102] J. Karki, “Signal conditioning piezoelectric sensors,” *App. Rep. SLOA33A*, vol. 126, no. 2, pp. 1–6, 2000, doi: 10.1115/1.1766030.
- [103] X. Wang, F. Sun, G. Yin, Y. Wang, B. Liu, and M. Dong, “Tactile-sensing based on flexible PVDF nanofibers via electrospinning: A review,” *Sensors (Switzerland)*, vol. 18, no. 2, 2018, doi: 10.3390/s18020330.
- [104] J.-Y. Ke, H.-J. Chu, Y.-H. Hsu, and C.-K. Lee, “A highly flexible piezoelectret-fiber pressure sensor based on highly aligned P(VDF-TrFE) electrospun fibers,” *Act. Passiv. Smart Struct. Integr. Syst. 2017*, vol. 10164, p. 101642X, 2017, doi: 10.1117/12.2259854.
- [105] D. Edmondson, A. Cooper, S. Jana, D. Wood, and M. Zhang, “Centrifugal electrospinning of highly aligned polymer nanofibers over a large area,” *J. Mater. Chem.*, vol. 22, no. 35, pp. 18646–18652, 2012, doi: 10.1039/c2jm33877g.
- [106] W. A. Yee, M. Kotaki, Y. Liu, and X. Lu, “Morphology, polymorphism behavior and molecular orientation of electrospun poly(vinylidene fluoride) fibers,” *Polymer (Guildf.)*, vol. 48, no. 2, pp. 512–521, 2007, doi: 10.1016/j.polymer.2006.11.036.
- [107] D. Fabiani *et al.*, “Nanofibrous piezoelectric structures for composite materials to be used in electrical and electronic components,” *Proc. Nord. Insul. Symp.*, no. 26, pp. 1–5, 2019, doi: 10.5324/nordis.v0i26.3263.
- [108] H. Yu, T. Huang, M. Lu, M. Mao, Q. Zhang, and H. Wang, “Enhanced power output of an electrospun PVDF/MWCNTs-based nanogenerator by tuning its conductivity,” *Nanotechnology*, vol. 24, no. 40, 2013, doi: 10.1088/0957-4484/24/40/405401.
- [109] K. Forward, A. Flores, and G. Rutledge, “Production of core-shell fibers by electrospinning from a free surface _ Elsevier Enhanced Reader.pdf,” *Chem. Eng. Sci.*, 2013.
- [110] J. Jiang, J. Jiang, X. Deng, and Z. Deng, “Detecting debonding between steel beam and reinforcing CFRP plate using active sensing with removable PZT-based transducers,” *Sensors (Switzerland)*, vol. 20, no. 1, 2020, doi: 10.3390/s20010041.
- [111] B. Yang *et al.*, “Damage Localization in Composite Laminates by Building in PZT Wafer Transducers: A Comparative Study with Surface-Bonded PZT Strategy,” *Adv. Eng. Mater.*, vol. 21, no. 3, pp. 1–12, 2019, doi: 10.1002/adem.201801040.
- [112] H. P. Konka, M. A. Wahab, and K. Lian, “The effects of embedded piezoelectric fiber composite sensors on the structural integrity of glass-fiber-epoxy composite laminate,” *Smart Mater. Struct.*, vol. 21, no. 1, 2012, doi: 10.1088/0964-1726/21/1/015016.
- [113] M. Y. Hwang and L. H. Kang, “Characteristics and fabrication of piezoelectric GFRP using smart resin prepreg for detecting impact signals,” *Compos. Sci. Technol.*, vol. 167, no. July, pp. 224–233, 2018, doi: 10.1016/j.compscitech.2018.08.002.
- [114] P. Taylor, R. G. Kepler, and R. A. Anderson, “Advances in Physics Ferroelectric polymers Ferroelectric polymers,” no. July 2012, pp. 37–41, 1992.
- [115] D. P. Skinner, R. E. Newnham, and L. E. Cross, “Flexible composite transducers,” *Mater. Res. Bull.*, vol. 13, pp. 599–607, 1978.

- [116] R. Newnham, D. Skinner, and L. Cross, "Connectivity and piezoelectric-pyroelectric composites," *Mater. Res. Bull.*, vol. 13, pp. 525–536, 1978.
- [117] H. Zarei, T. Brugo, J. Belcari, H. Bisadi, G. Minak, and A. Zucchelli, "Low velocity impact damage assessment of GLARE fiber-metal laminates interleaved by Nylon 6,6 nanofiber mats," *Compos. Struct.*, vol. 167, pp. 123–131, 2017, doi: 10.1016/j.compstruct.2017.01.079.
- [118] H. Zarei, T. Brugo, J. Belcari, H. Bisadi, G. Minak, and A. Zucchelli, "Low velocity impact damage assessment of GLARE fiber-metal laminates interleaved by Nylon 6,6 nanofiber mats," *Compos. Struct.*, vol. 167, pp. 123–131, 2017, doi: 10.1016/j.compstruct.2017.01.079.
- [119] J. Briscoe and S. Dunn, "Piezoelectric nanogenerators - a review of nanostructured piezoelectric energy harvesters," *Nano Energy*, vol. 14, pp. 15–29, 2014, doi: 10.1016/j.nanoen.2014.11.059.
- [120] H. A. Sodano, D. J. Inman, and G. Park, "A review of power harvesting from vibration using piezoelectric materials," *Shock Vib. Dig.*, vol. 36, no. 3, pp. 197–205, 2004, doi: 10.1177/0583102404043275.
- [121] M. Alexe, S. Senz, M. A. Schubert, D. Hesse, and U. Gösele, "Energy harvesting using nanowires?," *Adv. Mater.*, vol. 20, no. 21, pp. 4021–4026, 2008, doi: 10.1002/adma.200800272.
- [122] Z. L. Wang, "Energy harvesting using piezoelectric nanowires-a correspondence on 'Energy harvesting using nanowires?' by alexe et al.," *Adv. Mater.*, vol. 21, no. 13, pp. 1311–1315, 2009, doi: 10.1002/adma.200802638.
- [123] L. Serairi, L. Gu, Y. Qin, Y. Lu, P. Basset, and Y. Leprince-Wang, "Flexible piezoelectric nanogenerators based on PVDF-TrFE nanofibers," *EPJ Appl. Phys.*, vol. 80, no. 3, pp. 1–7, 2017, doi: 10.1051/epjap/2017170288.
- [124] J. F. Antaki, "A Gait powered autologous battery charging system for artificial organ.pdf," *ASAIO J. Am. Soc. Artif. Intern. Organs 1992*, vol. 41, pp. M588-595, 1995.
- [125] J. Kymissis, C. Kendall, J. Paradiso, and N. Gershenfeld, "Parasitic Power Harvesting in Shoes John," *Dig. Pap. Second Int. Symp. Wearable Comput. (Cat. No.98EX215)*, pp. 13–23, 1998.
- [126] M. Renaud, T. Sterken, P. Fiorini, R. Puers, K. Baert, and C. Van Hoof, "Scavenging energy from human body:design of a piezoelectric transducer," *Dig. Tech. Pap. - Int. Conf. Solid State Sensors Actuators Microsystems, TRANSDUCERS '05*, vol. 1, pp. 784–787, 2005, doi: 10.1109/SENSOR.2005.1496534.
- [127] M. Pozzi and M. Zhu, "Characterization of a rotary piezoelectric energy harvester based on plucking excitation for knee-joint wearable applications," *Smart Mater. Struct.*, vol. 21, no. 5, 2012, doi: 10.1088/0964-1726/21/5/055004.
- [128] J. Feenstra, J. Granstrom, and H. Sodano, "Energy harvesting through a backpack employing a mechanically amplified piezoelectric stack," *Mech. Syst. Signal Process.*, vol. 22, no. 3, pp. 721–734, 2008, doi: 10.1016/j.ymsp.2007.09.015.
- [129] M. H. Chung *et al.*, "Enhanced output performance on LbL multilayer PVDF-TrFE piezoelectric films for charging supercapacitor," *Sci. Rep.*, vol. 9, no. 1, pp. 6–11, 2019, doi: 10.1038/s41598-019-43098-6.
- [130] Y. Hu, C. Xu, Y. Zhang, L. Lin, R. L. Snyder, and Z. L. Wang, "A nanogenerator for energy harvesting from a rotating tire and its application as a self-powered pressure/speed sensor," *Adv. Mater.*, vol. 23, no. 35, pp. 4068–4071, 2011, doi: 10.1002/adma.201102067.
- [131] L. Yuan *et al.*, "Paper-based supercapacitors for self-powered nanosystems," *Angew. Chemie - Int. Ed.*, vol. 51, no. 20, pp. 4934–4938, 2012, doi: 10.1002/anie.201109142.

